




ADVERTIMENT. L'accés als continguts d'aquesta tesi queda condicionat a l'acceptació de les condicions d'ús establertes per la següent llicència Creative Commons:  <https://creativecommons.org/licenses/?lang=ca>

ADVERTENCIA. El acceso a los contenidos de esta tesis queda condicionado a la aceptación de las condiciones de uso establecidas por la siguiente licencia Creative Commons:  <https://creativecommons.org/licenses/?lang=es>

WARNING. The access to the contents of this doctoral thesis it is limited to the acceptance of the use conditions set by the following Creative Commons license:  <https://creativecommons.org/licenses/?lang=en>

Polymorphism in Organic Semiconductor Thin Films: A Nanoscale Investigation of Thermal and Interfacial Effects

**Doctoral Thesis
In Materials Science**

Author: Shunya Yan

Supervisor/Tutor: Dr. Esther Barrena

Group of Physical Chemistry of Surfaces and Interfaces,
Institut de Ciència de Materials de Barcelona (ICMAB-CSIC)

Department of Physics, Faculty of Science,

September, 2024

ABSTRACT

This thesis presents an experimental work that provides insight into the effects of temperature, interface, and film thickness on the polymorphism of organic semiconductor thin films at the nanoscale by utilizing a combination of advanced characterization techniques. The organic semiconductor thin film samples were prepared using the organic molecular beam deposition (OMBD).

This thesis contains three main studies. In the first study, we examined how substrate temperature during both annealing and film deposition affects the structure of C8O-BTBT-OC8 thin films. Using a combination of AFM and GIWAXS, we identified a temperature-induced structural transformation into a new polymorph (high-temperature phase) that implies a tilted configuration of the molecules. It was demonstrated that, after cooling to room temperature, the two distinct structures may coexist at the interface between the organic thin film and silicon dioxide.

In our second study, we employed AFM, KPFM, GIWAX, and UPS techniques to investigate polymorphism in Ph-BTBT-10 thin films. Due to its asymmetric charge distribution in the molecule, this BTBT derivative has a dipolar electrical dipole. Our findings reveal an important role of the dipolar electrostatic interactions between molecules leading to a great level of structural intricacy. During growth the molecular packing structure evolves from an initial bilayer configuration at the interface (thickness of 5 nm) to a lamellar packing of polar layers (i.e with a net electrical dipole) that ultimately transforms into the reported non-polar thin-film phase due to an increase in the percentage of flipped molecules in the packing (for thickness exceeding 20 nm). This work also highlights the importance of KPFM in studying nanoscale polar polymorphs.

In our third study we conducted in situ thermal annealing experiments by combining KPFM and GIWAXS to investigate the impact of interface and thickness on the structural transition of Ph-BTBT-10 thin films and the stability of the formed crystalline

polymorphs. Our results demonstrate that a reduced film thickness enhances the stability of the bulk phase, as indicated by a lower critical temperature for the structural transition from a single-layer lamellar packing to the bilayer structure. This observation is in contrast with findings for other organic semiconductor films and is explained by the stabilization of the bilayer at the substrate interface.

Carrier mobility is a key performance indicator for OFETs. As the organic thin film serves as the active layer of OFETs, understanding and controlling the polymorphism and structure of thin films at the nanoscale are crucial for enhancing device performance. Our study reveals how thermal conditions, interfaces, and thickness influence molecular packing, offering insights to improve the performance and reproducibility of OFETs.

RESUMEN

Esta tesis presenta un trabajo experimental que proporciona información sobre los efectos de la temperatura, la interfaz y el espesor de la película en el polimorfismo de películas delgadas de semiconductores orgánicos a escala nanométrica, utilizando una combinación de técnicas avanzadas de caracterización. Las muestras de películas delgadas de semiconductores orgánicos se prepararon utilizando la deposición de haces moleculares orgánicos (OMBD).

Esta tesis contiene tres estudios principales. En el primer estudio, examinamos cómo la temperatura del sustrato durante el calentamiento y la deposición de la película afecta la estructura de las películas delgadas de C8O-BTBT-OC8. Usando una combinación de AFM y GIWAXS, identificamos una transformación estructural inducida por la temperatura en un nuevo polimorfo (fase de alta temperatura) que implica una configuración inclinada de las moléculas. Se demostró que, después de enfriar a temperatura ambiente, las dos estructuras distintas pueden coexistir en la interfaz entre la película delgada orgánica y el dióxido de silicio.

En nuestro segundo estudio, empleamos técnicas de AFM, KPFM, GIWAX y UPS para investigar el polimorfismo en películas delgadas de Ph-BTBT-10. Debido a su distribución de carga asimétrica en la molécula, este derivado de BTBT tiene un dipolo eléctrico dipolar. Nuestros hallazgos revelan un papel importante de las interacciones electrostáticas dipolares entre moléculas, lo que lleva a un alto nivel de complejidad estructural. Durante el crecimiento, la estructura de empaquetamiento molecular evoluciona desde una configuración inicial de bicapa en la interfaz (espesor de 5 nm) hasta un empaquetamiento laminar de capas polares (es decir, con un dipolo eléctrico neto) que finalmente se transforma en la fase de película delgada no polar reportada. Esto se atribuye debido a un aumento en el porcentaje de moléculas invertidas en el

empaquetamiento (para espesores superiores a 20 nm). Este trabajo también destaca la importancia de KPFM en el estudio de polimorfos polares a escala nanométrica.

En nuestro tercer estudio, realizamos experimentos de calentamiento in situ combinando KPFM y GIWAXS para investigar el impacto de la interfaz y el espesor en la transición estructural de las películas delgadas de Ph-BTBT-10 y la estabilidad de los polimorfos cristalinos formados. Nuestros resultados demuestran que una reducción en el espesor de la película mejora la estabilidad de la fase bicapa, como lo indica una temperatura crítica más baja para la transición estructural. Esta observación contrasta con los hallazgos para otras películas de semiconductores orgánicos y se explica por la estabilización de la bicapa en la interfaz del sustrato.

La movilidad de los portadores es un indicador clave del rendimiento para los OFETs. Dado que la película delgada orgánica sirve como la capa activa de los OFETs, comprender y controlar el polimorfismo y la estructura de las películas delgadas a escala nanométrica es crucial para mejorar el rendimiento del dispositivo. Nuestro estudio revela cómo las condiciones térmicas, las interfaces y el espesor influyen en el empaquetamiento molecular, ofreciendo ideas para mejorar el rendimiento y la reproducibilidad de los OFETs.

CONTENTS

Abstract	i
Contents	v
Acronyms and Symbols	ix
1 MOTIVATION	1
I INTRODUCTION	
2 FUNDAMENTALS	
2.1 Organic semiconductor materials.....	7
2.1.1 Design strategy.....	9
2.1.2 Structure and polymorphism.....	10
2.2 BTBT derivatives.....	13
2.2.1 Historic development.....	13
2.2.2 C8O-BTBTOC8.....	18
2.2.3 Ph-BTBT-10.....	19
2.3 OFETS	22
2.3.1 Basic Concept	22
2.4 References.....	28
3 MAIN METHODS AND TECHNIQUES.....	37
3.1 Substrates prepared and cleaning.....	37

3.2 Organic Molecular Beam Deposition (OMBD).....	38
3.3 Atomic force microscopy.....	42
3.3.1 AFM setup and basic operation	43
3.3.2 AFM measurement mode.....	45
3.3.2.1 Contact mode	45
3.3.2.2 Dynamic mode	47
3.3.3 AFM advanced operation modes	51
3.3.3.1 Friction force microscopy	51
3.3.3.2 Kelvin probe force microscopy.....	52
3.4 X-ray Diffraction	56
3.5 Ultraviolet Photoemission Spectroscopy (UPS)	59
3.6 Fabrication and Characterization of OFETs	60
3.7 Reference	62

II RESULTS AND DISCUSSION

4 Paper I: Temperature-induced Polymorphism of a Benzothiophene Derivative: Reversibility and Impact on the Thin Film Morphology	71
5 Paper II: Polar polymorphism: a new intermediate structure towards the thin- film phase in asymmetric benzothieno[3,2-b][1]-benzothiophene derivatives.....	85
6 Paper III: Thickness dependent structural transition in Ph-BTBT-10 thin films and stabilization of the ubiquitous interface bilayer	105

III CONCLUSIONS

7 SUMMARY AND PERSPECTIVES 143

8 Author’s Contributions 147

9 Acknowledgements..... 149

ACRONYMS AND SYMBOLS

OSC	Organic Semiconductor
OLED	Organic Light-emitting Diodes
OFET	Organic Field-effect Transistor
CT	Charge-Transfer
GIWAXS	Grazing Incidence Wide-angle X-ray Scattering
AM	Amplitude Modulation
FM	Frequency Modulation
AFM	Atomic Force Microscopy
KPFM	Local Kelvin Probe Force Microscopy
SIP	Surface-induced Phase
HIP	High Temperature Polymorph
UPS	Ultra-Violet Photoelectron Spectroscopy
OMBD	Organic Molecular Beam Deposition
HOMO	Highest Occupied Molecular Orbital
LUMO	Lowest Unoccupied Molecular Orbital
LHB	Layer Herringbone
WF	Work Function
CV	Cyclic Voltammetry
SAM	Self-assembled Monolayer
PS	Polystyrene
SmE	Smectic E
OTFT	Organic Thin-Film Transistor
NCFET	Negative Capacitance Field-effect Transistor
RC	Contact Resistance

QM	Quartz Microbalance
TEM	Transmission Electron Microscopy
SPM	Scanning Probe Microscopy
FFM	Friction Force Microscopy
CPD	Contact Potential Difference
SP	Surface Potential
XRD	X-ray Diffraction
GIXD	Grazing Incidence X-ray Diffraction
FWHM	Full Width at Half Maximum
SECO	Secondary Electron Cutoff
AC	Alternating Current
DC	Direct Current

ω	Oscillation Frequency
A	Oscillation Amplitude
Φ	Work Function
E_F	Fermi Level
E_{vac}	Vacuum Level
e	Electronic Charge
k	Force Constant
q	Scattering Vector
θ	Scattering Angle
λ	Radiation Wavelength
μ	Mobility

1

MOTIVATION

Organic semiconductor (OSC) thin films based on π -conjugated molecules have garnered significant interest in electronic devices. In recent years, substantial progress has been made in this field, resulting in a growing market for organic semiconductor electronic products, such as organic light-emitting diodes (OLED) display technology. Although the development of organic field-effect transistors (OFETs) has not progressed as rapidly as OLEDs, OFETs have emerged as a commercially viable technology. However, many fundamental research questions remain unresolved. Carrier mobility is a primary performance indicator for OFETs. It depends on structural details at different length scales, which are not yet fully understood or satisfactorily controlled. One critical issue is polymorphism. The adopted crystal structure is driven by weak intermolecular van der Waals forces, giving organic semiconductor materials a high propensity to polymorphism. Identifying the formed polymorphs in thin films is essential to establish structure-property relationships and understand the mechanisms of charge transport. Additionally, thin film growth can result in metastable phases, unattainable under equilibrium conditions and non-existing in the single-crystalline form. Specifically, the solid surface can induce surface-induced polymorphism. That means that for some molecular materials, the substrate stabilizes a molecular packing that is different from that in the bulk phase structure. For each material, the crystallinity and morphology are influenced by kinetic and thermodynamic factors, necessitating the exploration of various growth parameters and post-growth treatments to optimize the electrical performance of thin film OFETs. These include the substrate temperature during growth and temperature of the thermal treatment performed after the growth of the films.

Polymorphism and the temperature behavior can directly affect device functional characteristics and temporal stability and remain a long-standing issue.

In π -conjugated organic semiconductor materials, heteroarenes with fused aromatic ring structures, such as [1]benzothieno[3,2-b]benzothiophene (BTBT) derivatives, have emerged as some of the most prominent organic semiconductors due to their excellent performance in organic field-effect transistors (OFETs). These materials exhibit charge carrier mobilities exceeding $10 \text{ cm}^2/\text{Vs}$ and possess exceptional air stability. Additionally, they can be applied in photodetectors/phototransistors or as donors in the formation of organic charge-transfer (CT) complexes. The high design versatility of BTBT derivatives allows for the realization of various symmetric and asymmetric alkylated BTBT molecular structures. In this study, we focus on dioctyl-BTBT (C8O-BTBT-OC8) and 7-decyl-2-phenyl[1]benzothieno[3,2-b][1]-benzothiophene (Ph-BTBT-10) as our research subjects because according to the state of the art at the start of this thesis, C8O-BTBT-OC8 exhibits a substrate-induced phase (SIP) different from its bulk structure when thin films are prepared by thermal evaporation or solution processing; Ph-BTBT-10 has been shown to exhibit two crystalline polymorphs in thin films, with the charge carrier mobility being closely depending on its molecular packing structure.

In this thesis, we combined surface characterization techniques such as synchrotron-based grazing incidence wide-angle X-ray scattering (GIWAXS), atomic force microscopy (AFM), and local Kelvin probe force microscopy (KPFM) to provide a systematic and detailed characterization of polymorphism in C8O-BTBT-OC8 and Ph-BTBT-10 thin films, with particular focus on the role of the interface. Based on our findings, we provide recommendations for optimizing and controlling film quality, which are of significant importance for enhancing the performance and reproducibility of organic field-effect transistor (OFET) devices.

Specifically:

- We used GIWAXS and AFM to characterize C8O-BTBT-OC8 thin films and to determine the impact of different substrate temperatures during growth and annealing treatments of films deposited at room temperature. We determined a structural transition from SIP to a high temperature polymorph (HTP) when the films are annealed at a temperature higher than 90 °C. We also concluded that the cooling rate affects the reversibility of the film structure. Growing films at an appropriate substrate temperature yields a smoother morphology, better suited for OFETs.
- We focus on the asymmetric BTBT derivative 7-decyl-2-phenyl[1]benzothieno[3,2-b][1]-benzothiophene (Ph-BTBT-10), which has attracted large interest in recent years due to its excellent charge carrier mobility. In thin films of Ph-BTBT-10 we discovered an important role of the surface as well as of the electrostatic interactions, giving rise to a complex thickness-dependent polymorphism. Films thinner than 20 nm exhibit a polar thin film structure, with strong impact on the electronic properties measured by KPFM and UV photoelectron spectroscopy (UPS). That structure in thin-films grown at room temperature is metastable.
- We monitored structural changes in Ph-BTBT-10 films of varying thicknesses in-situ during thermal annealing using KPFM and GIWAXS. We demonstrated the role of the interface in the Ph-BTBT-10 film structural transition occurring with thermal annealing, concluding that the transition from a single-layer (metastable) to a bilayer packing (thermodynamically stable) initiates at the film's bottom and extends to the top surface. As a consequence, for thinner films (<20 nm), there is a lower transition temperature to the thermodynamically stable bilayer structure, as well as a faster change at room temperature towards the bilayer structure with time.

Part I

FUNDAMENTALS

2

FUNDAMENTALS

This chapter introduces the fundamental background knowledge related to the topic of this thesis, including the materials used in the experiments.

2.1 Organic semiconductor materials

Organic semiconductors (OSCs) have garnered widespread attention since their discovery. Notably, in the 1970s, which was 30 years after the first organic semiconductor material emerged, researchers successfully synthesized NMP-TCNQ, which exhibited conductivity as high as that of metallic materials.[1],[2] Since then, there have been a large progress in the synthesis of new organic conjugated materials to be used as semiconductors in electronic applications.[3],[4],[5],[6],[7],[8] In 2000, Alan J. Heeger, Alan G. MacDiarmid, and Hideki Shirakawa, were awarded the Nobel Prize in Chemistry for their discovery in 1977 that polyacetylene doped with bromine or iodine vapor exhibits a high conductivity.[9]

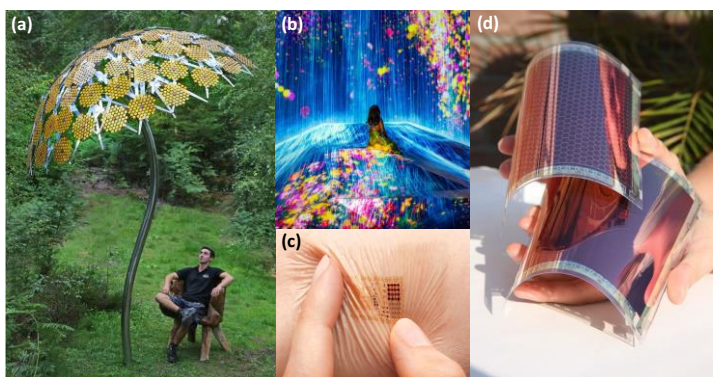


Figure 1. Recently application of organic semiconductors in different fields: (a) solar cells,[25] (b) OLED,[26] (c) wearable electronics,[27] (d) Bendable electronic.[28]

Compared to the covalent bonds in semiconductor crystals, the van der Waals bonding in organic semiconductor materials is weaker, which allows these materials to be processed at room temperature and atmospheric pressure using methods like solution processing, inkjet printing, and laser printing,[10],[11],[12] or by vacuum sublimation ($T < 250\text{ }^{\circ}\text{C}$). As a result, organic semiconductors can be applied to flexible substrates such as plastics,[13],[14],[15],[16],[17],[18],[19],[20],[21] textiles,[22] and paper.[12],[23],[24] This enables the use of organic electronic devices in areas where rigid electronic devices cannot be used, thus complementing existing silicon technology. Current implementations of organic semiconductor devices include organic photovoltaics (OPVs),[29],[30],[31],[32] sensors,[33],[34] organic light-emitting diodes (OLEDs),[35],[36] and organic field-effect transistors (OFETs).[37],[38] Figure 1 illustrates examples of applications of organic semiconductors.

Based on the molecular mass, OSCs can generally be categorized into two main types: polymers and small molecules. When deposited on a solid surface, compared to polymers, small molecule OSCs have the advantages of allowing long-range order and minimized structural defects, which contribute to their potential for high mobility. While polymers are restricted to solution processing, small molecules OSCs can be processed via solution or vacuum deposition.[39] Vacuum deposition (also known as Organic Molecular Beam Deposition (OMBD)) allows for precise control over the growth, resulting in high-quality films with controllable thickness and morphology and free of solvent molecules or chemical impurities. In addition, chemical design allows to optimize the performance of existing materials to meet specific needs (i.e. energy levels, solubility, optical spectrum).[40] Moreover, the continuous emergence of new organic semiconductor materials can bring surprising performance characteristics and new functionalities, which in turn motivate new applications.

2.1.1 Design strategy

As already mentioned, one reason organic semiconductor materials excite researchers is the possibility to continually design and synthesize new materials based on application needs.[41]

In general organic semiconductors consist on the following structural components: a conjugated core, heteroatoms, substituted functional groups, and alkyl side chains.[42] The π -conjugated core plays a decisive role in the material's primary physical properties because it determines the intra-molecular and inter-molecular interactions, thereby influencing physical characteristics such as energy band position and air stability.[37] For example, inter-molecular interactions will be affected by including heteroatoms and substituted functional groups with different electro negativities and steric hindrances. These interactions, in turn, influence the distribution of electron clouds between adjacent molecules, which ultimately plays a crucial role in inter-molecular charge transfer. Additionally, side chains,[43] functional substituted groups, and the length of the alkyl chains also impact the molecule's packing structure, solubility, and electrical properties.

Overall, the attributes of materials are not influenced solely by one element; they are shaped by a mixture of various elements. The significance of each element differs across different types of materials, thus requiring targeted analysis for each specific material.

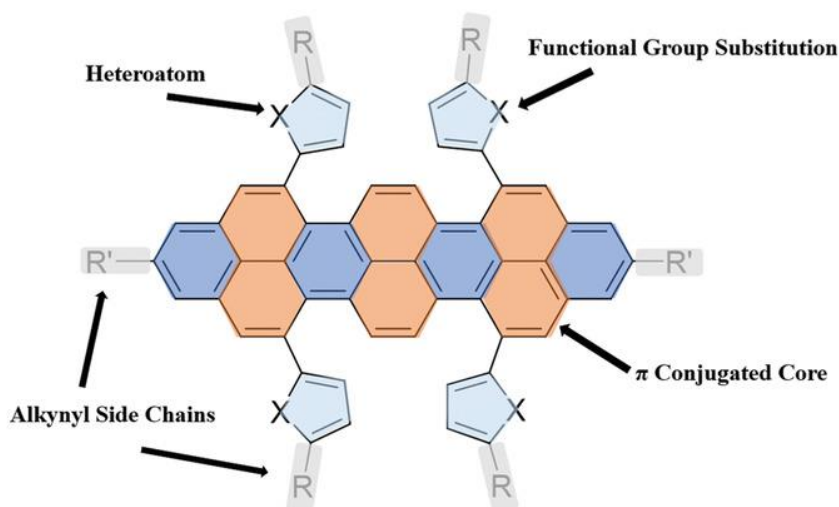


Figure 2. Schematic illustration for the key components of a typical OSCs molecules.[42]

2.1.2 Structure and polymorphism

The charge mobility in organic semiconductor films is not only related to the structure of individual molecules but also highly dependent on the arrangement of molecules in solid form and the resulting morphology of the film.[44] Relevant parameters such as π - π stacking mode, π - π distance, and π - π displacement all play a crucial role in charge transport. Generally, a large π - π orbital overlap, a short π - π distance, and optimal π - π displacement contribute to enhanced charge transport. [13],[37]

Based on the geometry of the molecular packing, π - π stacking motifs can be categorized into four types.[44],[37],[40] Before introducing these four motifs, let us clarify two concepts: the direction of π -stacking and the direction of lamellar-stacking. π -stacking occurs between conjugated groups, and lamellar stacking usually refers to the regular separation of the conjugated and aliphatic moieties.[45]

- Cofacial Stacking Motif (as shown in Figure 3a): In this configuration, molecules are aligned face-to-face in the π -stacking direction while adopting an edge-to-edge arrangement in the lamellar-stacking direction. This pattern

enhances π - π orbital overlap, facilitating intermolecular charge transfer, which is pivotal for effective conductivity.

- Slipped Stacking Motif (as shown in Figure 3b): This motif represents a variant of the cofacial structure, characterized by a significant misalignment in the lamellar-stacking direction. Here, molecules maintain an edge-to-edge orientation in the lamellar-stacking axis and an edge-to-face orientation in the π -stacking axis.
- Brick Layer Stacking Motif (as shown in Figure 3c): Extending the displacement observed in the slipped stacking motif within the lamellar-stacking direction results in the formation of a bricklayer stacking motif. This arrangement promotes additional structural irregularity, potentially influencing electronic properties.
- Herringbone Stacking Motif (as shown in Figure 3d): In this configuration, molecules are organized face-to-face along the π -stacking axis and face-to-edge along the lamellar-stacking axis. This dual-directional arrangement enhances the efficiency of carrier propagation in both the π -stacking and lamellar-stacking directions, thereby potentially increasing the conductivity of the films configured in this manner.

However, in practice, the molecular stacking does not always conform to the theoretical expectations. Variation in experimental conditions and parameters during thin-film growth, the type of substrate and subsequent post-growth treatments (e.g., annealing or solvent vapor annealing), can lead to strong differences in the structure and in the morphology.

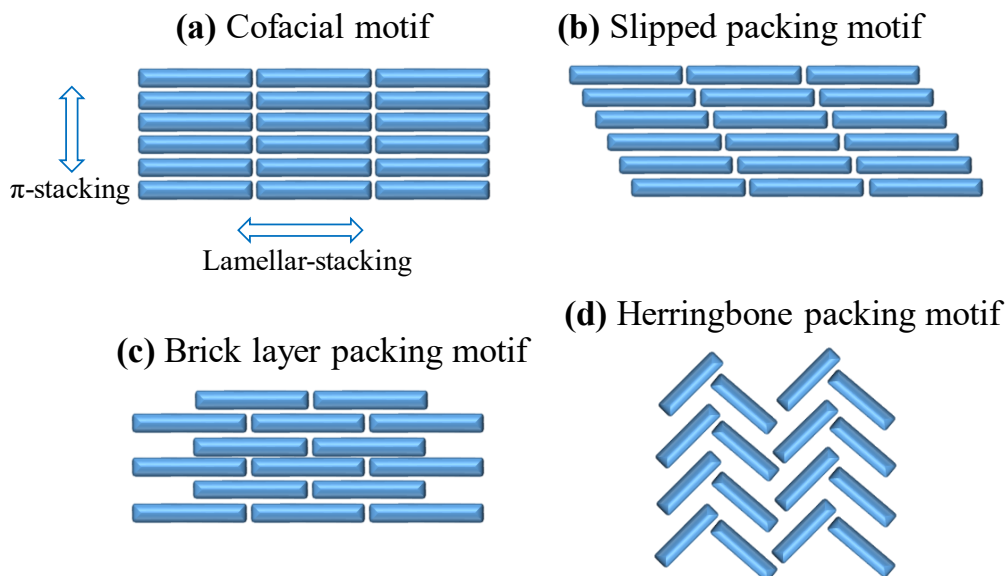


Figure 3. Four typical packing motifs existing in organic solid states: (a) Cofacial stacking, (b) Slipped stacking, (c) Brick layer stacking, (d) Herringbone stacking motif.

Polymorphism in organic semiconductor materials presents both advantages and disadvantages. The advantage is that polymorphism provides a valuable opportunity to study the relationship between charge transport properties within the film and the molecular stacking configuration and it can lead to new functionalities that not exist in the single crystal form. The disadvantage is that uncontrollable molecular-packing motifs during device fabrication may affect the performance, reproducibility and stability of the devices.[46],[47] Therefore, to achieve films that meet performance standards, it is crucial to control polymorphism.

For certain molecular materials, new polymorphic forms distinct from those observed in the bulk may exist near the interface with the substrate, referred to as substrate-induced phases (SIPs). These SIPs can extend over several molecular layers and do not necessarily correlate with any matching of unit cells between the film and the substrate. In our cases, the surfaces used as dielectric are amorphous (i.e SiO_2).

The most well-documented example of SIP is the thin-film phase of pentacene. The variations between pentacene polymorphs can be attributed to changes in the tilt of the

long molecular axis.[48] Different structures and morphologies were demonstrated depending on the growth conditions and the type of surface on which it is deposited. When deposited on graphene or metals such as Au or Cu, pentacene molecules typically lie flat on the substrate surface.[49],[50],[51] Conversely, when deposited on polymer surfaces, the molecules stand nearly upright, with a slight tilt of the long molecular axis away from the surface normal, depending on the specific polymorph present.[52],[53],[54],[55]

To date, three distinct substrate-induced phases (SIPs) of pentacene have been reported. On SiO_x substrates, an SIP with a characteristic (001) d-spacing of 15.4 Å has been observed.[56] A second SIP of pentacene, with a (001) d-spacing of 15.1 Å, has been identified on surfaces such as Kapton and NaCl.[50],[52] The third SIP of pentacene, with a (001) d-spacing of 13.5 Å, has been discovered in films coated onto polyimide nanogratings.[57]

2.2 BTBT derivatives

2.2.1 Historic development

In the vast array of heteroarenes, [1]benzothieno[3,2-b]benzothiophene (BTBT) is widely employed in the synthesis of new organic small molecule semiconductors. Discussion on the molecular structure of BTBT dates back to 1949 [58] and has been widely researched and discussed thereafter.[59],[60],[61],[62] The first successful application of a BTBT derivative in organic field-effect transistors (OFETs) was achieved with 2,7-Diphenyl[1]benzothieno[3,2-b][1]benzothiophene (DPh-BTBT). OFETs utilizing vapor-deposited DPh-BTBT thin films as the active layer exhibited an electron mobility of up to 2.0 cm²/Vs at room temperature.[63] Since this development, numerous new BTBT derivatives have been synthesized with the objective of enhancing OFET performance. The BTBT core comprises four consecutive aromatic rings. Despite its highly extended π -electron system, the highest occupied molecular orbital (HOMO) remains stable due to the sulfur atoms substituting for carbon atoms at the 5- and 10-

positions. Sulfur atoms exhibit larger HOMO coefficients compared to carbon atoms, enhancing intermolecular orbital overlap and facilitating charge transfer between molecules.[64] This qualitatively explains why BTBT derivatives possess good air stability and high mobility. Furthermore, besides the 5- and 10- positions, the remaining positions in the BTBT core can also be substituted with alkyl chains, benzene rings, methoxy groups, alkenyl groups, alkynyl groups, etc., providing the possibility of synthesizing numerous derivatives and laying a reliable foundation for the next generation of high-performance organic materials.[65],[66] Additionally, BTBT derivatives can interact with other π -electron acceptors, such as n-type TCNQ, F2TCNQ, and F4TCNQ, to form co-crystal structures that exhibit novel properties.[67]

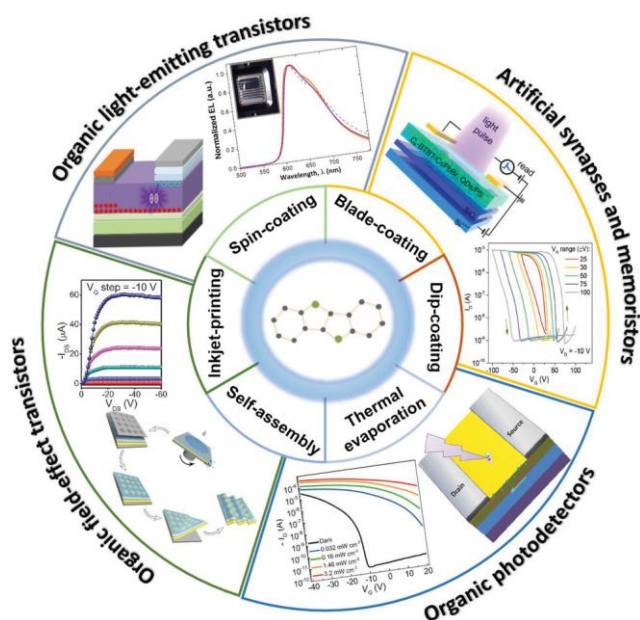


Figure 4. Schematic of fabrication techniques and applications of BTBT-based electronic and optoelectronic devices.[60]

In summary, due to its low-lying HOMO level, good air stability, high electron mobility, and potential for synthesizing numerous derivatives, BTBT derivatives find widespread applications in organic field-effect transistors (OFETs), photodetectors, phototransistors, solar cells, etc. (As shown in Figure 4)[60]

In Cn-BTBT-Cn derivatives, the molecules adopt a lamella stacking with a HB packing of the cores. Such packing is denominated layer herringbone (LHB) packing. As shown in Figure 5, the alkyl layers and BTBT layers follow a lamella-like alternating structure (Figure 5a), with a herringbone arrangement of the BTBT cores (Figure 5b).[68] The LHB packing ensures both, high charge mobility and structural stability of the π -conjugated system. Studies suggest that both symmetric and asymmetric molecular structures tend to exhibit LHB packing when the alkyl chain is relatively long ($n \geq 4$ for monoalkylated, $n \geq 6$ for dialkylated, and $n \geq 5$ for phenyl-alkylated BTBTs).[69] However, with shorter alkyl chains, the disorderliness of the intra-chain disrupts layer-by-layer or LHB packing, resulting in T-shaped (core-to-edge) or slipped parallel (core-to-core) molecular stacking structures rather than LHB packing.[70],[71] Furthermore, the length of the alkyl chain determines the interlayer distance (d-spacing); longer alkyl chains lead to greater interlayer distances and thus larger d-spacing.

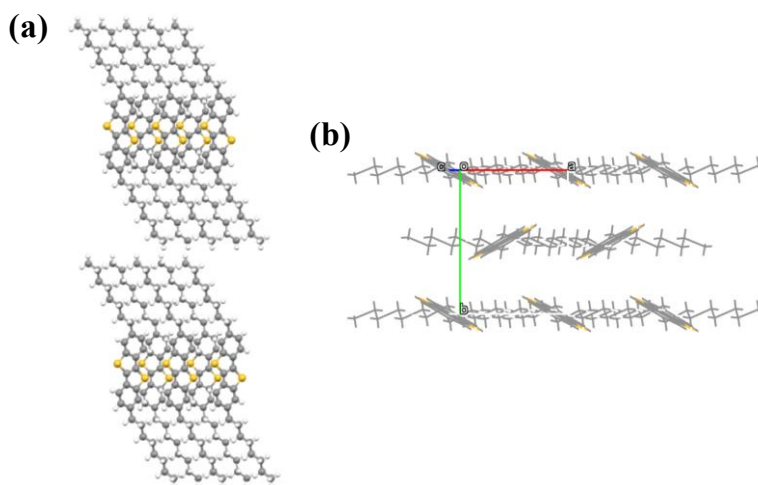


Figure 5. Crystal structure of SIP in C8-BTBT-C8 thin films. (a) from side view, (b) from top view.

Kobayashi et al. reported that in BTBT derivatives, electron transport primarily occurs in a band-like manner.[72] Moreover, in solution preparation process the hydrophobic interaction between alkyl chains enhances intermolecular interactions, further reinforcing its band-like transport characteristics.[73] Two main factors influencing the mobility of charge carriers are the strong electronic coupling between adjacent

molecules and small intramolecular reorganization energy.[79] Therefore, in the BTBT core, sulfur atoms enhance intermolecular interactions and overlap, while the herringbone stacking mode strengthens coupling between molecules, promoting charge carrier mobility.

In BTBT derivatives, extending π -conjugated backbones along the long axis enhances both intermolecular electronic coupling and molecular rigidity. Additionally, a network of sulfur-sulfur and C-H... π contacts between molecules effectively suppresses lattice vibrations, endowing BTBT derivatives with high thermal stability potential.[80]

In Figure 6 we list several common BTBT derivatives and their carrier motilities in thin film, including C8O-BTBT-OC8 and Ph-BTBT-10, which we will explain in detail later. It is noteworthy that the hole mobility of OTFTs using solution-processed C8-BTBT-C8 thin films was reported to reach up to 43 cm²/Vs (with an average of 25 cm²/Vs), making it the highest mobility reported for organic molecules to date.[74]

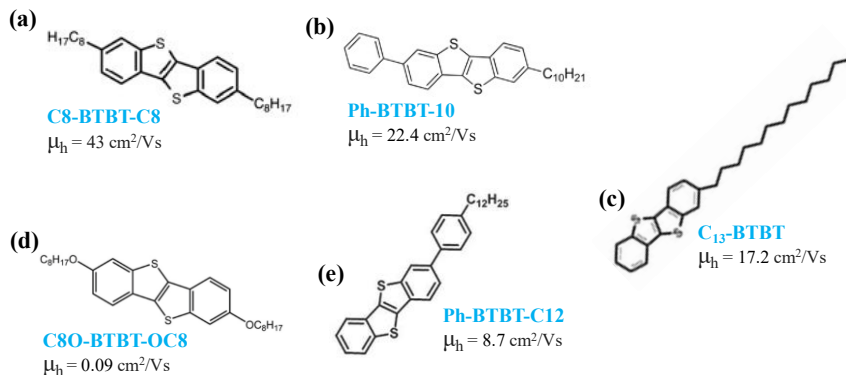


Figure 6. Examples of some common BTBT derivatives and their motilities. (a) C8-BTBT-C8,[74] (b) Ph-BTBT-10,[75] (c) C13-BTBT,[76] (d) C8O-BTBT-OC8,[77] (e) Ph-BTBT-C12.[78]

2.2.2 C8O-BTBT-OC8

Here we introduce one of the main research subjects in this thesis, dioctyl-BTBT (C8O-BTBT-OC8) (shown in Figure 7).

C8O-BTBT-OC8 is one of the BTBT derivatives that has been extensively researched in recent years.[81],[82],[83] It has larger thermal stability than C8-BTBT-C8, and its solubility and ease of preparation render it promising for applications in printing techniques.[84] Reports indicate that the charge mobility of thin films of C8O-BTBT-OC8 can reach up to $0.09 \text{ cm}^2/\text{Vs}$. [81] The molecular length is 33.88 \AA , [85] the HOMO level is -5.22 eV (Cyclic Voltammetry (CV)) or -5.39 eV (Ultra-Violet Photoelectron Spectroscopy (UPS)). [84] It is already well known that C8O-BTBT-OC8 exhibits two polymorphs: the surface-induced phase (SIP) and the bulk phase, with distinct packing arrangements. In the bulk phase (thermodynamically stable), molecules are in layered π - π stacking. However, when deposited on a surface, the molecules adopt the SIP phase, with the same LHB packing motif as for C8-BTBT-C8 (see in Figure 7b and 7c). [86] According to literature, the SIP structure is metastable and undergoes a transition into the bulk phase with aging over six months at room temperature, and solvent vapor annealing can expedite this phase transition within few days. [87] Due to this feature, the performance and stability of devices based solely on pure C8O-BTBT-OC8 films may be affected by the spontaneous transition from SIP to bulk phase, thereby impacting device electrical performance. Reports have shown that blending C8O-BTBT-OC8 with polystyrene (PS) enhances the stability of SIP, consequently improving device performance and long-term stability. In fact, devices have maintained high performance for over 1.5 years. [81]

Additionally, thermal stability is a crucial characteristic influencing material applications, as post-annealing is a widely used treatment method to enhance thin film quality. Therefore, understanding and studying the thermal stability of polymorphs is essential for effective annealing.

In this thesis, we investigated the effect of annealing on the structure and morphology. Detailed findings will be presented in Chapter 4.

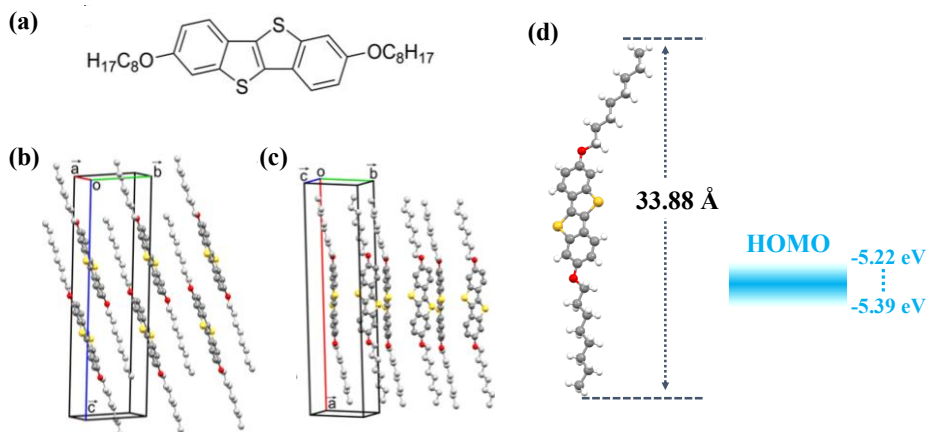


Figure 7. (a) Chemical structure of C8O-BTBT-OC8; Molecular packing in the (b) bulk phase (single-crystalline form) and (c) SIP in thin films;[86] (d) Molecular length and HOMO level (measured by CV and UPS).

2.2.3 Ph-BTBT-10

In this section, we introduce another subject of our study in this thesis: 2-Decyl-7-phenyl[1]benzothieno[3,2-b][1]benzothiophene (Ph-BTBT-10).

Ph-BTBT-10 consists of a benzothienobenzothiophene (BTBT) core attached to a phenyl group and a decyl chain.[88] The molecule has a length of 2.65 Å and a HOMO level of -5.65 eV, as determined by cyclic voltammetry (CV).[89] This material has garnered attention due to its excellent air stability, thermal stability of films up to 200 °C, high carrier mobility exceeding 10 cm²/Vs, and its suitability for solution processing, which makes it promising for printed electronics applications.[88]

In the bulk the molecule crystallizes into a double-layered structure (bilayer structure) with the conjugated parts and decyl parts segregated. The conjugated cores adopt a herringbone pattern, characteristic of the packing of other BTBT derivatives (Figure 5). Thus, the bilayer structure consists of two adjacent herringbone layers, with alkyl-up and alkyl-down orientation, yielding an interplanar distance of 5.3 nm. The packing arrangement of the molecules in the bulk phase is illustrated in Figure 8c.[85] The molecules adopt a different structure in thin films. During the preparation of thin films

using the physical vapor deposition method, it was observed that the molecules form a double layer on the silicon substrate at the initial film growth stage, with a stage height of 5.3 nm (as see Figure 8b). Subsequently, the molecules adopt a single-layer lamellar packing with an interplanar distance of 2.65 nm (i.e. half bilayer), which is a metastable phase.[85] The reported structure of the thin-film phase is shown in the Figure 8c. After post-annealing at 115 °C, a phase transition occurs from the single-layer to the bilayer packing (bulk phase). Upon further increasing the annealing temperature to 146 °C, another phase transition occurs from the bilayer phase to the crystalline smectic E (SmE) phase, which remains stable up to 210 °C. At an annealing temperature of 215 °C, the film transitions to a highly flat single-layer structure corresponding to the SmA liquid crystalline phase.

Notably, when the film is heated to a temperature near the transition to the liquid crystalline phase, a flip-flop behavior of the molecules in the bilayer structure has been reported, leading to disorder in the film packing.[90]

Additionally, there has been considerable research on applying Ph-BTBT-10 in device fabrication. Hiroaki Lino et al. reported that the highest carrier mobility ($13.9 \text{ cm}^2/\text{Vs}$) is achieved when Ph-BTBT-10 packs in the bilayer structure.[88] Furthermore, Takamasa Hamai et al. reported that organic thin-film transistors (OTFTs) based on the Ph-BTBT-10 bilayer structure exhibit a layer-number dependent device mobility and current-voltage characteristics. They proposed that paired alkyl-chain layers within the single-crystalline film provide higher tunneling resistance than an unpaired alkyl-chain layer on the film surface. This results in device resistance being proportional to the layer number, thus impacting the overall device performance.[91]

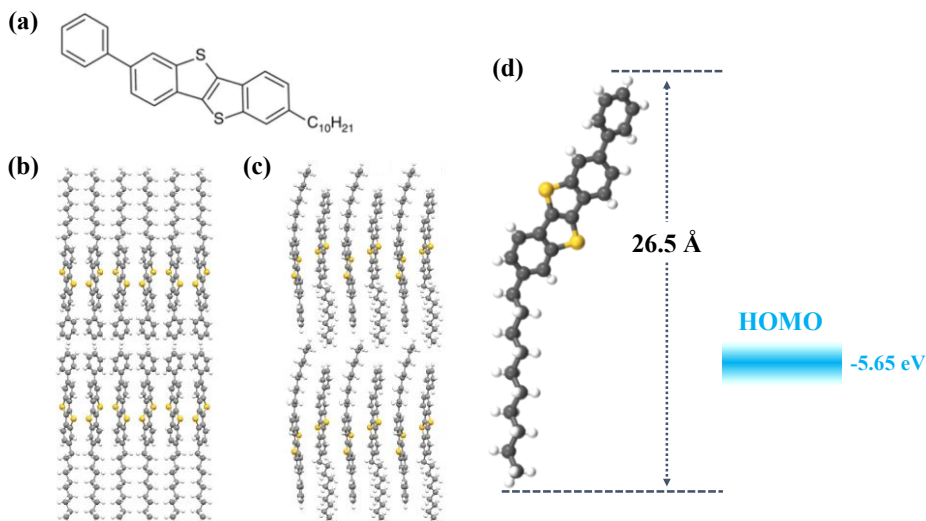


Figure 8. (a) chemical structure of Ph-BTBT-C10; (b) Bi-Layer packing structure and (c) Single-Layer packing structure; (d) Molecular length and HOMO level.

In summary, since the electron mobility of Ph-BTBT-10 thin films is closely linked to the molecular packing structure, studying, understanding, and controlling its polymorphism is crucial. In this thesis, we have identified a new packing structure, termed the thin film polar phase, in addition to the previously reported polymorphisms of Ph-BTBT-10. Detailed findings will be presented in Chapter 5.

2.3 OFETS

2.3.1 Basic Concept

Silicon-based transistors have revolutionized modern electronic technology, playing a crucial role not only in shaping the technologies that impact our personal lives but also in a wide range of industries such as transportation, communication, manufacturing, engineering, medicine, energy, defense, and national security.

Organic field-effect transistors (OFETs) typically consist of three main components: organic semiconductor material, a gate dielectric, and electrodes (including gate, source, and drain). These components can be configured into two types of devices: coplanar and

staggered. In coplanar devices, the source, drain, and conducting channel are located on the same plane, while in staggered devices, the conducting channel is not on the same plane as the source and drain contacts. These configurations can further be divided into four device architectures: bottom gate, bottom contacts (BGBC) (as shown in Figure 9a); bottom gate, top contacts (BGTC) (as shown in Figure 9b); top gate, bottom contacts (TGBC) (as shown in Figure 9c); and top gate, top contacts (TGTC) (as shown in Figure 9d).

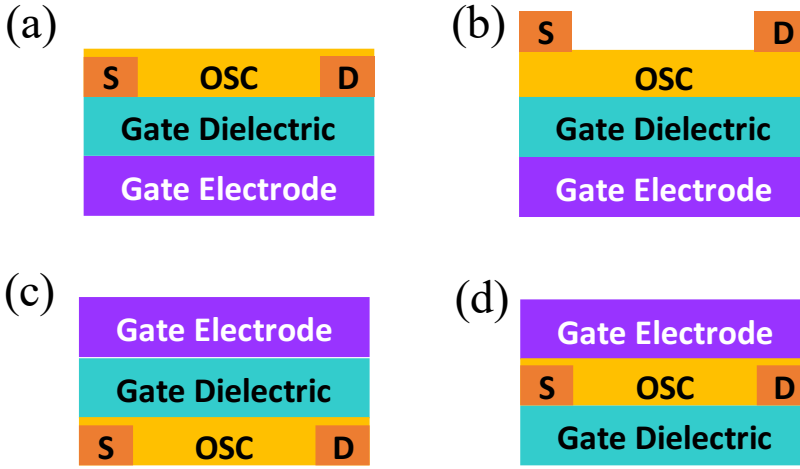


Figure 9. OFET device architecture: (a) bottom gate, bottom contact, (b) bottom gate, top contact, (c) top gate, bottom contact, and (d) top gate, top contact.

Each architecture has its advantages and disadvantages. In this paper, we primarily focus on the bottom gate, top contacts (BGTC) structure. This choice is based on current reports indicating that top contact devices exhibit lower contact resistance compared to other structures. This is attributed to the direct deposition of metal electrodes on the organic semiconductor layer, which facilitates easier migration of metal atoms to the boundary of the crystalline organic thin film, thereby reducing contact resistance.[92] Furthermore, the bottom gate configuration results in a staggered structure between the gate and contacts, providing a larger charge injection area and enhancing charge injection efficiency.[93]

There are several key parameters used to evaluate the performance of organic field-effect transistors (OFETs):

- Field-effect mobility: This value determines whether OFETs can be commercially viable and the domains in which they can be applied. High mobility is a target in device development because it enhances the performance and commercial applicability of the transistors. Generally, when the carrier mobility (μ) of the device is larger than $1\text{cm}^2/\text{Vs}$ can be considered to have high carrier mobility.
- Threshold voltage (V_{Th}): This parameter represents the operating voltage of the device. A lower V_{Th} indicates that the device requires less voltage to activate, making it more energy-efficient. From a cost-efficiency perspective, it is desirable for the V_{Th} to be close to 0 V.
- Subthreshold swing (S): This parameter reflects the concentration of traps in the organic semiconductor film. A smaller S value indicates a faster switching speed for the device. An acceptable subthreshold swing is typically around 1V/dec, with some high-performance devices even achieving values less than 0.5 V/dec. For instance, Liu et al. reported that the subthreshold swing (SS) value of negative capacitance field-effect transistors (NCFETs) based on MoS₂ can reach as low as 42.5 mV/dec.[94]

Additionally, parameters such as the on/off current ratio are also important; for further reading, we recommend some reviews about OFETs.[92],[95]

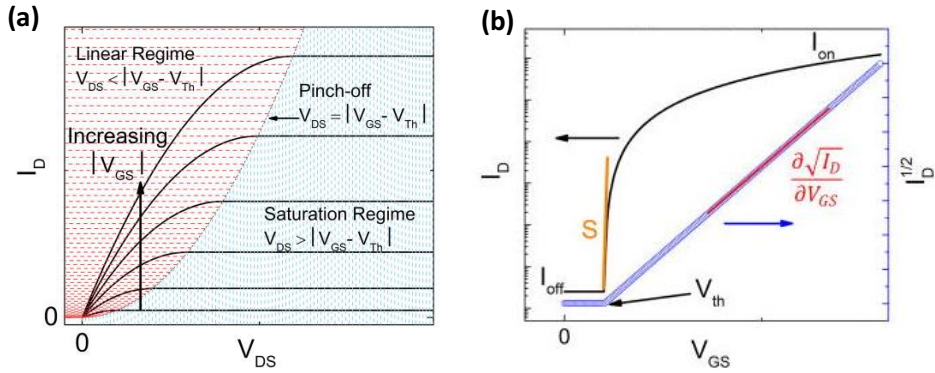


Figure 10. Ideal OFET output characteristics (a), and transfer curve in saturation region(b).[92]

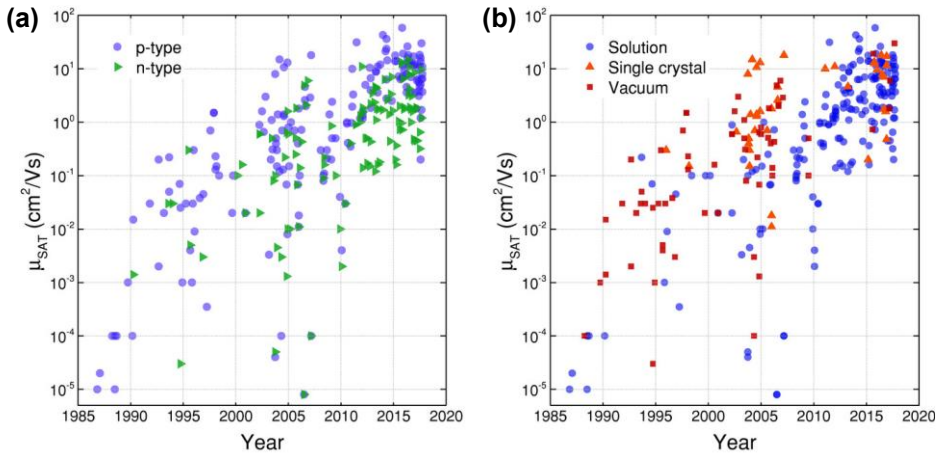


Figure 11. This graph shows the change over time in the field effect mobility values, which are divided into two categories: (a) Charge carrier type: p-type and n-type. (b) Processing technique: solution processed, single crystal, and vacuum.[95]

Field-effect mobility is the primary metric for evaluating the performance of organic field-effect transistors (OFETs). The graph above (Figure 11) summarizes the mobilities reported for OFETs over the past 35 years, categorized by the type of organic semiconductor material or the method of fabrication. Figure 11a indicates that the carrier mobilities of devices based on n-type organic semiconductor materials are gradually catching up to those of p-type organic semiconductor devices.

Figure 11b shows the variations in carrier mobility that can result from different fabrication methods. The data suggest that the method of preparing organic materials does not significantly impact mobility, with similar values observed for solution-processed, single crystal, and vacuum-processed devices. However, devices processed via solution generally exhibit somewhat higher mobilities.

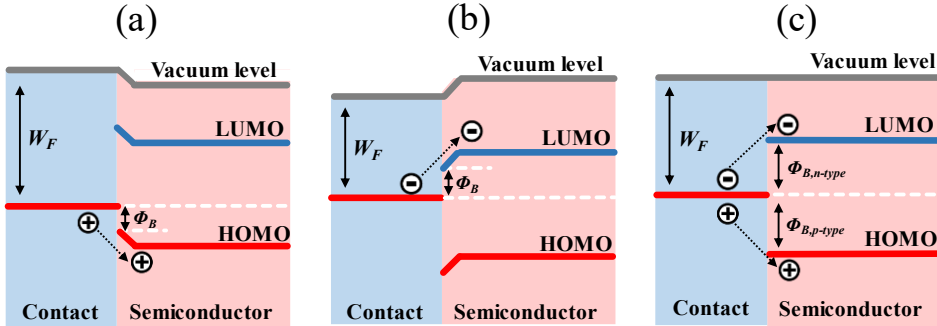


Figure 12: The injection barrier Φ_B is the difference between the work function of contact and the corresponding semiconductor band. (a) Holes are injected into the semiconductor HOMO in a p-type device. The proximity of W_F to the HOMO level causes energy level bending, shifting the level from its nominal value at the interface. (b) Electrons are injected into the semiconductor LUMO in a n-type device. (c) A work function in between the HOMO and LUMO levels can facilitate am-bipolar transport, though injection barriers will always be larger than in the corresponding unipolar device. Energy level bending is minimal when W_F is near the Fermi level of the semiconductor.[92]

For an organic field-effect transistor (OFET) to achieve good device performance, high charge injection efficiency is essential. Charge injection primarily depends on the alignment of the work function between the electrode's contact work function (W_F) and the semiconductor's highest occupied molecular orbital (HOMO) or lowest unoccupied molecular orbital (LUMO) levels. Aligning the contact work function with the semiconductor's HOMO/LUMO levels is not straightforward because the work function is a surface property of the material and is subject to environmental effects. For p-type channels, the injection barrier (Φ_B) mainly depends on the difference between the contact's W_F and the semiconductor's HOMO level (or between the W_F and the LUMO for n-type channels). This relationship can be influenced by several complex factors,

such as the formation of interface dipoles or the molecular orientation at the interface. To enhance charge injection, in addition to selecting semiconductor materials and contacts with matching energy levels, chemical modification is a common approach. For example, electrodes can be modified with polar self-assembled monolayers (SAMs).[92]

Energy bending alignment is a key phenomenon occurring at interfaces. When materials with different Fermi levels come into contact, charge transfer occurs until thermodynamic equilibrium is achieved, resulting in a common Fermi level. The resulting charges generate an electrostatic field near the interface, inducing a vacuum-level shift to align the Fermi levels. The figure below illustrates and explains the band bending phenomenon present in different types of devices.

Figure 12a illustrates a p-type device where the HOMO level of the electrode is higher than that of the semiconductor material. At the interface, holes are injected from the electrode into the semiconductor's HOMO, causing an upward bending of the HOMO level and effectively raising the energy level at the contact interface. Figure 12b depicts an n-type device where the electrode's LUMO level is lower than that of the organic semiconductor. At the interface, electrons flow from the electrode into the semiconductor's LUMO, leading to a downward bending of the LUMO level and lowering the energy level at the interface. Figure 12c presents a situation where the electrode's work function is positioned between the HOMO and LUMO levels of the organic semiconductor. This alignment can facilitate ambipolar transport, as detailed in the accompanying illustration.

Contact resistance is another crucial factor that needs to be considered. Contact resistance can be understood as the finite voltage required to transfer charges from the electrode surface into the semiconductor and vice versa. Typically, the resistance due to the contacts must be lower than the resistance due to the channel. If this condition is not met, the voltage drop at the contacts results in a smaller effective potential across the channel, leading to excessive power loss and reduced field-effect mobility. Several variables can affect the contact resistance (RC) in OFETs. These include the energy

levels of the organic semiconductor (OSC), the packing ordering of the OSC, and the material of the contact electrodes.[96] Many methods have been researched and employed to minimize the contact resistance of devices. From a microstructural perspective, enhancing the packing order of the OSC can be effective. From an energy level perspective, reducing the height of the Schottky barrier is beneficial. This can be achieved, for example, by using thiol-based self-assembled monolayers (SAMs) or adding a charge injection layer between the injecting contacts and the OSC.[97],[98] In addition, layer doping is also a commonly used and effective method to enhance carrier injection in electronics.[99]

References

- [1] A. J. Epstein, S. Etemad, A. Garito, and et A. Heeger, 'Metal-insulator transition and antiferromagnetism in a one-dimensional organic solid', *Phys. Rev. B*, vol. 5, no. 3, p. 952, 1972.
- [2] John. Ferraris, D. O. Cowan, V. Walatka, and J. H. Perlstein, 'Electron transfer in a new highly conducting donor-acceptor complex', *J. Am. Chem. Soc.*, vol. 95, no. 3, pp. 948–949, Feb. 1973, doi: 10.1021/ja00784a066.
- [3] D. Liu *et al.*, 'Integrating Unexpected High Charge-Carrier Mobility and Low-Threshold Lasing Action in an Organic Semiconductor', *Angew. Chem.*, vol. 134, no. 25, p. e202200791, 2022, doi: <https://doi.org/10.1002/ange.202200791>.
- [4] H. E. Katz *et al.*, 'A soluble and air-stable organic semiconductor with high electron mobility', *Nature*, vol. 404, no. 6777, pp. 478–481, Mar. 2000, doi: 10.1038/35006603.
- [5] W. Li, H. E. Katz, A. J. Lovinger, and J. G. Laquindanum, 'Field-effect transistors based on thiophene hexamer analogues with diminished electron donor strength', *Chem. Mater.*, vol. 11, no. 2, pp. 458–465, 1999.
- [6] K. Takimiya *et al.*, "'Manipulation" of Crystal Structure by Methylthiolation Enabling Ultrahigh Mobility in a Pyrene-Based Molecular Semiconductor', *Adv. Mater.*, vol. 33, no. 32, p. 2102914, 2021.
- [7] K. Feng *et al.*, 'Cyano-Functionalized n-Type Polymer with High Electron Mobility for High-Performance Organic Electrochemical Transistors', *Adv. Mater.*, vol. 34, no. 24, p. 2201340, 2022.
- [8] Q. Shi *et al.*, 'Synthetic Routes for Heteroatom-Containing Alkylated/Arylated Polycyclic Aromatic Hydrocarbons', *Angew. Chem.*, vol. 133, no. 6, pp. 2960–2964, 2021.
- [9] H. Shirakawa, E. J. Louis, A. G. MacDiarmid, C. K. Chiang, and A. J. Heeger, 'Synthesis of electrically conducting organic polymers: halogen derivatives of polyacetylene,(CH) x', *J. Chem. Soc. Chem. Commun.*, no. 16, pp. 578–580, 1977.
- [10] H. Sirringhaus *et al.*, 'High-resolution inkjet printing of all-polymer transistor circuits', *Science*, vol. 290, no. 5499, pp. 2123–2126, 2000.

- [11]T. Sekitani, Y. Noguchi, U. Zschieschang, H. Klauk, and T. Someya, ‘Organic transistors manufactured using inkjet technology with subfemtoliter accuracy’, *Proc. Natl. Acad. Sci.*, vol. 105, no. 13, pp. 4976–4980, 2008.
- [12]P. J. Diemer *et al.*, ‘Laser-Printed Organic Thin-Film Transistors’, *Adv. Mater. Technol.*, vol. 2, no. 11, p. 1700167, 2017.
- [13]M. Medina-Sánchez, C. Martínez-Domingo, E. Ramon, and A. Merkoçi, ‘An Inkjet-Printed Field-Effect Transistor for Label-Free Biosensing’, *Adv. Funct. Mater.*, vol. 24, no. 40, pp. 6291–6302, 2014.
- [14]Y. Xu, R. Gwoziecki, I. Chartier, R. Coppard, F. Balestra, and G. Ghibaudo, ‘Modified transmission-line method for contact resistance extraction in organic field-effect transistors’, *Appl. Phys. Lett.*, vol. 97, no. 6, 2010.
- [15]T. Kubo *et al.*, ‘Suppressing molecular vibrations in organic semiconductors by inducing strain’, *Nat. Commun.*, vol. 7, no. 1, p. 11156, 2016.
- [16]C. Reese, W.-J. Chung, M. Ling, M. Roberts, and Z. Bao, ‘High-performance microscale single-crystal transistors by lithography on an elastomer dielectric’, *Appl. Phys. Lett.*, vol. 89, no. 20, 2006.
- [17]W. Xie *et al.*, ‘Temperature-independent transport in high-mobility dinaphtho-thieno-thiophene (DNTT) single crystal transistors.’, *Adv. Mater. Deerfield Beach Fla*, vol. 25, no. 25, pp. 3478–3484, 2013.
- [18]D. Ji *et al.*, ‘Large scale, flexible organic transistor arrays and circuits based on polyimide materials’, *Org. Electron.*, vol. 14, no. 10, pp. 2528–2533, 2013.
- [19]Y. Zang, F. Zhang, D. Huang, X. Gao, C. Di, and D. Zhu, ‘Flexible suspended gate organic thin-film transistors for ultra-sensitive pressure detection’, *Nat. Commun.*, vol. 6, no. 1, p. 6269, 2015.
- [20]H. T. Yi, M. M. Payne, J. E. Anthony, and V. Podzorov, ‘Ultra-flexible solution-processed organic field-effect transistors’, *Nat. Commun.*, vol. 3, no. 1, p. 1259, 2012.
- [21]J. A. Rogers, T. Someya, and Y. Huang, ‘Materials and mechanics for stretchable electronics’, *science*, vol. 327, no. 5973, pp. 1603–1607, 2010.
- [22]K. Cherenack and L. Van Pieterse, ‘Smart textiles: Challenges and opportunities’, *J. Appl. Phys.*, vol. 112, no. 9, 2012.

- [23] T. Minari *et al.*, ‘Room-Temperature Printing of Organic Thin-Film Transistors with π -Junction Gold Nanoparticles’, *Adv. Funct. Mater.*, vol. 24, no. 31, pp. 4886–4892, 2014.
- [24] U. Zschieschang and H. Klauk, ‘Low-voltage organic transistors with steep subthreshold slope fabricated on commercially available paper’, *Org. Electron.*, vol. 25, pp. 340–344, 2015.
- [25] ‘Picture of solar cells’. [Online]. Available: <https://www.pinterest.es/pin/971933163321801762/>.
- [26] *OLED*. [Online]. Available: <http://www.stellalee.net/2018/06/mori-building-digital-art-museum.html?m=1>
- [27] *Wearable electronics*. [Online]. Available: <https://www.dezeen.com/2013/03/28/biostamp-temporary-tattoo-wearable-electronic-circuits-john-rogers-mc10/>
- [28] *Bendable electronic*. [Online]. Available: <https://i.pinimg.com/736x/b1/cc/c5/b1ccc5a3691690c12383e395111a0cea.jpg>
- [29] Y.-W. Su, S.-C. Lan, and K.-H. Wei, ‘Organic photovoltaics’, *Mater. Today*, vol. 15, no. 12, pp. 554–562, 2012.
- [30] G. Li, R. Zhu, and Y. Yang, ‘Polymer solar cells’, *Nat. Photonics*, vol. 6, no. 3, pp. 153–161, 2012.
- [31] Y.-J. Cheng, S.-H. Yang, and C.-S. Hsu, ‘Synthesis of conjugated polymers for organic solar cell applications’, *Chem. Rev.*, vol. 109, no. 11, pp. 5868–5923, 2009.
- [32] L. Lu, T. Zheng, Q. Wu, A. M. Schneider, D. Zhao, and L. Yu, ‘Recent advances in bulk heterojunction polymer solar cells’, *Chem. Rev.*, vol. 115, no. 23, pp. 12666–12731, 2015.
- [33] L. Torsi, M. Magliulo, K. Manoli, and G. Palazzo, ‘Organic field-effect transistor sensors: a tutorial review’, *Chem. Soc. Rev.*, vol. 42, no. 22, pp. 8612–8628, 2013.
- [34] P. Lin and F. Yan, ‘Organic thin-film transistors for chemical and biological sensing’, *Adv. Mater.*, vol. 24, no. 1, pp. 34–51, 2012.

- [35]K. Baeg, M. Binda, D. Natali, M. Caironi, and Y. Noh, ‘Organic light detectors: photodiodes and phototransistors’, *Adv. Mater.*, vol. 25, no. 31, pp. 4267–4295, 2013.
- [36]J. Mei, Y. Hong, J. W. Lam, A. Qin, Y. Tang, and B. Z. Tang, ‘Aggregation-induced emission: the whole is more brilliant than the parts’, *Adv. Mater.*, vol. 26, no. 31, pp. 5429–5479, 2014.
- [37]C. Wang, H. Dong, W. Hu, Y. Liu, and D. Zhu, ‘Semiconducting π -conjugated systems in field-effect transistors: a material odyssey of organic electronics’, *Chem. Rev.*, vol. 112, no. 4, pp. 2208–2267, 2012.
- [38]H. Sirringhaus, ‘25th anniversary article: organic field-effect transistors: the path beyond amorphous silicon’, *Adv. Mater.*, vol. 26, no. 9, pp. 1319–1335, 2014.
- [39]X. Song *et al.*, ‘A Highly Crystalline Fused-Ring n-Type Small Molecule for Non-Fullerene Acceptor Based Organic Solar Cells and Field-Effect Transistors’, *Adv. Funct. Mater.*, vol. 28, no. 35, p. 1802895, 2018.
- [40]H. Jiang *et al.*, ‘High-performance five-ring-fused organic semiconductors for field-effect transistors’, *Chem. Soc. Rev.*, vol. 51, no. 8, pp. 3071–3122, 2022.
- [41]H. Bronstein, C. B. Nielsen, B. C. Schroeder, and I. McCulloch, ‘The role of chemical design in the performance of organic semiconductors’, *Nat. Rev. Chem.*, vol. 4, no. 2, pp. 66–77, 2020.
- [42]L. Bai, N. Wang, and Y. Li, ‘Controlled Growth and Self-Assembly of Multiscale Organic Semiconductor’, *Adv. Mater.*, vol. 34, no. 22, p. 2102811, Jun. 2022, doi: 10.1002/adma.202102811.
- [43]H. Chung, S. Chen, B. Patel, G. Garbay, Y. H. Geerts, and Y. Diao, ‘Understanding the role of bulky side chains on polymorphism of btbt-based organic semiconductors’, *Cryst. Growth Des.*, vol. 20, no. 3, pp. 1646–1654, 2020.
- [44]M. Mas-Torrent and C. Rovira, ‘Role of molecular order and solid-state structure in organic field-effect transistors’, *Chem. Rev.*, vol. 111, no. 8, pp. 4833–4856, 2011.
- [45]Z.-F. Yao, J.-Y. Wang, and J. Pei, ‘Control of π – π stacking via crystal engineering in organic conjugated small molecule crystals’, *Cryst. Growth Des.*, vol. 18, no. 1, pp. 7–15, 2018.

- [46] A. Troisi and G. Orlandi, ‘Band structure of the four pentacene polymorphs and effect on the hole mobility at low temperature’, *J. Phys. Chem. B*, vol. 109, no. 5, pp. 1849–1856, 2005.
- [47] A. A. Günther, J. Widmer, D. Kasemann, and K. Leo, ‘Hole mobility in thermally evaporated pentacene: Morphological and directional dependence’, *Appl. Phys. Lett.*, vol. 106, no. 23, 2015.
- [48] A. O. F. Jones, B. Chattopadhyay, Y. H. Geerts, and R. Resel, ‘Substrate-Induced and Thin-Film Phases: Polymorphism of Organic Materials on Surfaces’, *Adv. Funct. Mater.*, vol. 26, no. 14, pp. 2233–2255, 2016, doi: <https://doi.org/10.1002/adfm.201503169>.
- [49] D. Käfer, L. Ruppel, and G. Witte, ‘Growth of pentacene on clean and modified gold surfaces’, *Phys Rev B*, vol. 75, no. 8, p. 085309, Feb. 2007, doi: 10.1103/PhysRevB.75.085309.
- [50] N. Koch *et al.*, ‘Adsorption-Induced Intramolecular Dipole: Correlating Molecular Conformation and Interface Electronic Structure’, *J. Am. Chem. Soc.*, vol. 130, no. 23, pp. 7300–7304, Jun. 2008, doi: 10.1021/ja800286k.
- [51] W. H. Lee *et al.*, ‘Surface-Directed Molecular Assembly of Pentacene on Monolayer Graphene for High-Performance Organic Transistors’, *J. Am. Chem. Soc.*, vol. 133, no. 12, pp. 4447–4454, Mar. 2011, doi: 10.1021/ja1097463.
- [52] C. C. Mattheus *et al.*, ‘Identification of polymorphs of pentacene’, *Synth. Met.*, vol. 138, no. 3, pp. 475–481, 2003, doi: [https://doi.org/10.1016/S0379-6779\(02\)00467-8](https://doi.org/10.1016/S0379-6779(02)00467-8).
- [53] B. Stadlober, U. Haas, H. Maresch, and A. Haase, ‘Growth model of pentacene on inorganic and organic dielectrics based on scaling and rate-equation theory’, *Phys Rev B*, vol. 74, no. 16, p. 165302, Oct. 2006, doi: 10.1103/PhysRevB.74.165302.
- [54] S. Nishikata *et al.*, ‘Polycrystalline domain structure of pentacene thin films epitaxially grown on a hydrogen-terminated Si(111) surface’, *Phys Rev B*, vol. 76, no. 16, p. 165424, Oct. 2007, doi: 10.1103/PhysRevB.76.165424.
- [55] H. S. Lee, D. H. Kim, J. H. Cho, M. Hwang, Y. Jang, and K. Cho, ‘Effect of the Phase States of Self-Assembled Monolayers on Pentacene Growth and Thin-Film Transistor Characteristics’, *J. Am. Chem. Soc.*, vol. 130, no. 32, pp. 10556–10564, Aug. 2008, doi: 10.1021/ja800142t.

- [56] C. D. Dimitrakopoulos, A. R. Brown, and A. Pomp, 'Molecular beam deposited thin films of pentacene for organic field effect transistor applications', *J. Appl. Phys.*, vol. 80, no. 4, pp. 2501–2508, Aug. 1996, doi: 10.1063/1.363032.
- [57] W.-Y. Chou, M.-H. Chang, H.-L. Cheng, Y.-C. Lee, C.-C. Chang, and H.-S. Sheu, 'New Pentacene Crystalline Phase Induced by Nanoimprinted Polyimide Gratings', *J. Phys. Chem. C*, vol. 116, no. 15, pp. 8619–8626, Apr. 2012, doi: 10.1021/jp300043j.
- [58] A. W. HORTON, 'The Mechanism of the Reactions of Hydrocarbons with Sulfur1', *J. Org. Chem.*, vol. 14, no. 5, pp. 761–770, 1949.
- [59] K. Takimiya, I. Osaka, T. Mori, and M. Nakano, 'Organic Semiconductors Based on [1]Benzothieno[3,2-b][1]benzothiophene Substructure', *Acc. Chem. Res.*, vol. 47, no. 5, pp. 1493–1502, May 2014, doi: 10.1021/ar400282g.
- [60] P. Xie, T. Liu, J. Sun, and J. Yang, 'Structures, Properties, and Device Applications for [1]Benzothieno[3,2-b]Benzothiophene Derivatives', *Adv. Funct. Mater.*, vol. 32, no. 21, p. 2200843, May 2022, doi: 10.1002/adfm.202200843.
- [61] H. Usta *et al.*, 'High Electron Mobility in [1]Benzothieno[3,2-b][1]benzothiophene-Based Field-Effect Transistors: Toward n-Type BTBTs', *Chem. Mater.*, vol. 31, no. 14, pp. 5254–5263, Jul. 2019, doi: 10.1021/acs.chemmater.9b01614.
- [62] H. Ebata *et al.*, 'Highly Soluble [1]Benzothieno[3,2-b]benzothiophene (BTBT) Derivatives for High-Performance, Solution-Processed Organic Field-Effect Transistors', *J. Am. Chem. Soc.*, vol. 129, no. 51, pp. 15732–15733, Dec. 2007, doi: 10.1021/ja074841i.
- [63] K. Takimiya, H. Ebata, K. Sakamoto, T. Izawa, T. Otsubo, and Y. Kunugi, '2,7-Diphenyl[1]benzothieno[3,2-b]benzothiophene, A New Organic Semiconductor for Air-Stable Organic Field-Effect Transistors with Mobilities up to 2.0 cm² V⁻¹ s⁻¹', *J. Am. Chem. Soc.*, vol. 128, no. 39, pp. 12604–12605, Oct. 2006, doi: 10.1021/ja064052l.
- [64] R. Ozdemir *et al.*, 'Engineering functionalized low LUMO [1] benzothieno [3, 2-b][1] benzothiophenes (BTBTs): unusual molecular and charge transport properties', *J. Mater. Chem. C*, vol. 8, no. 43, pp. 15253–15267, 2020.
- [65] T. Mori *et al.*, 'Consecutive thiophene-annulation approach to π -extended thienoacene-based organic semiconductors with [1] benzothieno [3, 2-b][1]

- benzothiophene (BTBT) substructure', *J. Am. Chem. Soc.*, vol. 135, no. 37, pp. 13900–13913, 2013.
- [66] R. Wawrzinek *et al.*, 'Mobility Evaluation of [1] Benzothieno [3, 2-b][1] benzothiophene Derivatives: Limitation and Impact on Charge Transport', *ACS Appl. Mater. Interfaces*, vol. 11, no. 3, pp. 3271–3279, 2018.
- [67] Q. Wei *et al.*, 'Theoretical Studies of Bipolar Transport in CnBTBT–FmTCNQ Donor–Acceptor Cocrystals', *J. Phys. Chem. Lett.*, vol. 11, no. 2, pp. 359–365, Jan. 2020, doi: 10.1021/acs.jpcclett.9b03439.
- [68] T. Izawa, E. Miyazaki, and K. Takimiya, 'Molecular Ordering of High-Performance Soluble Molecular Semiconductors and Re-evaluation of Their Field-Effect Transistor Characteristics', *Adv. Mater.*, vol. 20, no. 18, pp. 3388–3392, 2008, doi: <https://doi.org/10.1002/adma.200800799>.
- [69] H. Minemawari *et al.*, 'Enhanced layered-herringbone packing due to long alkyl chain substitution in solution-processable organic semiconductors', *Chem. Mater.*, vol. 29, no. 3, pp. 1245–1254, 2017.
- [70] S. Tsuzuki, K. Honda, T. Uchimaru, M. Mikami, and K. Tanabe, 'Origin of Attraction and Directionality of the π/π Interaction: Model Chemistry Calculations of Benzene Dimer Interaction', *J. Am. Chem. Soc.*, vol. 124, no. 1, pp. 104–112, Jan. 2002, doi: 10.1021/ja0105212.
- [71] D. E. Williams and Y. Xiao, 'Benzene, naphthalene and anthracene dimers and their relation to the observed crystal structures', *Acta Crystallogr. A*, vol. 49, no. 1, pp. 1–10, 1993.
- [72] H. Kobayashi *et al.*, 'Hopping and band mobilities of pentacene, rubrene, and 2, 7-dioctyl [1] benzothieno [3, 2-b][1] benzothiophene (C8-BTBT) from first principle calculations', *J. Chem. Phys.*, vol. 139, no. 1, 2013.
- [73] J. Xi, M. Long, L. Tang, D. Wang, and Z. Shuai, 'First-principles prediction of charge mobility in carbon and organic nanomaterials', *Nanoscale*, vol. 4, no. 15, pp. 4348–4369, 2012.
- [74] Y. Yuan *et al.*, 'Ultra-high mobility transparent organic thin film transistors grown by an off-centre spin-coating method', *Nat. Commun.*, vol. 5, no. 1, p. 3005, 2014.

- [75] H. Iino and J. Hanna, 'Liquid crystalline organic semiconductors for organic transistor applications', *Polym. J.*, vol. 49, no. 1, pp. 23–30, 2017.
- [76] A. Y. Amin, A. Khassanov, K. Reuter, T. Meyer-Friedrichsen, and M. Halik, 'Low-voltage organic field effect transistors with a 2-tridecyl [1] benzothieno [3, 2-b][1] benzothiophene semiconductor layer', *J. Am. Chem. Soc.*, vol. 134, no. 40, pp. 16548–16550, 2012.
- [77] T. Salzillo *et al.*, 'Enhancing Long-Term Device Stability Using Thin Film Blends of Small Molecule Semiconductors and Insulating Polymers to Trap Surface-Induced Polymorphs', *Adv. Funct. Mater.*, vol. 30, no. 52, p. 2006115, 2020.
- [78] Y. He *et al.*, 'High Performance OTFTs Fabricated Using a Calamitic Liquid Crystalline Material of 2-(4-Dodecyl phenyl)[1] benzothieno [3, 2-b][1] benzothiophene', *Adv. Electron. Mater.*, vol. 2, no. 9, p. 1600179, 2016.
- [79] A. N. Sokolov *et al.*, 'From computational discovery to experimental characterization of a high hole mobility organic crystal', *Nat. Commun.*, vol. 2, no. 1, p. 437, 2011.
- [80] Wen Shi, Z. M. Wong, T. Deng, G. Wu, and S. Yang, 'Unravelling the Molecular Origin of Organic Semiconductors with High-Performance Thermoelectric Response', *Adv. Funct. Mater.*, vol. 31, no. 9, p. 2007438, 2021.
- [81] L. Fijahi *et al.*, 'Charge transfer complexes of a benzothienobenzothiophene derivative and their implementation as active layer in solution-processed thin film organic field-effect transistors', *J Mater Chem C*, vol. 10, no. 18, pp. 7319–7328, 2022, doi: 10.1039/D2TC00655C.
- [82] H. Spreitzer *et al.*, 'Alkyl chain assisted thin film growth of 2,7-dioctyloxy-benzothienobenzothiophene', *J Mater Chem C*, vol. 7, no. 27, pp. 8477–8484, 2019, doi: 10.1039/C9TC01979K.
- [83] S. Yan *et al.*, 'Temperature-induced polymorphism of a benzothiophene derivative: reversibility and impact on the thin film morphology', *Phys Chem Chem Phys*, vol. 24, no. 39, pp. 24562–24569, 2022, doi: 10.1039/D2CP03467K.
- [84] C. Ruzié *et al.*, 'Design, synthesis, chemical stability, packing, cyclic voltammetry, ionisation potential, and charge transport of [1]benzothieno[3,2-b][1]benzothiophene derivatives', *J Mater Chem C*, vol. 4, no. 22, pp. 4863–4879, 2016, doi: 10.1039/C6TC01409G.

- [85]S. Hofer *et al.*, ‘Phase Transition toward a Thermodynamically Less Stable Phase: Cross-Nucleation due to Thin Film Growth of a Benzothieno-benzothiophene Derivative’, *J. Phys. Chem. C*, vol. 125, no. 51, pp. 28039–28047, Dec. 2021, doi: 10.1021/acs.jpcc.1c06610.
- [86]N. Bedoya-Martínez *et al.*, ‘DFT-Assisted Polymorph Identification from Lattice Raman Fingerprinting’, *J. Phys. Chem. Lett.*, vol. 8, no. 15, pp. 3690–3695, Aug. 2017, doi: 10.1021/acs.jpcllett.7b01634.
- [87]A. O. F. Jones *et al.*, ‘Substrate-Induced Phase of a [1]Benzothieno[3,2-b]benzothiophene Derivative and Phase Evolution by Aging and Solvent Vapor Annealing’, *ACS Appl. Mater. Interfaces*, vol. 7, no. 3, pp. 1868–1873, Jan. 2015, doi: 10.1021/am5075908.
- [88]H. Iino, T. Usui, and J. Hanna, ‘Liquid crystals for organic thin-film transistors’, *Nat. Commun.*, vol. 6, no. 1, p. 6828, Apr. 2015, doi: 10.1038/ncomms7828.
- [89]M. Kunii, H. Iino, and J. Hanna, ‘Bias-stress characterization of solution-processed organic field-effect transistor based on highly ordered liquid crystals’, *Appl. Phys. Lett.*, vol. 110, no. 24, 2017.
- [90]S. Hofer *et al.*, ‘Molecular disorder in crystalline thin films of an asymmetric BTBT derivative’, *Chem. Mater.*, vol. 33, no. 4, pp. 1455–1461, 2021.
- [91]T. Hamai, S. Arai, and T. Hasegawa, ‘Effects of tunneling-based access resistance in layered single-crystalline organic transistors’, *J. Mater. Res.*, vol. 33, no. 16, pp. 2350–2363, 2018.
- [92]Z. Lamport, H. Iqbal, S. Anand, M. Waldrip, and O. Jurchescu, ‘Tutorial: Organic field-effect transistors: Materials, structure and operation’, *J. Appl. Phys.*, vol. 124, p. 071101, Aug. 2018, doi: 10.1063/1.5042255.
- [93]W.-Y. Lee and J. Mei, ‘OFETs: BASIC CONCEPTS AND MATERIAL DESIGNS’, 2016.
- [94]X. Liu *et al.*, ‘MoS₂ Negative-Capacitance Field-Effect Transistors with Subthreshold Swing below the Physics Limit’, *Adv. Mater.*, vol. 30, no. 28, p. 1800932, 2018, doi: <https://doi.org/10.1002/adma.201800932>.

- [95]A. F. Paterson *et al.*, ‘Recent Progress in High-Mobility Organic Transistors: A Reality Check’, *Adv. Mater.*, vol. 30, no. 36, p. 1801079, Sep. 2018, doi: 10.1002/adma.201801079.
- [96]C. Liu, Y. Xu, Y. Li, W. Scheideler, and T. Minari, ‘Critical Impact of Gate Dielectric Interfaces on the Contact Resistance of High-Performance Organic Field-Effect Transistors’, *J. Phys. Chem. C*, vol. 117, no. 23, pp. 12337–12345, Jun. 2013, doi: 10.1021/jp4023844.
- [97]D. Natali and M. Caironi, ‘Charge Injection in Solution-Processed Organic Field-Effect Transistors: Physics, Models and Characterization Methods’, *Adv. Mater.*, vol. 24, no. 11, pp. 1357–1387, 2012, doi: <https://doi.org/10.1002/adma.201104206>.
- [98]C. Liu, Y. Xu, and Y.-Y. Noh, ‘Contact engineering in organic field-effect transistors’, *Mater. Today*, vol. 18, no. 2, pp. 79–96, Mar. 2015, doi: 10.1016/j.mattod.2014.08.037.
- [99]A. Babuji *et al.*, ‘Double Beneficial Role of Fluorinated Fullerene Dopants on Organic Thin-Film Transistors: Structural Stability and Improved Performance’, *ACS Appl. Mater. Interfaces*, vol. 12, no. 25, pp. 28416–28425, Jun. 2020, doi: 10.1021/acsami.0c06418.

3

MAIN METHODS AND TECHNIQUES

3.1 Substrates prepared and cleaning

During this thesis we primarily use P-type native Silicon substrates, unless specified otherwise. The cleaning process encompasses ultra-sonication in a solvent bath followed by UV-ozone cleaning. During the ultra-sonication cleaning stage, the substrates are cleaned three times: initially with ethanol, then with acetone, and finally with ethanol again for the last cleaning, with each session lasting approximately 10-15 minutes. After cleaning, the substrates are dried using a nitrogen gun. After that, they are treated with a UV-ozone cleaner for 10-15 minutes. This cleaning process effectively removes most organic impurities from the substrate surface, ensuring the level of cleanliness required for the experiments.

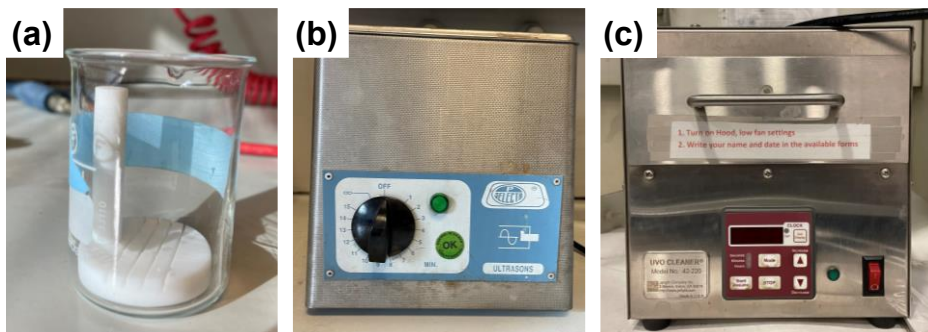


Figure 1: Equipment and instruments used in the substrate cleaning process: (a) sample cleaning rack and beaker; (b) ultra-sonication machine; (c) UV-ozone machine.

3.2 Organic Molecular Beam Deposition (OMBD)

Organic Molecular Beam Deposition (OMBD) is widely used for the fabrication of organic thin films by sublimation of the organic compound in high or ultra-high vacuum. It is also known as physical vapor deposition. It offers several advantages: firstly, it can be used to prepare films from organic materials that are insoluble or difficult to dissolve in solvents; secondly, fabricating films in a high-vacuum or ultra-high vacuum environment prevents contamination of the samples during the preparation process or from the solvent (it is solvent free), and thirdly, it allows for precise control over the thickness of the films and the growth rate.

Here, I will detail the components of OMBD and our experimental procedures and conditions, integrating the specific equipment used in our laboratory. The material powder is loaded into a crucible located within a Knudsen cell. The temperature of the crucible is controlled by adjusting the current from the power supply connected to the cell, allowing control over the evaporation rate of the material. During the evaporation process, a quartz crystal microbalance is used to monitor the thickness of the deposited

film. The sample holder is positioned at the focus of the evaporation cone and sits onto a heater that enables additional annealing of the substrate prior to film deposition or during the growth to provide different growth conditions. Both, the effusion cell and the sample holder are equipped with a shutter, facilitating the start, pause, or termination of the material growth process at any time.

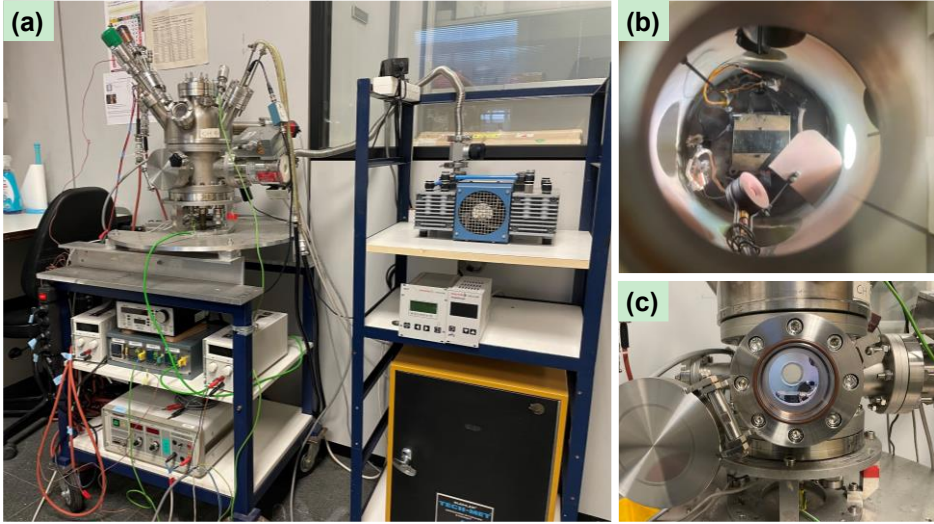


Figure 2: OMBD equipment in our lab. (a) The general view of whole equipment. (b) Photograph taken from the top window of the growth chamber, showing the sample holder, sample shutter, QM (close to the bottom of this picture) and one of our effusion cells. (c) View from the chamber door.

In our experiments, the substrate located on the sample holder is first pre-annealed once the pressure in the growth chamber reaches the required level ($\leq 10^{-6}$ mbar). The annealing temperature should be higher than 200 °C and maintained for at least ten minutes. The purpose of this step is to desorb water and contaminants from the substrate. Simultaneously, the sublimation cell is degassed at a temperature higher than 100 °C to remove moisture from the material and purify it. Before opening the sample shutter, the evaporation rate should be at a stable rate because the growth rate significantly affects

the film development, and stable, low-speed growth parameters are necessary to obtaining high-crystallinity films. Therefore, to ensure the quality of the films and the reproducibility of the samples, the evaporation rate is generally controlled at 2-3 Å/min in our experiments. The sublimation temperature for the growth of C8O-BTBT-OC8 is around 180 °C and for Ph-BTBT-10 is around 200 °C. The sample shutter also offers another advantage, allowing us to fabricate samples with varying thicknesses and compositions in a single preparation.

However, our experiments indicate a spatial gradient in the evaporation flux that causes the final coverage of the samples to varies when the samples are out of the center. Figure 3a shows a top-view scheme that illustrates the geometric relationship between three samples located in the sample holder, the effusion cell, and the quartz microbalance (QM). Sample B is the one located in the middle of the sample holder, with Sample A and Sample C positioned to the left and right of Sample B, respectively. Sample A is the farthest from the cell, while Sample C is the closest. We have verified that the shutter on the sample holder can cover all three samples when closed. Figure 3b displays AFM topography images obtained in different regions (top, middle, or bottom) of these three samples. In this experiment, the deposition material used is C8O-BTBT-OC8, and the nominal thickness is 60 Å, which is equivalent to two monolayers. After analysis of the morphology, we found that the film thickness in the middle region of sample B is approximately equivalent to two monolayers, consistent with the QM reading. For the middle of sample C the conclusion is that its actual thickness is about 1.76 monolayers, which is 88% of the nominal thickness. For the middle part of the sample A, the real thickness is around 29.5 Å, which is half of the nominal thickness. In our experiments

we tried to put the samples as close as possible to the center.

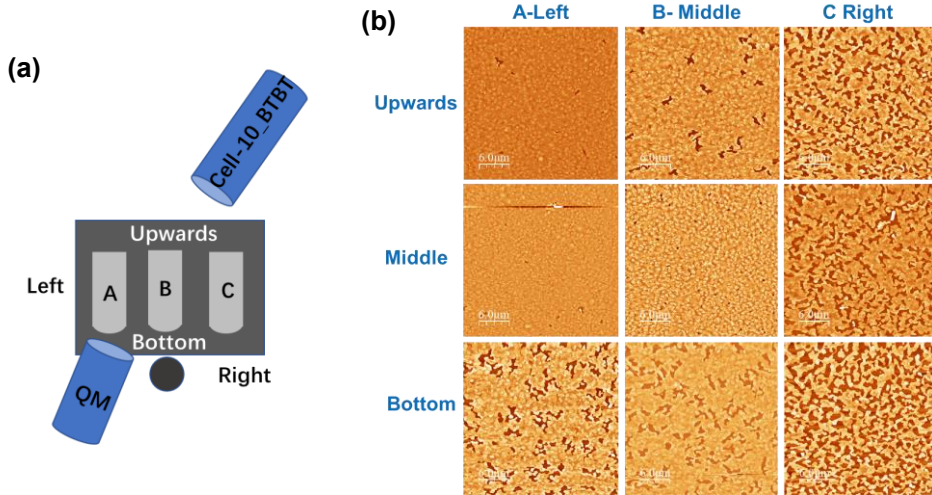


Figure 3: (a) the scheme shows the geometric relationship between the sample, the QM and effusion cell, (b) AFM topography images from different parts of each sample. The size of the sample is around 1cm x 2cm and the distance between adjacent samples is approximately 0.8 cm. Therefore, the distance from the left side of sample A to the right side of sample C is approximately 5 cm.

Moreover, in some experiments we used a transmission electron microscopy (TEM) grid as a shadow mask to have regions with uncovered substrate that can be used as reference (the optical microscope images are shown in figure 4a). This stainless steel grid features a central circular pattern with a diameter of 40 microns, a scale that conveniently allows us to study the surface characteristics of different regions by AFM (the topography and phase images are shown in Figure 4b and 4c).

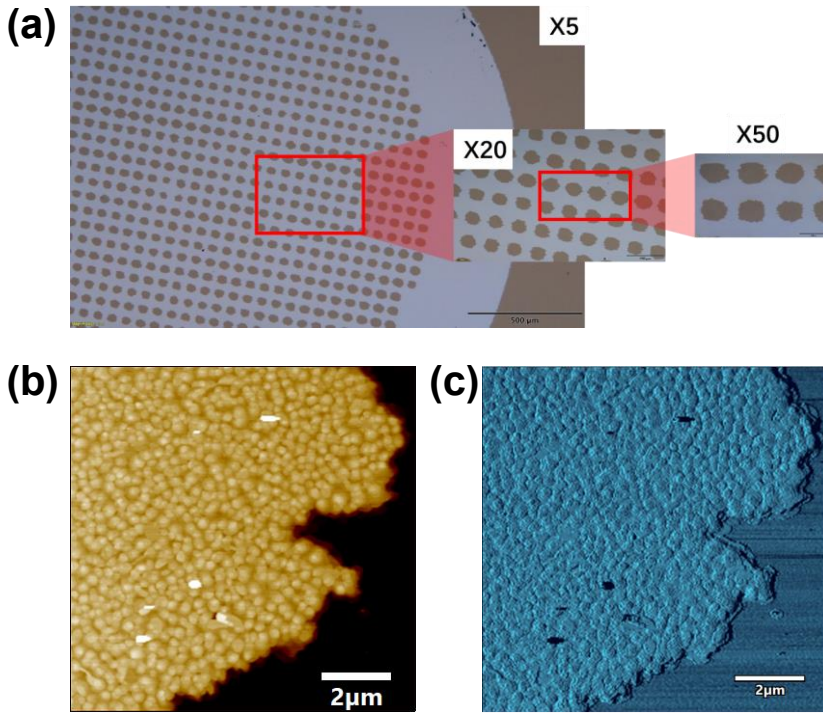


Figure 4: (a) Optical microscope images of a TEM grid mask at different magnifications, (b) and (c) are the AFM topography and phase images of one of the patterned organic films grown with the shadow mask, respectively. The uncover substrate is visible on the right part of the images.

3.3 Atomic force microscopy

Atomic Force Microscopy (AFM)[1] has been widely applied in recent years to the study of a broad range of materials, with applications across various fields such as batteries, biology, solar cells, and electronic devices.[2] Generally, AFM is used to obtain topographic images of sample surfaces, primarily through working modes such as contact and dynamic modes.[2],[3],[4] Beyond these traditional modes, researchers have been tirelessly developing novel modes. These advanced measuring modes enable users to capture information about the material that extends beyond topography and local force

measurements. Examples of such measurements include Young's modulus,[5] adhesion,[6] piezo response,[7] electrical conductivity,[8] surface potential,[9] and electrochemistry.[10],[11],[12]

In this chapter, based on the application in our experiments, we will mainly focus on the contact and dynamic working mode, Friction force microscopy and Kelvin probe force microscopy.

3.3.1 AFM setup and basic operation

Atomic Force Microscopy (AFM) is a member of the Scanning Probe Microscopy (SPM) family, fundamentally operating by measuring material surface properties with a physical nanometric-sized probe. The feedback signal from the probe results from specific interactions between the probe and the sample.

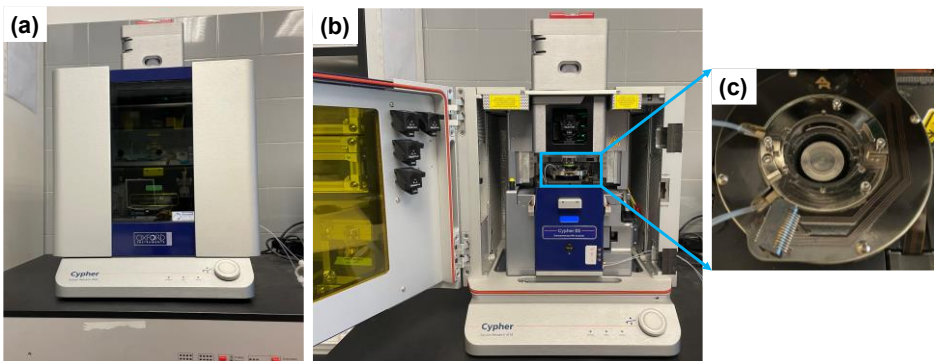


Figure 5. The AFM setup in our lab. (a) The global overview of Cypher microscope, (b) The view when enclosed door opened, the scanner is the blue subject, (c) The scanning stage.

The invention of Atomic Force Microscopy by Binnig, Quate and Gerber dates back to 1986 at Stanford University. It consists of a cantilever approached to the surface that

bends or twists due to the interaction forces between the tip and the sample surface, which include Van der Waals forces,[13] short-range forces,[13] friction forces,[14] and electrostatic forces.[15] These interaction forces are typically in the order of nano-newtons or even less.

In AFM, a photodetector detects the deflection of a laser focused on the back of the cantilever.[16] As illustrated below in the Figure 6, the photodetector is composed of four quadrants, a design that allows for the quantification of bending along the normal direction and torsion around the cantilever's axis. Vertical shifts in the laser relative to the quadrant's origin result from cantilever bending, while horizontal shifts are due to torsion. Ultimately, information about the normal and lateral forces is transmitted in volts to two separate channels, representing the normal force and the lateral force. There are excellent books and reviews with technical details, for example the book B. Bushan and O. Marti.[17],[18]

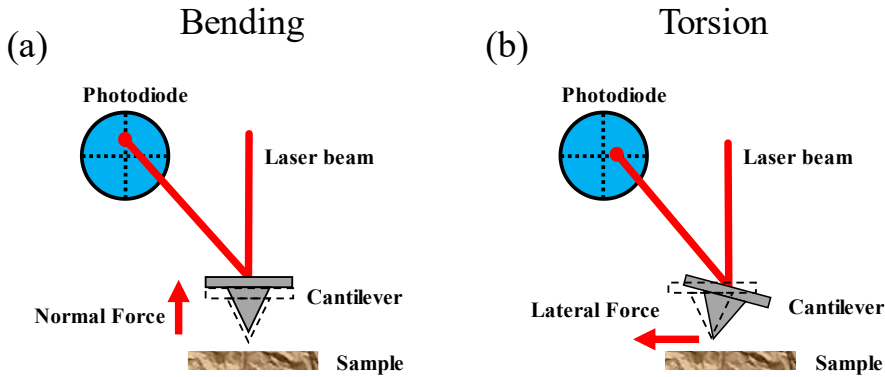


Figure 6. Schematic view of the laser deflection detection method commonly used in an AFM setup.

It is clear that the characteristics of the tip and cantilever, such as shape, size, material, and stiffness, significantly influence the measurements. Therefore, selecting an

appropriate probe based on the specific characteristics of the sample is crucial during testing.

3.3.2 AFM measurement mode

The two primary working modes of AFM are contact and dynamic modes. In contact mode, the tip directly contacts the sample, causing the tip-sample interaction to result in vertical or lateral deflection of the cantilever. In dynamic mode, the cantilever is oscillated at a certain frequency (generally its resonance frequency) close to the surface. The interaction between the tip and the surfaces causes changes relative to the initial tip oscillation, such as changes in phase, frequency, and amplitude. We will discuss these two modes in more detail next.

3.3.2.1 Contact mode

In this working mode, the tip maintains direct contact with the sample surface, and the cantilever deflection caused by the repulsive tip-sample force is monitored. During scanning, the piezoelectric element's Z movement is adjusted through a feedback loop to keep the tip deflection at a constant value. Thus, the Z movement values required to maintain the normal deflection of the cantilever at each point of the scanning area form the topographic image. Understanding the tip-sample interaction force during the tip approach process is also crucial. This not only helps the experimenter quantitatively understand the force between the tip and the sample but also aids in finding the optimal test set point.[19]

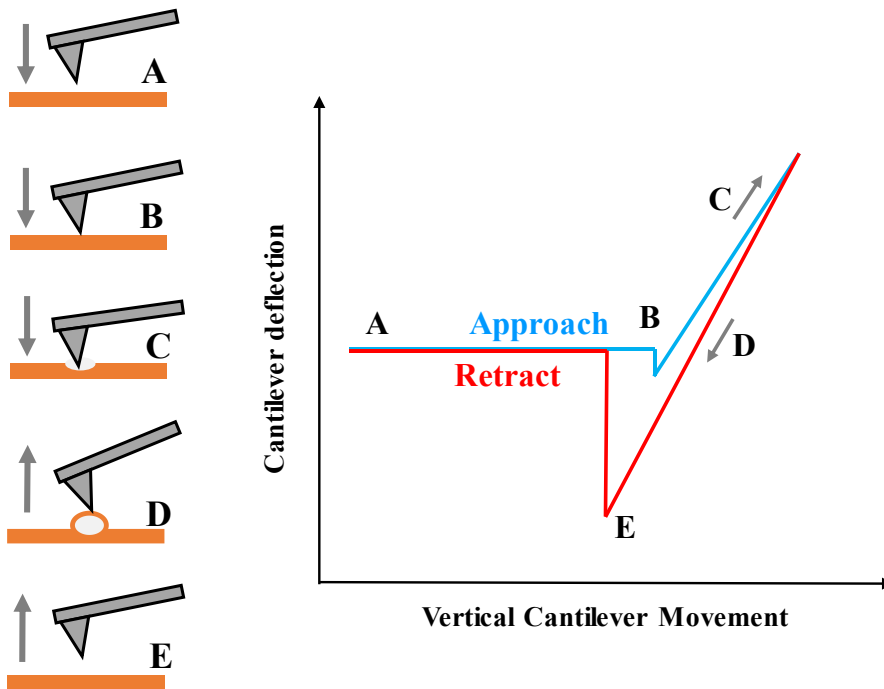


Figure 7: Cantilever deflection recorded in a force-distance curve, representing the cantilever deflection vs. Z piezo movement during one approach and withdraw cycle. The point of Snap-On is marked as B, and the point of snap-off is marked as E.

Let's examine the accompanying Figure 7 to detail how the tip deflection varies with the Z movement of the piezo during the approach of the tip towards the sample surface (force-distance curve). At position A, there is no change in the cantilever deflection. As the tip gradually approaches the sample the attractive interactions (such as Van der Waals forces) cause a change in the cantilever deflection (the tip bends towards the sample). As the tip continues to approach the surface, the sum of the attractive forces exceeds the restoring force from the cantilever spring, causing the tip to suddenly jump into contact with the surface, a position also known as the snap-in point (at position B). Due to repulsive short-range forces (C), the cantilever deflects away from the surface linearly with the scanner movement (blue curve in the Figure 7). However, when we try to retract

the tip (red curve in the Figure 7), the tip remains attached to the surface due to the adhesion of the tip to the surface (from D to E in the red curve). To compensate this force, the piezo needs to be further retracted until the tip snaps free (point E). Therefore, the approach (blue) and retract (red) curves will not be exactly the same when measured in ambient conditions (hysteresis) due to capillary adhesion forces caused by water adhering to the sample surface, resulting in bending of the cantilever from position C to E. In the plot the Y-axis represents the photodiode response V_{A-B} , and the X-axis represents the vertical movement of the piezo (Z). To convert the V_{A-B} signal into force, the deflection in volts must be translated to nanometers using the slope of the approach force-distance curve. The sensitivity factor, S_z [nm/V], is the inverse of the slope. Subsequently, by introducing the cantilever force constant, k_z [N/m], we can obtain the applied load (in nN): $F = K_z S_z \Delta Z$.

Based on the defined set point, we can identify two regimes: (a) the repulsive regime, when the cantilever has a positive deflection (from B to C), and (b) the attractive regime with negative deflection (from D to E).

3.3.2.2 Dynamic mode

In dynamic mode, the feedback loop is based on monitoring the behavior of the vibrating cantilever as it approaches the sample surface. As it comes closer to the sample, the tip-sample interactions induce variations in the cantilever's frequency, amplitude, and phase relative to the reference oscillation. In principle, any of these variations in physical magnitudes can serve as a feedback parameter to track the properties of the sample surface,[3],[21],[22] which enables multiple operational modes. Among the various

working modes, the main ones are Amplitude Modulation (AM-AFM) and Frequency Modulation (FM-AFM), where the feedback parameters are the amplitude and the frequency shift of the cantilever, respectively.[3],[21],[22]

In Amplitude Modulation (AM-AFM), the cantilever is excited at a fixed frequency, which could be at the resonance frequency or excited at higher eigenmode, such as the 2nd or 3rd. The oscillation amplitude of the cantilever is monitored. As the tip approaches the sample surface, the frequency shifts by the action of the conservative forces and the oscillation amplitude decreases due to the dissipative interaction between the tip and the sample (see Figure 8a and 8b).[22],[23] During scanning, the tip-sample position is adjusted via the topographic feedback to maintain a constant amplitude. The phase map simultaneously acquired, which is very sensitive to compositional differences on the surface.

The figure 9a and 9b illustrates how the amplitude and phase of the sensor change as the distance between the tip and the sample varies, enabling control of the measurements in either the attractive or repulsive region. Far from the sample (Z-position > 60 nm), the tip amplitude is 60 nm (free amplitude) and the phase is nearly 90°, indicating that the cantilever is being driven at resonance. As the tip approaches the sample (Z-position < 60 nm in the figure), the tip phase begins to increase due to the attractive interactions. However, as the tip gets closer to the sample, a repulsive force also comes into play and at a certain distance (Z-position close to 40 nm), when the repulsive force outweighs the attractive one, the phase shifts below 90°. In our measurements, we mostly operate in the attractive regime.

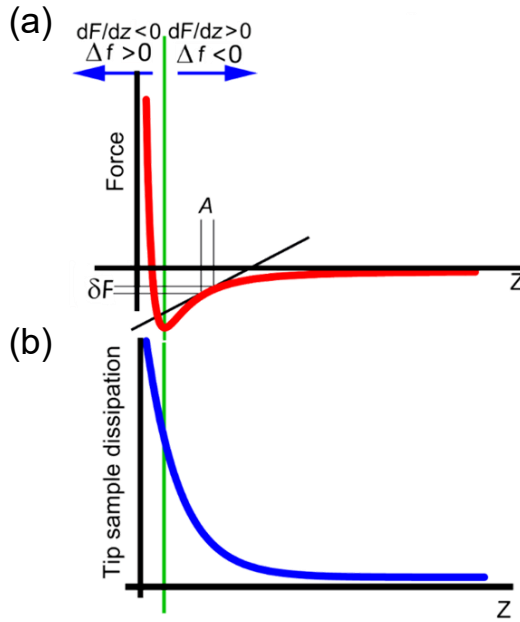


Figure 8: (a) Conservative force versus distance interaction between an AFM tip and a surface; (b) Energy dissipation of the tip as it approaches the sample;[22]

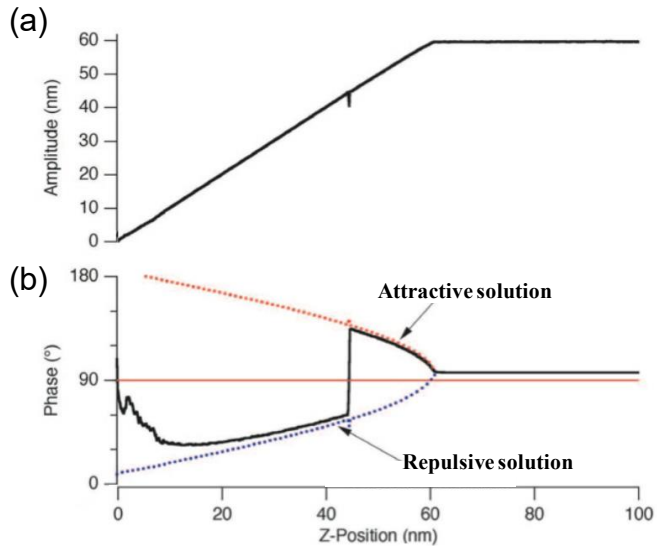


Figure 9: (a) Cantilever amplitude and (b) phase as a function of tip-sample distance.[24]

Commonly, topographic images provide accurate and real information about the sample surface. However, in some cases, if the chemical composition or physical properties vary within the scanning area, the topographic results may be inaccurate.[23]

A common issue can be an incorrect height measurement. Figure 10 presents the topography of C8O-BTBT-OC8 films deposited on a P-type silicon dioxide substrate, obtained by AFM in contact mode (Figure 10a) and dynamic mode (Figure 10b). In this sample we see several terraces in the organic film surrounded by uncovered substrate. The expected single-layer height is 3.1 nm (see chapter 2.2.2). In the topography obtained via contact mode, the measured height of all the layers is about 3.1-3.2 nm, closely matching the reported layer height. However, in the topography acquired through dynamic mode, while the height of the fourth layer is also 3.2 nm, the height of the first layer is 2.6 nm, which is lower than the actual layer height. This discrepancy arises from differences in the physical properties of the substrate and the OSC film. Therefore, in our experiments, height measurements are consistently cross-checked using also contact mode for accuracy.

In Frequency Modulation AFM (FM-AFM), changes in the cantilever's resonant frequency ($\Delta\omega$) are monitored while scanning. The feedback mechanism maintains a constant frequency shift by adjusting the relative tip-sample position and constructs a constant $\Delta\omega$ map by recording the relative piezo displacement. FM-AFM is not detailed here because it was not used in the experiments described in this thesis.

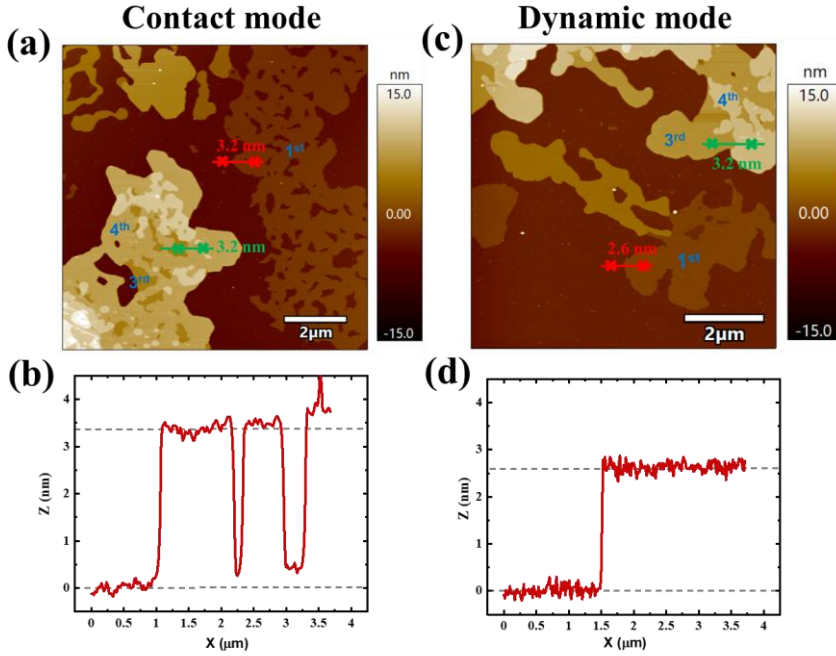


Figure 10. The topographies and height profile of the same sample obtained by contact mode (a, b) and dynamic mode (c, d).

3.3.3 AFM advanced operation modes

As mentioned earlier, AFM not only provides topographical information about the sample surface, but it is also sensitive to various physical and chemical interaction forces between the tip and the sample. This sensitivity enables the development of numerous specialized operation modes. The modes employed in this thesis will be detailed in the following sections.

3.3.3.1 Friction force microscopy

In Friction Force Microscopy (FFM), we measure the frictional forces along the

scanning path, which have an opposite force direction relative to the tip-sample motion.[14],[26] The friction generated by the tip's movement causes a torsion of the cantilever, which is detected by the lateral displacement of the laser spot in the four-quadrant photodiode as described before.[14],[27],[28] The lateral force image is related to dissipation and therefore is very sensitive to differences in the chemical composition, crystallinity, or orientation of the different domains of the sample with heterogeneous composition.[27],[28],[14],[28],[29],[25] In the work presented in this thesis, FFM was used for qualitative assessment or comparison between areas in the same sample. Therefore unlike other studies,[30] we did not determine the torsion spring constant of the cantilever and the sensitivity factor for the lateral force. That is, the signal is given in volts. In our experiments, each line was scanned twice (trace and retrace) to produce two lateral force images with opposite directions, named as forward and backward. In the forward scanning image, a higher lateral force indicates higher friction, whereas in the backward scanning image, the high-friction areas appear with a darker color. To avoid confusion, we consistently show the forward scanning image of the lateral force. The friction is calculated from $\frac{1}{2}(LF_{forward} - LF_{backward})$.

3.3.3.2 Kelvin probe force microscopy

The work function (Φ) is a fundamental property of solid materials, defined as the amount of energy required to extract an electron from the Fermi level (E_F) and place it at rest in free space above the vacuum level (E_{vac}). The macroscopic Kelvin probe method directly measures the work function of a material. This method is based on the principle of a parallel-plate capacitor formed between the sample and an oscillating

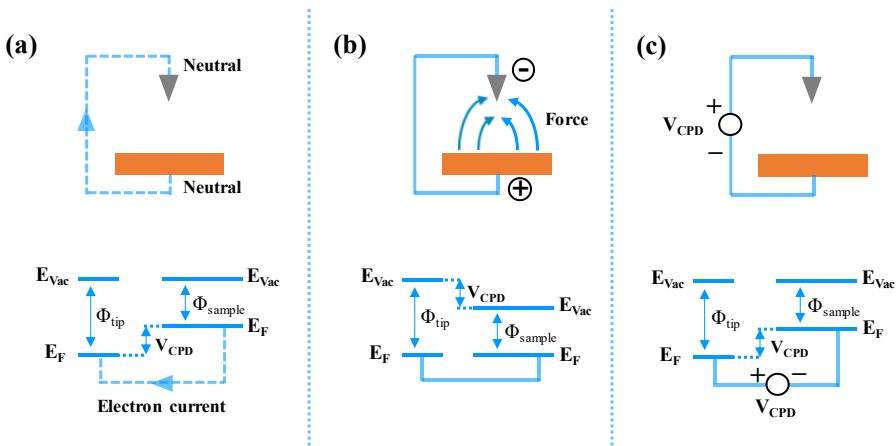
metallic probe.[32],[33],[34],[35],[36] It was initially developed by Lord Kelvin and later refined by William Zisman several decades later.[36],[37]

The KPFM measures the *contact potential difference* (CPD) between the AFM tip and the sample surface. The CPD (V_{CPD}) between the tip and sample is described as:

$$V_{CPD} = \frac{\phi_{tip} - \phi_{sample}}{-e} \quad (1)$$

Where ϕ_{tip} and ϕ_{sample} are the work functions of the sample and tip, e is the electronic charge.

Figure 11 illustrates how the energy levels of the tip and sample aligned, which are electrically connected but have different work functions. Electrons flow from the material with the lower work function to the one with the higher work function until their Fermi levels align. This electronic equilibrium creates a contact potential difference and electrostatic force between the tip and the sample. To counteract the electrostatic force, an additional bias voltage, known as the V_{CPD} (Voltaic Contact Potential Difference), is applied between the probe and the sample.



Figures 11: Definition and basic measurement setup of contact potential difference (CPD).

On the tip it is applied an AC voltage (V_{AC}) and DC voltage (V_{DC}). V_{AC} is used to generate an oscillatory electrostatic force between tip and sample that will help us to measure and nullify the electrostatic interaction by means of a lock-in. V_{DC} is used to nullify the oscillating electrical force and thus used to obtain the CPD in each pixel.

The electrostatic force (F_{es}) between tip and sample can be given by:

$$F_{es}(Z) = -\frac{1}{2}\Delta V^2 \frac{dC(z)}{dz} \quad (2)$$

And ΔV is the potential difference, consisting in V_{CPD} and the V_{DC} applied on the tip, it is:

$$\Delta V = V_{tip} - V_{CPD} = (V_{DC} + V_{CPD}) + V_{AC} \sin(\omega t) \quad (3)$$

Substituting Eq. (3) in Eq. (2) we get:

$$F_{es}(z, t) = -\frac{1}{2} \frac{\partial C(z)}{\partial z} [(V_{DC} + V_{CPD}) + V_{AC} \sin(\omega t)]^2 \quad (4)$$

This equation can be separated into three parts:

$$F_{DC} = -\frac{1}{2} \frac{\partial C(z)}{\partial z} [(V_{DC} + V_{CPD})^2 + \frac{1}{2} V_{AC}^2] \quad (5)$$

$$F_{\omega} = -\frac{\partial C(z)}{\partial z} (V_{DC} + V_{CPD}) V_{AC} \sin(\omega t) \quad (6)$$

$$F_{2\omega} = \frac{1}{4} \frac{\partial C(z)}{\partial z} V_{AC}^2 \cos(2\omega t) \quad (7)$$

F_{DC} results in a static deflection of the AFM tip, F_{ω} is used to measure the V_{CPD} , and $F_{2\omega}$ is used to measure the capacitance between the tip and sample surface. In KPFM there is an extra lock-in amplifier employed to measure the F_{ω} that is nullified by the

feedback of the Kelvin regulator. By this way, the V_{CPD} value in each point is acquired, form the map of surface potential of the whole sample surface. The obtained voltage map is also called surface potential (SP) map. In our AFM, with V_{DC} applied to the tip, a more positive value of the SP in one area respect to another area can be interpreted as a lower local work function.

In AM-KPFM, the electrostatic force F_w is measured directly from the amplitude of the cantilever oscillation at ω induced by the V_{AC} . The important parameters are the choice of ω for the electrostatic signal and the magnitude of V_{AC} .

In our experiments, we utilized a KPFM mode provided by Oxford Instruments, known as Nap mode. In Figure 12 the scheme illustrates how the NAP mode operates. It is conducted in two separate passes: the first is the surface pass (trace) indicated by a red dashed line in Figure 12, during which the AFM operates in the standard AM-dynamic mode to acquire the topographical map. The second is the Nap pass (retrace), indicated by the blue dashed line shown in Figure 12, during which there the mechanical oscillation is switched off and the standard Z feedback loop is turned off also, the tip can be approached towards the sample with a delta height. Instead, the tip is driven electrically with an AC bias at the same frequency (first eigenmode), being F_w is detected and nullified. In the Nap pass, in addition to the AC voltage, different delta height values also affect the accuracy of the Surface Potential (SP) information obtained. For delta height, the reference height is the center point of the cantilever oscillations. In our experiments, we normally set it at -10 nm, which indicates that the tip moves closer to sample surface by 10 nm during the second pass. This setting allows for more accurate SP measurements without the risk of the tip being too close to the sample and potentially

striking the surface.

In our experiment, normally we set the target amplitude at 1V and the sensor we used most are NSC35/Pt, which has 30nm thickness Pt coating on the tip.

1. Topography

2. Kpfm

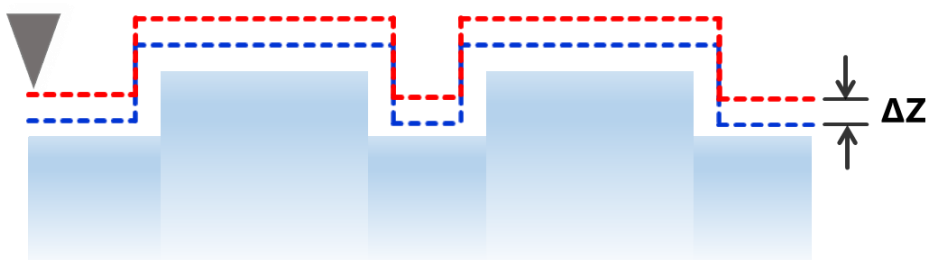


Figure 12. The two passes in NAP mode.

3.4 X-ray Diffraction

The structural information of the organic film is studied by X-ray diffraction. The wavelengths of electromagnetic waves for X-rays range from 0.1 to 100 Å. This wavelength(λ) range aligns well with the typical inter-atomic and inter-molecular distances found in solids, making X-rays highly effective for examining condensed matter at the atomic scale. X-ray waves exhibit positive interference after being scattered by the crystal planes when the incident wavelength satisfies Bragg's law:

$$n\lambda = 2d \sin \theta \quad (8)$$

In this relation, θ is the angle of the incident wave (respect to the crystal plane), d is the inter-planar distance of the sample, and n is an integer.

The scattering vector q is defined as $q=k_f-k_i$, and another expression of the Bragg's law is:

$$|q| = 2|k_i| \sin \theta = \frac{4\pi}{\lambda} \sin \theta \quad (9)$$

This formula's physical meaning is that constructive interference occurs if the incident (k_i) and scattered (k_f) wave vectors coincide with the sample's reciprocal lattice vector.[37] The scattering vector is the fundamental variable used to present the results of a scattering experiment independent from the x-ray wavelength λ used in the experiment.

Another fundamental property is that there is a critical angle at which total reflection occurs that allows measuring surfaces with enhanced sensitivity. By varying the angle of incidence, the penetration into the bulk can be controlled, which gives the means for performing a depth-dependent characterization. More detailed explanations about this topic can be found in the literature. [38],[39]

To obtain the structural characteristics of the material, we primarily focus on the molecular arrangement along two directions of the reciprocal space: q_z (perpendicular to the sample surface) and q_{xy} (along the sample surface). We acquire structural information in these directions through different tests: Specular X-ray diffraction (XRD) and grazing incidence X-ray diffraction (GIXD). It is also found in the literature as grazing incidence wide angle X-ray scattering GIWAXS. Using specular XRD, we can probe the component of the scattering vector perpendicular to the sample surface (q_z), also called out-of-plane (OOP) scan. This allows us to obtain information such as film thickness, surface roughness, and lattice structure along the q_z direction in reciprocal

space. For detailed information, refer to the literature.[41],[42] Using GIXD, we can probe the component of the scattering vector along the sample surface (q_{xy}). For detailed information, refer to.[42]

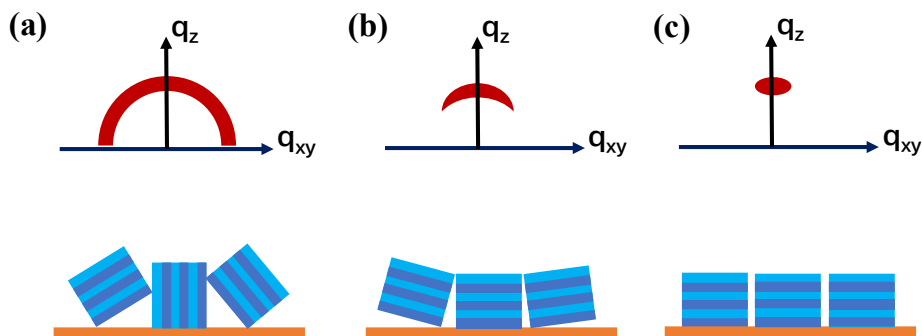


Figure 13. (a) Randomly oriented (similar to powder) arrangements of crystallites, with no preference for a specific crystallographic orientation with respect to the substrate normal produce rings in the diffraction patterns. (b) Textured or oriented films with a distribution of crystallite orientations produce arcs of diffracted intensity. (c) Highly oriented films produce spots or ellipses.

By analyzing the diffraction pattern shapes, we can infer and hypothesize the packing structure and degree of crystallinity of the molecules relative to the substrate surface. As shown in the Figure 13c, when the molecular arrangement in polycrystalline films is highly ordered with the crystalline planes parallel to the surface (textured film), the diffraction pattern appears as spots (Bragg peaks) along the q_z direction. If there is misalignment in the orientation of the crystallites on the surface, the diffracted intensity appears as arcs. A complete random orientation (i.e. powder) would result in powder diffraction rings. [43]

The results we show in chapter 4, 5 and 6 are acquired from the BL11-NCD-SWEET beamline of the ALBA Synchrotron (Spain) using a photon energy of 12.4 keV. Different incident angles were used, ranging between 0.091° and 0.151° , ensuring measurements

with surface sensitivity or full thin film penetration while minimizing the substrate contribution. A large-area 2D Rayonix LX 255-HS detector was used, which consists of a pixel array of 2880×960 (V * H) with a pixel size of $88.54 \times 88.54 \mu\text{m}^2$ for the binning employed. The scattering vector (q) was calibrated using Cr_2O_3 as a calibration standard and pyFAI python library is used for the conversion from pixels to reciprocal space .[44]

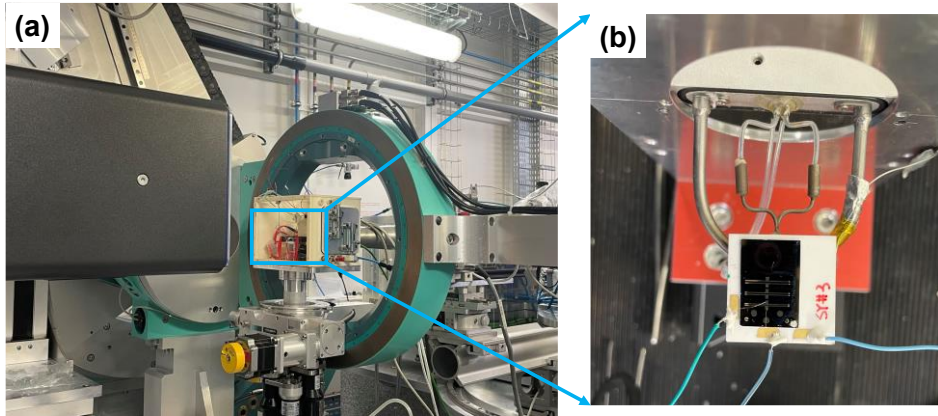


Figure 14: The equipment in ID28 at ESRF; (a) detector and sample stage; (b) The Linkam heating and cooling stage.

3.5 Ultraviolet Photoemission Spectroscopy (UPS)

For an introduction to the principles and analysis of UPS, please refer to the literature.[43], [45]. Here, we will primarily describe the specifics and setup of our experiment.

The UPS tests were conducted at the photoemission spectroscopy facility located at the Institut Catala de Nanociencia i Nanotecnologia (ICN2). This facility comprises three UHV chambers, designated for load lock, preparation, and analysis. It allows us to install our own Knudsen cell for sample preparation and to perform in-situ experiments. The

analysis system, which maintains a base pressure of 5×10^{-10} mbar, is outfitted with a SPECS Phoibos 150 hemispherical energy analyzer. UPS measurements were conducted using a monochromatic HeI UV source at 21.22 eV. The energy resolution, determined by the full width at half maximum (FWHM) of the Ag 3d_{5/2} peak from a sputtered silver foil, was recorded at 0.11 eV. To determine the work function of the samples from the secondary electron cutoff (SECO), spectra were collected with the samples biased at -10 V. Additionally, an Au (111) single crystal served as the reference for establishing the Fermi energy.

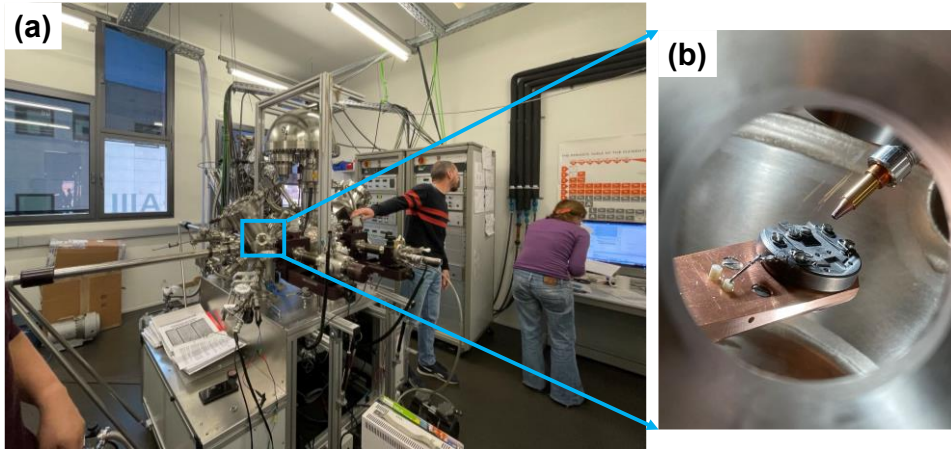


Figure 15: (a) The Global overview of the XPS-UPS system at ICN2. (b) our sample in the analysis chamber.

3.6 Fabrication and Characterization of OFETs

In this section, we discuss the preparation methods and characterization techniques used for OFETs in this experiment. Detailed information on the structure, analysis, and data

processing methods of OFETs can be found in Chapter 2 and the relevant literature.[47],[48],[49],[50], [51],[52],[53],[54] Here, we primarily focus on the device fabrication process and characterization methods used in this study.

In this thesis, we use OFETs to study the relationship between the packing structure of C8O-BTBT-OC8 and device efficiency. In our experiments, we employ a top contact, bottom gate device structure. A doped silicon piece with a 200 nm thick oxide layer serves both as the substrate for the device and as a dense dielectric layer. First, clean the silicon substrates according to the method described in Chapter 2. Then, place the substrates in the growth chamber to deposit the desired C8O-BTBT-OC8 thin film. After completing the film deposition, transfer the substrates with the organic thin film to the BOC Thermal Evaporator in the cleanroom. Using a shadow mask, deposit 50 nm of Au as the source and drain contacts.

OFETs were measured during a synchrotron experiment in December 2023 in the beamline BM28 (XMaS) of the ESRF using a Keithley 2612B.

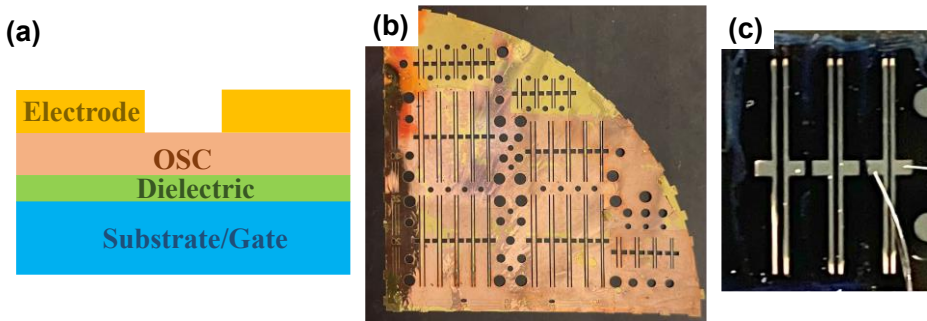


Figure 16: (a) The schema of device structure we used in this thesis, (b) The shadow mask, (c) The device photo.

Reference

- [1] G. Binnig, C. F. Quate, and C. Gerber, ‘Atomic force microscope’, *Phys. Rev. Lett.*, vol. 56, no. 9, p. 930, 1986.
- [2] D. Sarid, ‘Scanning Force Microscopy: With Applications To Electric, Magnetic, And Atomic Forces’, 1991. [Online]. Available: <https://api.semanticscholar.org/CorpusID:97505518>
- [3] B. Bhushan, *Springer handbook of nanotechnology*. Springer, 2017.
- [4] E. Meyer, H. J. Hug, and R. Bennewitz, *Scanning probe microscopy*, vol. 4. Springer, 2003.
- [5] O. H. Olubowale *et al.*, “‘May the Force Be with You!’ Force–Volume Mapping with Atomic Force Microscopy’, *ACS Omega*, vol. 6, no. 40, pp. 25860–25875, 2021, doi: 10.1021/acsomega.1c03829.
- [6] O. D. S. Ferreira, E. Gelinck, D. de Graaf, and H. Fischer, ‘Adhesion experiments using an AFM—Parameters of influence’, *Appl. Surf. Sci.*, vol. 257, no. 1, pp. 48–55, 2010, doi: <https://doi.org/10.1016/j.apsusc.2010.06.031>.
- [7] A. Gruverman, M. Alexe, and D. Meier, ‘Piezoresponse force microscopy and nanoferroic phenomena’, *Nat. Commun.*, vol. 10, no. 1, p. 1661, Apr. 2019, doi: 10.1038/s41467-019-09650-8.
- [8] G. A. MacDonald, P. A. Veneman, D. Placencia, and N. R. Armstrong, ‘Electrical Property Heterogeneity at Transparent Conductive Oxide/Organic Semiconductor Interfaces: Mapping Contact Ohmicity Using Conducting-Tip Atomic Force Microscopy’, *ACS Nano*, vol. 6, no. 11, pp. 9623–9636, 2012, doi: 10.1021/nn303043y.
- [9] X. Shi, W. Qing, T. Marhaba, and W. Zhang, ‘Atomic force microscopy - Scanning electrochemical microscopy (AFM-SECM) for nanoscale topographical and

- electrochemical characterization: Principles, applications and perspectives', *Electrochimica Acta*, vol. 332, p. 135472, 2020, doi: <https://doi.org/10.1016/j.electacta.2019.135472>.
- [10] J. Loos, 'The art of SPM: Scanning probe microscopy in materials science', *Adv. Mater.*, vol. 17, no. 15, pp. 1821–1833, 2005.
- [11] P. Samorì, *Scanning probe microscopies beyond imaging: manipulation of molecules and nanostructures*. John Wiley & Sons, 2006.
- [12] T. Glatzel, M. C. Lux-Steiner, E. Strassburg, A. Boag, and Y. Rosenwaks, 'Principles of Kelvin probe force microscopy', *Scanning Probe Microsc. Electr. Electromechanical Phenom. Nanoscale*, pp. 113–131, 2007.
- [13] J. N. Israelachvili, *Intermolecular and surface forces*. Academic press, 2011.
- [14] C. Robert W and S. M., 'Scratching the Surface: Fundamental Investigations of Tribology with Atomic Force Microscopy.', *Chem. Rev.*, vol. 97, no. 4, pp. 1163–1194, 1997, doi: <https://doi.org/10.1021/cr960068q>.
- [15] H.-J. Butt, 'Electrostatic interaction in atomic force microscopy', *Biophys. J.*, vol. 60, no. 4, pp. 777–785, 1991, doi: [https://doi.org/10.1016/S0006-3495\(91\)82112-9](https://doi.org/10.1016/S0006-3495(91)82112-9).
- [16] S. Alexander *et al.*, 'An atomic-resolution atomic-force microscope implemented using an optical lever', *J. Appl. Phys.*, vol. 65, no. 1, pp. 164–167, Jan. 1989, doi: 10.1063/1.342563.
- [17] B. Bhushan and O. Marti, 'Scanning probe microscopy–principle of operation, instrumentation, and probes', *Springer Handb. Nanotechnol.*, pp. 573–617, 2010.
- [18] D. Schryvers, 'Scanning Force Microscopy', *Mater. Res. Bull.*, vol. 6, no. 31, p. 759, 1996.
- [19] A. L. Weisenhorn, P. K. Hansma, T. R. Albrecht, and C. F. Quate, 'Forces in atomic

- force microscopy in air and water', *Appl. Phys. Lett.*, vol. 54, no. 26, pp. 2651–2653, Jun. 1989, doi: 10.1063/1.101024.
- [20] R. García, 'Dynamic atomic force microscopy methods', *Surf. Sci. Rep.*, vol. 47, no. 6–8, pp. 197–301, Sep. 2002, doi: 10.1016/S0167-5729(02)00077-8.
- [21] R. García, *Amplitude modulation atomic force microscopy*. John Wiley & Sons, 2011.
- [22] M. Jaafar, D. Martínez-Martín, M. Cuenca, J. Melcher, A. Raman, and J. Gómez-Herrero, 'Drive-amplitude-modulation atomic force microscopy: From vacuum to liquids', *Beilstein J. Nanotechnol.*, vol. 3, pp. 336–344, Apr. 2012, doi: 10.3762/bjnano.3.38.
- [23] E. Palacios-Lidón, C. Munuera, C. Ocal, and J. Colchero, 'Contrast inversion in non-contact Dynamic Scanning Force Microscopy: What is high and what is low?', *Ultramicroscopy*, vol. 110, no. 7, pp. 789–800, Jun. 2010, doi: 10.1016/j.ultramic.2010.01.015.
- [24] Asylum Research, *Application Guide*, Version 18. Asylum Research an Oxford Instruments company, 2021.
- [25] R. Bennewitz, 'Friction Force Microscopy', in *Fundamentals of Friction and Wear*, E. Gnecco and E. Meyer, Eds., Berlin, Heidelberg: Springer Berlin Heidelberg, 2007, pp. 1–14. doi: 10.1007/978-3-540-36807-6_1.
- [26] J. Y. Park and M. Salmeron, 'Fundamental Aspects of Energy Dissipation in Friction', *Chem. Rev.*, vol. 114, no. 1, pp. 677–711, Jan. 2014, doi: 10.1021/cr200431y.
- [27] E. Gnecco and E. Meyer, Eds., *Fundamentals of Friction and Wear on the Nanoscale*. in NanoScience and Technology. Cham: Springer International Publishing, 2015. doi: 10.1007/978-3-319-10560-4.
- [28] C. Munuera, E. Barrena, and C. Ocal, 'Deciphering Structural Domains of

- Alkanethiol Self-Assembled Configurations by Friction Force Microscopy', *J. Phys. Chem. A*, vol. 111, no. 49, pp. 12721–12726, Dec. 2007, doi: 10.1021/jp076127t.
- [29] M. Paradinas, C. Munuera, C. Silien, M. Buck, and C. Ocal, 'Heterogeneous nanotribological response of polymorphic self-assembled monolayers arising from domain and phase dependent friction', *Phys Chem Chem Phys*, vol. 15, no. 4, pp. 1302–1309, 2013, doi: 10.1039/C2CP43769D.
- [30] D. F. Ogletree, R. W. Carpick, and M. Salmeron, 'Calibration of frictional forces in atomic force microscopy', *Rev. Sci. Instrum.*, vol. 67, no. 9, pp. 3298–3306, Sep. 1996, doi: 10.1063/1.1147411.
- [31] M. Nonnenmacher, M. P. o'Boyle, and H. K. Wickramasinghe, 'Kelvin probe force microscopy', *Appl. Phys. Lett.*, vol. 58, no. 25, pp. 2921–2923, 1991.
- [32] S. Sadewasser and T. Glatzel, *Kelvin probe force microscopy*, vol. 48. Springer, 2012.
- [33] Th. Glatzel, M. Ch. Lux-Steiner, E. Strassburg, A. Boag, and Y. Rosenwaks, 'Principles of Kelvin Probe Force Microscopy', in *Scanning Probe Microscopy*, S. Kalinin and A. Gruverman, Eds., New York, NY: Springer New York, 2007, pp. 113–131. doi: 10.1007/978-0-387-28668-6_5.
- [34] W. Melitz, J. Shen, A. C. Kummel, and S. Lee, 'Kelvin probe force microscopy and its application', *Surf. Sci. Rep.*, vol. 66, no. 1, pp. 1–27, 2011.
- [35] W. A. Zisman, 'A NEW METHOD OF MEASURING CONTACT POTENTIAL DIFFERENCES IN METALS', *Rev. Sci. Instrum.*, vol. 3, no. 7, pp. 367–370, Jul. 1932, doi: 10.1063/1.1748947.
- [36] Lord Kelvin, 'V. Contact electricity of metals', *Lond. Edinb. Dublin Philos. Mag. J. Sci.*, vol. 46, no. 278, pp. 82–120, Jul. 1898, doi: 10.1080/14786449808621172.
- [37] N. W. Ashcroft and N. D. Mermin, *Solid state physics*. 1976.

- [38] J. Daillant and A. Gibaud, *X-ray and neutron reflectivity: principles and applications*, vol. 770. Springer, 2008.
- [39] R. Feidenhans, ‘Surface structure determination by X-ray diffraction’, *Surf. Sci. Rep.*, vol. 10, no. 3, pp. 105–188, 1989.
- [40] *X-Ray Scattering from Soft-Matter Thin Films*, vol. 148. 1999.
- [41] L. G. Parratt, ‘Surface Studies of Solids by Total Reflection of X-Rays’, *Phys Rev*, vol. 95, no. 2, pp. 359–369, Jul. 1954, doi: 10.1103/PhysRev.95.359.
- [42] M. Birkholz, *Thin film analysis by X-ray scattering*. John Wiley & Sons, 2006.
- [43] J. Rivnay, S. C. B. Mannsfeld, C. E. Miller, A. Salleo, and M. F. Toney, ‘Quantitative Determination of Organic Semiconductor Microstructure from the Molecular to Device Scale’, *Chem. Rev.*, vol. 112, no. 10, pp. 5488–5519, Oct. 2012, doi: 10.1021/cr3001109.
- [44] G. Ashiotis *et al.*, ‘The fast azimuthal integration Python library: pyFAI’, *J. Appl. Crystallogr.*, vol. 48, no. 2, pp. 510–519, 2015.
- [45] N. Koch, ‘Energy levels at interfaces between metals and conjugated organic molecules’, *J. Phys. Condens. Matter*, vol. 20, no. 18, p. 184008, May 2008, doi: 10.1088/0953-8984/20/18/184008.
- [46] J. Zaumseil and H. Sirringhaus, ‘Electron and Ambipolar Transport in Organic Field-Effect Transistors’, *Chem. Rev.*, vol. 107, no. 4, pp. 1296–1323, Apr. 2007, doi: 10.1021/cr0501543.
- [47] K. A. Mazzi and C. K. Luscombe, ‘Correction: The future of organic photovoltaics’, *Chem Soc Rev*, vol. 44, no. 15, pp. 5744–5744, 2015, doi: 10.1039/C5CS90059J.
- [48] G. Horowitz, ‘Organic thin film transistors: From theory to real devices’, *J. Mater. Res. - J MATER RES*, vol. 19, pp. 1946–1962, Jul. 2004, doi:

10.1557/JMR.2004.0266.

- [49] I. Kyriakidis, *Organic Field Effect Transistors: Theory, Fabrication and Characterization*. in Integrated Circuits and Systems. Springer US, 2008. [Online]. Available: https://books.google.es/books?id=GD_ry6FtSEQC
- [50] H. Klauk, 'Organic thin-film transistors', *Chem Soc Rev*, vol. 39, no. 7, pp. 2643–2666, 2010, doi: 10.1039/B909902F.
- [51] S. Riera-Galindo, F. Leonardi, R. Pfattner, and M. Mas-Torrent, 'Organic Semiconductor/Polymer Blend Films for Organic Field-Effect Transistors', *Adv. Mater. Technol.*, vol. 4, no. 9, p. 1900104, Sep. 2019, doi: 10.1002/admt.201900104.
- [52] Z. A. Lamport, H. F. Haneef, S. Anand, M. Waldrip, and O. D. Jurchescu, 'Tutorial: Organic field-effect transistors: Materials, structure and operation', *J. Appl. Phys.*, vol. 124, no. 7, p. 071101, Aug. 2018, doi: 10.1063/1.5042255.
- [53] G. Horowitz, 'Organic Field-Effect Transistors', *Adv. Mater.*, vol. 10, no. 5, pp. 365–377, Mar. 1998, doi: 10.1002/(SICI)1521-4095(199803)10:5<365::AID-ADMA365>3.0.CO;2-U.

Part II

RESULTS AND DISCUSSION

PAPER I

*Temperature-induced Polymorphism of a Benzothiophene
Derivative: Reversibility and Impact on the Thin Film
Morphology*



Cite this: *Phys. Chem. Chem. Phys.*,
2022, **24**, 24562

Temperature-induced polymorphism of a benzothiophene derivative: reversibility and impact on the thin film morphology†

Shunya Yan,^a Alba Cazorla,^{id}^a Adara Babuji,^a Eduardo Solano,^{id}^b Christian Ruzié,^c
Yves H. Geerts,^{cd} Carmen Ocal^{id}^{*a} and Esther Barrena^{id}^{*a}

The identification of polymorphs in organic semiconductors allows for establishing structure-property relationships and gaining understanding of microscopic charge transport physics. Thin films of 2,7-bis(octyloxy)[1]benzothieno[3,2-*b*]-benzothiophene (C₈O–BTBT–OC₈) exhibit a substrate-induced phase (SIP) that differs from the bulk structure, with important implications for the electrical performance in organic field effect transistors (OFETs). Here we combine grazing incidence wide-angle X-ray scattering (GIWAXS) and atomic force microscopy (AFM) to study how temperature affects the morphology and structure of C₈O–BTBT–OC₈ films grown by physical vapor deposition on SiO₂. We report a structural transition for C₈O–BTBT–OC₈ films, from the SIP encountered at room temperature (RT) to a high temperature phase (HTP) when the films are annealed at a temperature $T \geq 90$ °C. In this HTP structure, the molecules are packed with a tilt angle ($\approx 39^\circ$ respect to the surface normal) and an enlarged in-plane unit cell. Although the structural transition is reversible on cooling at RT, AFM reveals that molecular layers at the SiO₂ interface can remain with the HTP structure, buried under the film ordered in the SIP. For annealing temperatures close to 150 °C, dewetting occurs leading to a more complex morphological and structural scenario upon cooling, with coexistence of different molecular tilts. Because the molecular packing at the interface has direct impact in the charge carrier mobility of OFETs, identifying the different polymorphs of a material in the thin film form and determining their stability at the interfaces are key factors for device optimization.

Received 28th July 2022,
Accepted 27th September 2022

DOI: 10.1039/d2cp03467k

rsc.li/pccp

Introduction

Organic semiconductor (OSC) thin films based on π -conjugated molecules are of enormous interest as active components for electronic devices. The field has seen radical improvements in the last decades with an increasing number of products in the marketplace such as the organic light-emitting diode (OLED) display technology.^{1,2} The development of organic field effect transistors (OFETs) has not been as fast as for OLEDs and although OFETs have become a commercially viable technology, many issues related to fundamental research still remain elusive.^{3,4}

The charge carrier mobility, which is one of the main performance metrics for OFETs, relies on structural details at different length scales that are not yet fully understood and satisfactorily controllable.^{5–8} The crystalline structure adopted by small conjugated molecules is held by weak intermolecular van der Waals interactions, which confer to the OSC materials a high degree of polymorphism. The identification of new or specific polymorphs allows for establishing structure-property relationships and gaining an understanding of microscopic charge transport physics. In addition, polymorphism can represent an added value as it provides access *via* growth conditions to metastable phases, otherwise inaccessible under equilibrium conditions.⁹ In particular, the solid-surface on which a thin film grows, can give rise to surface-induced polymorphism.¹⁰ Hence, for thin films of some molecular materials it is observed that the substrate stabilizes a molecular packing that is different from the bulk structure. The so-called thin-film phase of pentacene is the best-known example of surface-induced phase (SIP).^{10–13} Because the degree of crystalline order and morphology of on-surface developed structures are influenced by both, kinetic and thermodynamic factors, the optimization of thin film OFETs requires exploring different

^a Institut de Ciència de Materials de Barcelona (ICMAB-CSIC), 08193 Bellaterra, Barcelona, Spain. E-mail: e.barrena@csic.es, cocal@icmab.es

^b ALBA synchrotron, C/de la Llum 2-26, Cerdanyola del Vallès, Barcelona, 08290, Spain

^c Laboratoire de Chimie des Polymères, Faculté des Sciences, Université Libre de Bruxelles (ULB), Boulevard du Triomphe, CP 206/01, 1050 Bruxelles, Belgium

^d International Solvay Institutes of Physics and Chemistry, Université Libre de Bruxelles (ULB), Boulevard du Triomphe, CP 231, 1050 Bruxelles, Belgium

† Electronic supplementary information (ESI) available. See DOI: <https://doi.org/10.1039/d2cp03467k>

growth parameters, including substrate temperature during growth. As the molecular packing crucially determines the properties of a material, polymorphism can have a direct impact on the functional properties and time stability of devices.¹⁴

Alkylated BTBT derivatives (C_n -BTBT- C_n) exhibit a high carrier mobility ($3\text{--}20\text{ cm}^2\text{ V}^{-1}\text{ s}^{-1}$),^{15–19} which has been related to their tendency to grow on the SiO_2 surface forming well-ordered layers of standing molecules with a herringbone (HB) arrangement of the BTBT cores.²⁰ The crystalline packing in the thin-film state is similar to that in the bulk single crystals.^{18,21,22} For 2,7-dioctyloxy[1]benzothieno[3,2-*b*]benzothiophene ($C_8\text{O}$ -BTBT- OC_8), with an oxygen atom added between the BTBT and each alkyl chain, important structural differences are found. The thermodynamically stable crystalline phase (single-crystal structure) consists of a triclinic structure with two molecules per unit cell exhibiting a co-facial stacking in which adjacent molecules are displaced respect to each other along the *c*-axis.^{21,23,24} In thin films, however, the presence of a SIP structure has been reported, which consists of a lamellar arrangement of the molecules with herringbone packing of the BTBT cores within the lamellae.^{23–26} The reported SIP for $C_8\text{O}$ -BTBT- OC_8 is isostructural with the C_8 -BTBT- C_8 structure.¹⁰ A difference from the bulk phase, which presents an inter-digitation of the alkyl chains, the (001) plane of the SIP conforms to a flat substrate surface. The HB structure of $C_8\text{O}$ -BTBT- OC_8 has been observed to form on surfaces for films prepared from vapour deposition²⁶ as well as from solution processing.^{14,23–25} A charge carrier mobility about $1\text{ cm}^2\text{ V}^{-1}\text{ s}^{-1}$ has been reported for OFETs based on thin films presenting the SIP phase.¹⁴ Although this mobility is lower than that reported for C_8 -BTBT- C_8 OFETs, the investigation of the electrical properties has been scarce and there is possible room for improvement *via* processing or post-processing methods (e.g., solvent or thermal annealing). Previous studies have reported that time or solvent vapour annealing lead to a conversion towards the bulk structure,²⁴ indicating that the SIP is metastable. The effect of temperature as a parameter has not yet been explored.

In this work, we combine synchrotron Grazing-Incidence Wide-Angle X-ray Scattering (GIWAXS) and Atomic Force Microscopy (AFM) to characterize the films grown by physical vapour deposition on the native oxide surface of p-doped Si wafers. We investigate the effect of temperature, either by using different substrate temperatures during the growth or by post-annealing treatments of films deposited at room temperature (RT).

Experimental section

GIWAXS experiments were performed at the BL11-NCD-SWEET beamline of the ALBA Synchrotron (Spain) using a photon energy of $h\nu = 12.4\text{ keV}$. Different incident angles were used, ranging between 0.09° and 0.15° , ensuring measurements with surface sensitivity or full thin film penetration while minimizing the substrate contribution. A large-area 2D Rayonix LX 255-HS detector, which consists of a pixel array of 2880×960 ($V \times H$) with a pixel size of $88.54 \times 88.54\text{ }\mu\text{m}^2$ for the binning employed,

was used to capture 2D images of the diffraction patterns. The scattering vector (q) was calibrated using Cr_2O_3 as a calibration standard and pyFAI python library.²⁸ To improve the signal-to-noise ratio and to check beam damage, 50 images with an exposure time of 0.02 s were acquired and summed up at each temperature and for each incident angle. The conversion of the data to the reciprocal space was performed by using a developed python routine, obtaining the out-of-plane (OOP), q_z , and in-plane (IP), q_{xy} , components of the scattering vector corresponding to the directions perpendicular and parallel to the surface, respectively. Because of the grazing incidence geometry, a section cut obtained along the vertical direction of the detector (so-called OOP section cuts in the text) is not the real specular scan. 2D GIWAXS patterns of annealed samples were collected *in situ* using the available Linkam TMS600 heating stage adapted for grazing incidence experiments to monitor the structural changes. Scattering patterns were recorded under N_2 gas flow with a step-wise temperature profile, which consisted of a fast heating ramp ($150\text{ }^\circ\text{C min}^{-1}$) and 5 minutes of annealing time before data collection. A set of twin samples was annealed in a heating plate (5 minutes annealing time in ambient conditions) and measured at room temperature by AFM. In the extraction of the lattice parameters we have considered the uncertainty given by the error propagation in the equation, considering the uncertainty of the peak position, *i.e.*, the error of the Gaussian fit for each peak. In this way the obtained uncertainty is $<0.0008\text{ }\text{\AA}$ for *b* and $<0.02\text{ }\text{\AA}$ for *a*.

$C_8\text{O}$ -BTBT- OC_8 was synthesized as previously reported.^{21,24} Before films growth, the silicon substrates (Si-Mat, Germany) were cleaned by sonication in acetone and ethanol, for 10 minutes in each solution, and degassed in vacuum ($\sim 10^{-6}\text{--}10^{-7}\text{ mbar}$) for 15 minutes at $250\text{ }^\circ\text{C}$. The thin films of $C_8\text{O}$ -BTBT- OC_8 were grown by physical vapour deposition in the same vacuum chamber, the growth rate and film thickness were about $2\text{--}3\text{ }\text{\AA min}^{-1}$ and 14 nm, respectively, as monitored by a quartz crystal microbalance (QCM). For post-growth annealing the samples were kept 5 minutes at the desired temperature.

AFM measurements in contact and dynamic modes were performed at RT using a commercial instrument (Cypher ES, Oxford instruments). For contact mode, silicon nitride tips were used (cantilevers with a nominal spring constant $k = 0.02$ or 0.03 N m^{-1} from Bruker) whereas for dynamic mode we used Cr/Pt-coated silicon tips (cantilevers with a nominal spring constant $k = 3\text{ N m}^{-1}$, from BudgetSensors). AFM data we analyzed with AR SPM Software from Oxford Instruments and WxSM freeware²⁷ from Nanotech Electronica.

Results

1. Structural analysis by GIWAXS

Thin films of $C_8\text{O}$ -BTBT- OC_8 (thickness $\approx 14\text{ nm}$) were deposited by physical vapour deposition in vacuum on silicon wafers at RT. The film structure was measured by GIWAXS during post-growth stepwise annealing of the sample (see the Experimental section). Fig. 1a displays 2D GIWAXS patterns acquired at different temperatures (patterns for other temperatures are displayed in Fig. S1, ESI†).



Section cuts along the OOP and IP directions are provided in Fig. 1b and c, respectively.

The diffraction pattern measured at RT agrees with the reported HB structure for the C_8O -BTBT- OC_8 SIP, oriented with the (001) plane parallel to the surface. The (001) crystalline plane in the SIP forms a flat and compact surface formed by densely packed alkyl chains that is stabilized by the flat surface. In the 2D GIWAXS pattern of Fig. 1a, the scattering intensity visible at $q_{xy} \approx 1.33 \text{ \AA}^{-1}$, 1.64 \AA^{-1} and 1.95 \AA^{-1} have been indexed as $(-1-1l)$, $(02l)$ and $(-12l)$, respectively. Such pattern, with the absence of scattering intensity for $(10l)$ or $(0\bar{1}l)$, is indicative of an in-plane rectangular cell ($\gamma = 90^\circ$) with two molecules per unit cell. The in-plane deduced unit cell (Table 1) agrees with the previously reported,¹⁰ but with a slightly lower value of the b -lattice parameter ($<1\%$). The Bragg peak position in the OOP direction ($q = 0.204 \text{ \AA}^{-1}$) has an associated inter-planar spacing of $d = 30.8 \text{ \AA}$ in agreement with previous reports, although the (001) Bragg peak appears at a slightly larger q -position (Fig. S1 in ESI†). The average molecular tilt respect to the surface normal, estimated from the molecular length ($L = 33.88 \text{ \AA}$) and the inter-planar distance results in $\theta \approx 24^\circ$, corresponding to the tilt of the alkyl chains in this structure.²⁴

At a temperature of $\approx 90^\circ \text{C}$, a remarkable change in the diffraction pattern points to the formation of a new polymorphic phase. Hereafter, this phase is referred to as the high temperature phase (HTP). As it can be appreciated in Fig. 1b,

Table 1 Unit-cell parameters of the C_8O -BTBT- OC_8 film for the two observed structures. The parameters of the HTP structure are obtained from the GIWAXS acquired at 90°C

	C_8O -BTBT- OC_8 (SIP)	C_8O -BTBT- OC_8 (HTP)
Crystal system	Monoclinic	Monoclinic
a (\AA)	6.02	7.05
b (\AA)	7.66	7.87
c (\AA)	31.08	29.2
α ($^\circ$)	90	90
β ($^\circ$)	97	63.9
γ ($^\circ$)	90	90

the structural transition involves a shift of the (001) Bragg peak to a larger q ($q = 0.237 \text{ \AA}^{-1}$), which leads to $d_{\text{HTP}} \approx 26.5 \text{ \AA}$, a considerably reduced inter-planar spacing. In the 2D GIWAXS pattern still three rods are visible at $q_{xy} \approx 1.17 \text{ \AA}^{-1}$, 1.58 \AA^{-1} and 1.81 \AA^{-1} , *i.e.*, shifted respect to those for the SIP structure (Fig. 1a and c). Note that the structural change is accompanied by a marked variation in the intensity distribution along q_z . Although there are not enough independent Bragg diffraction peaks to determine the six lattice constants (a , b , c , α , β and γ) of the crystallographic unit cell, the analysis can be simplified by some reasonable assumptions. The absence of diffraction features in the low q_{xy} region (*i.e.*, absence of $(10l)$ and $(0\bar{1}l)$) allows us to presume that the symmetry of the unit cell is preserved; therefore, the three rods can be indexed as $(-1-1l)$, $(02l)$ and $(-12l)$. Under these assumptions, there are only four parameters to be determined in the monoclinic unit cell: a , b , c and β (the angle between c and a). The lattice parameters a and b can be directly extracted from the peak position of the (020) and the q_{xy} component of the $(-1-10)$ rod; c and β are deduced from the q_z component of the $(-1-10)$ reflection ($q_z = 0.44 \text{ \AA}^{-1}$) and the (001) Bragg position. Further details are presented in the ESI†. The calculated lattice parameters are given in Table 1. The in-plane unit cell changes from $a_{\text{SIP}} = 6.02 \text{ \AA}$ and $b_{\text{SIP}} = 7.66 \text{ \AA}$ in the SIP to $a_{\text{HTP}} = 7.05 \text{ \AA}$ and $b_{\text{HTP}} = 7.87 \text{ \AA}$ in the HTP. The enlargement of the lattice parameter a and the reduction of the angle β are the most noticeable changes in the structural transition. Overall, the changes observed by GIWAXS are consistent with a scenario in which the molecules are tilted with respect to the surface normal. Notably, the intensity of the $(02l)$ reflection remains in-plane while the scattering intensity in the $(-1-1l)$ and $(-12l)$ is enhanced out-of-plane, indicating that the molecules are tilted towards the a -axis. Given that the BTBT cores are the most electron-dense parts of the molecule, the observed intensity enhancement along the $(-11l)$ and $(-12l)$ rods can be interpreted as a sign of the tilt of the BTBT cores (not uniquely the alkyl chains). The average molecular tilt from the surface normal estimated from the molecular length and d_{HTP} is $\theta \approx 38.5^\circ$, without taking into account any possible tilt difference between core and alkyl chains.

We have used the GIDSimulator software²⁹ to simulate the diffraction pattern with the extracted parameters for the HTP, obtaining the diffraction spots (Fig. 2a), which match with the recorded scattering pattern. The temperature induced structural transition from the SIP to the HTP is illustrated in Fig. 2b.

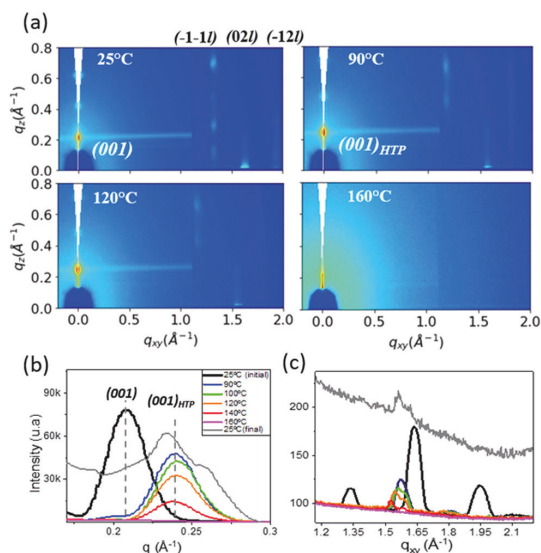


Fig. 1 (a) 2D GIWAXS patterns of a C_8O -BTBT- OC_8 thin-film (incidence angle of 0.13°) acquired at the indicated temperatures. The horizontal line appearing at $q_z \approx 0.24 \text{ \AA}^{-1}$ is produced by the CCD camera blooming due to the high intense signal of the (001) peak. Line cuts along the out-of-plane (b) and in-plane (c) directions. Additional 2D GIWAXS patterns and OOP cuts (larger q range) are provided in Fig. S1 (ESI†) for all employed temperatures. The data acquired at RT after annealing the film at 160°C in (b) and (c) have been multiplied by a factor of 5 (grey lines).



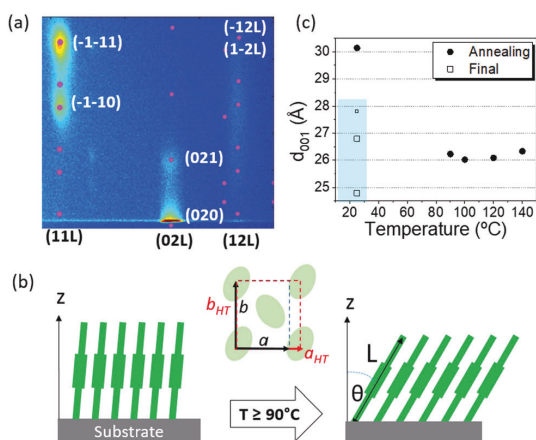


Fig. 2 (a) 2D diffraction pattern measured at 90 °C and simulated pattern (pink dots) for the HTP structure with the unit cell parameters given in Table 1. (b) Sketch illustrating the main changes involved in the structural transition from the SIP to the HTP structure with annealing temperature: tilting of the molecules and expansion of the a -lattice parameter. (c) Inter-planar spacing at different temperatures extracted from the (001) peak. After annealing, the film was cooled down and measured at 25 °C (final); the values appear with square symbols, the smaller size of one of them indicates the lower intensity of the corresponding peak (see Fig S2 in ESI†).

The HTP remains visible for substrate temperatures above 90 °C. Nevertheless, the peaks show a visible reduction of the intensity beyond 100 °C (see Fig. 1b and c), a fact that indicates that some molecular desorption occurs induced by thermal annealing. The absence of diffraction features at 160 °C (pink lines) can be interpreted as the full desorption of the film and/or as a change into a disordered state. Indeed, measurements taken at RT, after cooling down the film, reveal the presence of fairly faint structural features, confirming the desorption of most of the film. The OOP intensity (grey line in Fig. 1b) shows two dominant peaks at $q_z = 0.235 \text{ \AA}^{-1}$ and 0.258 \AA^{-1} (see fitting details in Fig. S2 in ESI†), corresponding to an interlayer spacing of 26.7 Å and 24.3 Å, respectively. This observation is interpreted as the coexistence of different tilt angles in the remaining molecular film. Furthermore, the in-plane data (grey line in Fig. 1c and Fig. S2, ESI†) shows a weak in-plane intensity at 1.58 \AA^{-1} that gives evidence of a molecular layer with prevalence of the HTP structure. The values of the d_{001} spacing calculated at each temperature have been displayed in Fig. 2c. In the following, we address the reversibility of the structural transition by AFM as well as the impact that the substrate temperature during growth has on the morphology of the films.

2. Thin film morphology analysis by AFM

Fig. 3a shows the surface morphology of a $\text{C}_8\text{O-BTBT-OC}_8$ thin film (14 nm nominal thickness) deposited on the SiO_2 substrate at RT (25 °C). As it can be seen in the displayed images, the surface exhibits a quite laterally homogeneous morphology. The magnified image at the inset shows terraced islands with a round shape on top of a continuous film. Taking into account

the QCM nominal thickness, the continuous film is estimated to be formed by four complete single molecular layers. A step height of $3.2 \pm 0.1 \text{ nm}$ is obtained (Fig. S3, ESI†), which is in agreement with the reported interlayer distance of the SIP structure.²⁴ The consequences that post-growth annealing has on the film morphology can be seen in Fig. 3 for 100 °C (b), 130 °C (c) and 150 °C (d). We note that all AFM images were obtained after the sample was allowed to cool down at RT after each annealing treatment.

Several important changes in the morphology are observed for the sample post-annealed to 100 °C (Fig. 3b). On the one hand, the number of levels exposed at the film surface is lower than in the as-grown film. The height of the individual layers is the same as in as-deposited films, indicating that the structural transition observed by GIWAXS is reversible and that the HTP transforms back to the SIP structure after cooling down. On the other hand, the top-most layer consists of laterally extended

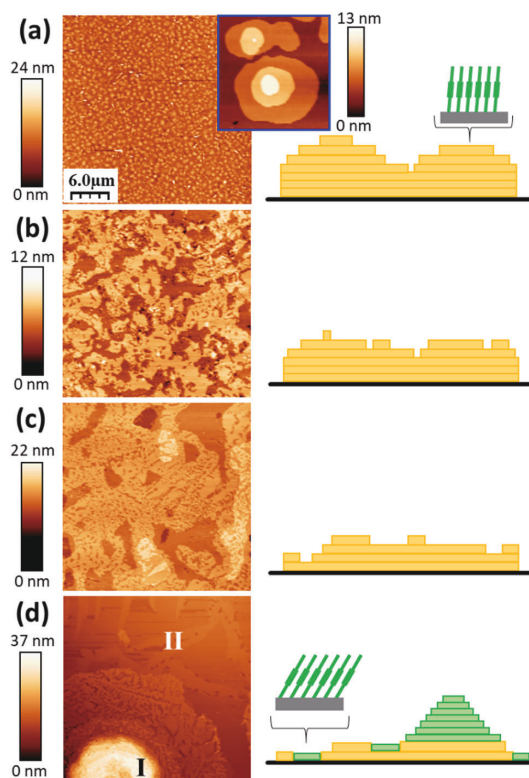


Fig. 3 AFM topographic images of 14 nm (nominal) of $\text{C}_8\text{O-BTBT-OC}_8$ deposited on SiO_2 at RT (25 °C) (a) and after post-annealing during 5 min at diverse temperatures: 100 °C (b), 130 °C (c) and 150 °C (d). The lateral size of the large images is $30 \mu\text{m} \times 30 \mu\text{m}$ and the dimensions of the image in the inset in (a) is $210 \text{ nm} \times 210 \text{ nm}$. The cartoons are schematic representations of the respective film morphology based on topographic profiles analysis of the images. Yellow color is associated to SIP (upright molecules) and green to tilted molecular layers. Note: all images were taken at RT.



islands that cover about 62% of the surface and shows small voids of one single layer depth. These holes might be the combined result of non-filled space after coalescence of the lateral growing regions and molecular desorption. This sort of flattening process is explained by an increased mobility of the molecules on the surface and a reduction of the Ehrlich-Schwoebel barrier when increasing the temperature.³⁰ The post-annealing treatment done has a smoothening effect on the morphology. After annealing the film at 130 °C (Fig. 3c), a further lateral enlargement of the terraces (with lateral sizes surpassing tens of micrometres) is seen. Despite a large vertical scale arising from newly created pitches reaching the substrate (Fig. S4 in ESI[†]), few topographic levels are seen. Interestingly, the thickness of the film has decreased as determined by the pitches depth, which confirms the initiation of molecular desorption from the film. This observation is fully consistent with the observed decrease of scattering intensity in the GIWAXS pattern for annealing temperatures above ≈ 100 °C.

The surface morphology dramatically changed upon a post-annealing temperature of 150 °C (Fig. 3d). Large multi-layered mounds with a circular shape (domes) appear on the surface (labelled I), with a diameter of several micrometers and a height of some tens of nanometers. These domes cover only about 10% of the surface and are surrounded by a corona and a considerably flat surrounding film (labelled II). Such morphology is characteristic of a film dewetting process. The differences among these two regions are illustrated in Fig. 4. A magnification of the stepped side of one mound is shown in Fig. 4a. We first note that the exposed terraces at this multi-layered region have step heights varying between 2.6 and 2.9 nm, *i.e.*, lower than the interlayer spacing of the SIP structure. This result is quantitatively illustrated in Fig. 4b, where the height distribution of the image recorded in region I is superimposed to a grid made out of vertical dotted lines separated by 3.2 nm, the interlayer distance measured

for the RT film. This observation agrees with the GIWAXS data (Fig. 2c), confirming the coexistence of diverse tilted configurations after cooling the annealed C₈O-BTBT-OC₈ films. There is no clear correlation between the molecular tilt and the terrace level.

As it can be seen in the corresponding magnification (Fig. 4c), region II is fairly flat, consisting of two film surface levels. The uncovered substrate is visible only through a few pinholes or voids (see white arrows in the figure), which allow us determining the layer thickness by topographic profile analysis (Fig. 4d). The molecular layer with the lowest height has a measured thickness that ranges between 2.3 and 2.8 nm, depending on the surface location. The highest level is ~ 3.2 nm thick, as corresponds to that expected for the SIP structure. On the basis of the GIWAXS results, we suggest that these regions correspond to one single molecular layer at the film/SiO₂ interface, that remains in the HTP structure when cooling from high temperature to RT, due to an incomplete transition from the HTP to the SIP. Since the SIP phase is denser than the HTP, voids are formed within the layer (white arrows). Moreover, the thinner molecular layer is easily removed due to the sweeping action of the tip while scanning in contact mode, likely indicating a defective packing (Fig. S5 in ESI[†]).

The impact that the morphological changes have on the surface roughness of the film has been analyzed in terms of the root mean square (RMS) calculated for large scale AFM topographic images (900 μm^2) at the different post-annealing temperatures. The data depicted in Fig. 5a show that the roughness of the as-grown films (RMS = 3 nm) considerably decreases by more than 50% after post-annealing at 100 °C. For subsequent temperature treatments, a relatively low increase of RMS is seen, in accordance with the similar number of exposed levels (Fig. 3b–d). For the post-annealed samples at 150 °C, two values were estimated that correspond to areas including or excluding the tall round mounds (pink and blue symbols, respectively). A plot of the interlayer spacing (layer thickness) measured by AFM after post-annealing at different temperatures is presented in Fig. 5b. From the AFM results, we conclude that the HTP structure reverses to the SIP after cooling the films to RT if the annealing temperature is kept lower than that of the dewetting transition (≈ 150 °C).

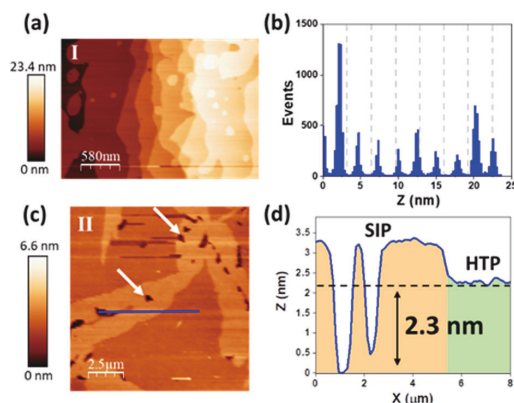


Fig. 4 AFM topographic images taken in region I (a) and region II (c) of the C₈O-BTBT-OC₈ film, at RT after being post-annealed at 150 °C (magnified regions of Fig. 3d). (b) Height distribution of the image in (a), the vertical dotted lines every 3.2 nm serve as a reference to show that the diverse step heights deviate from the interlayer distance measured for the SIP structure. (d) Line profile corresponding to the blue segment in (c).

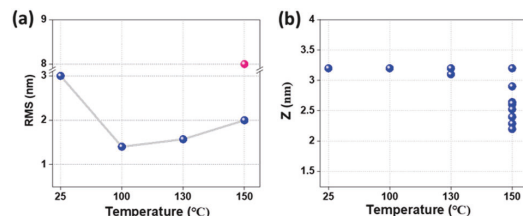


Fig. 5 (a) Root mean squared (RMS) surface roughness for the as-grown sample at 25 °C and for post-annealed films at the indicated temperatures (all measured at RT). The pink symbol corresponds to an area including the multilayer mound of region I of the sample post-annealed at 150 °C. (b) Height of single molecular layers obtained from AFM topographical images after post-annealing at different temperatures (the estimated error is ± 0.1 nm).



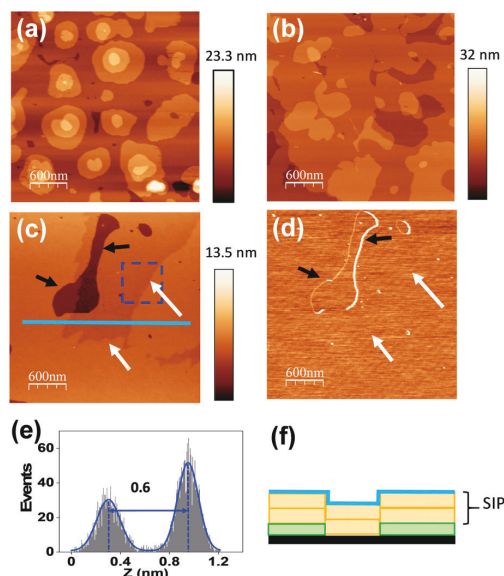


Fig. 6 AFM topographic images obtained at RT for $C_8O-BTBT-OC_8$ films with a nominal thickness of 14 nm grown at 25 °C (a), 85 °C (b) and 130 °C (c). (d) Lateral force image corresponding to (c). (e) Height distribution of the area enclosed within the dashed blue square in (c). Blue lines in (e) are the Gauss fits of the histogram. (f) Schematic cross section sketch of the film along the light blue segment indicated in (c).

In order to gain insight into the role of temperature as a growth parameter, we next analyze the morphology of thin films grown at different substrate temperatures and measured after cooling down to RT. Here the thickness of the films is found to be similar for all the growth temperatures. We note that sample cooling down inside the high vacuum chamber takes place with a lower rate than in the post-annealing experiments. In Fig. 6, the morphology obtained for thin films grown at 25 °C (a), 85 °C (b) and 130 °C (c) can be compared. As expected, increasing the substrate temperature during growth results in smoother films with larger terraces. However, the most important observation is the presence of step heights of only ~ 0.6 nm (white arrows in Fig. 6c). Conversely to higher steps also seen at the surface (black arrows in the figure), the low-height steps do present a particularity: their edges are smoother and show no contrast in the lateral force image (Fig. 6d).

Further comparison between topography and lateral force data are supplied in Fig. S6 (ESI[†]). It is worth noting that the contour of topographical features, in particular steps edges, is commonly distinguished in lateral force images as a result of the cantilever twist during upwards or downwards crossing a step due to topographical effects.³¹ The fact that the low-height steps are not apparent in the lateral force signal suggests that they arise from a buried topographical feature. We propose that the buried steps are due to the boundary SIP and HTP, both present at the film/ SiO_2 interface (Fig. 6f). Remarkably, the upper layers exhibit the SIP structure (also illustrated in Fig. 6f).

This result indicates that in spite of complete reversibility of the polymorphic transition, the molecular interaction with the substrate might stabilize the tilted phase at room temperature.

It is well established that polymorphism can have an important impact on the charge transport. The transfer integral values, which reflect the degree of electronic overlap between electronic levels in neighbouring molecules, can be significantly affected by differences in the molecular packing. In this respect, a theoretical study on strain-induced polymorphism in $C_8-BTB-C_8$ has revealed how the strained in-plane lattice modifies the electronic overlap between neighboring molecules, affecting the bandwidth.³² We note that for practical applications, a tilted arrangement of the BTBT cores in the HTP is expected to result in reduced π -overlap and, herewith, in a lower field-effect mobility in OFETs, a topic worthy of being explored in future studies. The evaluation of the effects that the cooling rate and different annealing protocols have on the structure of $C_8O-BTBT-OC_8$ thin films can help to gain a better understanding of the thermodynamic and kinetic factors affecting the stability of each polymorph.

One of the implications of the present work is that, although the film morphology and crystalline quality of the film can be improved by selecting the adequate growth temperature, even a small fraction of HTP at the interface would affect the device performance. The determination of the exact temperature for the polymorphic transition as well as the impact of the film thickness remain as open questions to be addressed in future studies.

Conclusions

By means of *in situ* GIWAXS measurements during thermal annealing of $C_8O-BTBT-OC_8$ thin films, we have observed a structural transition from the surface induced phase (SIP) encountered at RT to a high temperature phase (HTP) for $T \geq 90$ °C. In this HTP structure, the molecules are packed in a tilted configuration ($\approx 39^\circ$ from the surface normal) that also causes a larger in-plane a lattice parameter. The AFM results allow concluding that the structural transition is reversible, *i.e.*, HTP transforms back to the SIP after cooling down to RT, if the post-annealing temperature is kept lower than 150 °C (transition towards film dewetting). A more complex morphological scenario occurs after annealing at temperatures close to 150 °C, leading to the coexistence of different molecular tilts at RT.

Improved film planarity is obtained if, instead of submitted to relatively short post-annealing treatments, the films are grown at the adequate substrate temperature. AFM data reveals that, on cooling down the films, the HTP to SIP transition may be not fully reversible at the organic/ SiO_2 interface, where molecular layers in the HTP remain buried under the film ordered in the SIP.

The possible coexistence of SIP and HTP at that interface (plausibly affected by both, the annealing protocol and the cooling rate) can have a negative impact on the field-effect mobility in OFETs and deserve a further investigation.



Conflicts of interest

There are no conflicts to declare.

Acknowledgements

This work was funded by the projects PID2019-110907GB-I00 and FUNFUTURE CEX2019-000917-S from MCIN/AEI/10.13039/501100011033. S. Y. is financially supported by the China Scholarship Council (CSC) under Grant No. 202006990034. This work has been carried out within the framework of the doctoral program of Material Science (Department of Physics) of the Universitat Autònoma de Barcelona (UAB). GIWAXS experiments were performed at the beam line BL11 – NCD-SWEET at ALBA Synchrotron with the collaboration of ALBA staff. Y. H. G. is thankful to the Belgian National Fund for Scientific Research (FNRS) for financial support through research projects BTBT (No. 2.4565.11), Phasetrans (No. T.0058.14), Pi-Fast (No. T.0072.18), 2D to 3D (No. 30489208), and DIFFRA (No. U.G001.19). Financial support from the Fédération Wallonie-Bruxelles (ARC No. 20061) is also acknowledged.

References

- H. Sasabe and J. Kido, Recent Progress in Phosphorescent Organic Light-Emitting Devices, *Eur. J. Org. Chem.*, 2013, 7653–7663.
- J. D. Myers and J. Xue, Organic Semiconductors and their Applications in Photovoltaic Devices, *Polym. Rev.*, 2012, 52, 1–37.
- B. Yunlong Guo, G. Yu, Y. Liu, Y. L. Guo, G. Yu and Y. Q. Liu, Functional Organic Field-Effect Transistors, *Adv. Mater.*, 2010, 22, 4427–4447.
- C. Wang, X. Zhang, H. Dong, X. Chen and W. Hu, Challenges and Emerging Opportunities in High-Mobility and Low-Energy-Consumption Organic Field-Effect Transistors, *Adv. Energy Mater.*, 2020, 10, 2000955.
- S. Ahmed and J. Yi, Two-dimensional transition metal dichalcogenides and their charge carrier mobilities in field-effect transistors, *Nano-Micro Lett.*, 2017, 9, 1–23.
- G. Schweicher, Y. Olivier, V. Lemaure and Y. H. Geerts, What Currently Limits Charge Carrier Mobility in Crystals of Molecular Semiconductors?, *Isr. J. Chem.*, 2014, 54, 595–620.
- R. J. Kline and M. D. McGehee, Morphology and Charge Transport in Conjugated Polymers, *J. Macromol. Sci.*, 2007, 46, 27–45.
- S. Fratini, M. Nikolka, A. Salleo, G. Schweicher and H. Sirringhaus, Charge transport in high-mobility conjugated polymers and molecular semiconductors, *Nat. Mater.*, 2020, 19, 491–502.
- D. Gentili, M. Gazzano, M. Melucci, D. Jones and M. Cavallini, Polymorphism as an additional functionality of materials for technological applications at surfaces and interfaces, *Chem. Soc. Rev.*, 2019, 48, 2502–2517.
- A. O. F. Jones, B. Chattopadhyay, Y. H. Geerts and R. Resel, Substrate-Induced and Thin-Film Phases: Polymorphism of Organic Materials on Surfaces, *Adv. Funct. Mater.*, 2016, 26, 2233–2255.
- R. Ruiz, D. Choudhary, B. Nickel, T. Toccoli, K. C. Chang, A. C. Mayer, P. Clancy, J. M. Blakely, R. L. Headrick, S. Iannotta and G. G. Malliaras, Pentacene thin film growth, *Chem. Mater.*, 2004, 16, 4497–4508.
- S. E. Fritz, S. M. Martin, C. D. Frisbie, M. D. Ward and M. F. Toney, Structural Characterization of a Pentacene Monolayer on an Amorphous SiO₂ Substrate with Grazing Incidence X-ray Diffraction, *J. Am. Chem. Soc.*, 2004, 126, 4084–4085.
- S. C. B. Mannsfeld, A. Virkar, C. Reese, M. F. Toney and Z. Bao, Precise Structure of Pentacene Monolayers on Amorphous Silicon Oxide and Relation to Charge Transport, *Adv. Mater.*, 2009, 21, 2294–2298.
- T. Salzillo, A. Campos, A. Babuji, R. Santiago, S. T. Bromley, C. Ocal, E. Barrena, R. Jouclas, C. Ruzié, G. Schweicher, Y. H. Geerts and M. Mas-Torrent, Enhancing Long-Term Device Stability Using Thin Film Blends of Small Molecule Semiconductors and Insulating Polymers to Trap Surface-Induced Polymorphs, *Adv. Funct. Mater.*, 2020, 30, 2006115.
- C. Ruzié, J. Karpinska, A. Laurent, L. Sanguinet, S. Hunter, T. D. Anthopoulos, V. Lemaure, J. Cornil, A. R. Kennedy, O. Fenwick, P. Samori, G. Schweicher, B. Chattopadhyay and Y. H. Geerts, Design, synthesis, chemical stability, packing, cyclic voltammetry, ionisation potential, and charge transport of [1] benzothieno[3,2-*b*][1]benzothiophene derivatives, *J. Mater. Chem. C*, 2016, 4, 4863–4879.
- Y. Tsutsui, G. Schweicher, B. Chattopadhyay, T. Sakurai, J. B. Arlin, C. Ruzié, A. Aliev, A. Ciesielski, S. Colella, A. R. Kennedy, V. Lemaure, Y. Olivier, R. Hadji, L. Sanguinet, F. Castet, S. Osella, D. Dudenko, D. Beljonne, J. Cornil, P. Samori, S. Seki and Y. H. Geerts, Unraveling Unprecedented Charge Carrier Mobility through Structure Property Relationship of Four Isomers of Didodecyl[1]benzothieno[3,2-*b*][1]benzothiophene, *Adv. Mater.*, 2016, 28, 7106–7114.
- K. He, W. Li, H. Tian, J. Zhang, D. Yan, Y. Geng and F. Wang, Asymmetric Conjugated Molecules Based on [1]Benzothieno[3,2-*b*][1]benzothiophene for High-Mobility Organic Thin-Film Transistors: Influence of Alkyl Chain Length, *ACS Appl. Mater. Interfaces*, 2017, 9, 35427–35436.
- K. Takimiya, I. Osaka, T. Mori and M. Nakano, Organic semiconductors based on [1]benzothieno[3,2-*b*][1]benzothiophene substructure, *Acc. Chem. Res.*, 2014, 47, 1493–1502.
- P. Xie, T. Liu, J. Sun and J. Yang, Structures, Properties, and Device Applications for [1]Benzothieno[3,2-*b*]Benzothiophene Derivatives, *Adv. Funct. Mater.*, 2022, 32, 202200843.
- A. Babuji, F. Silvestri, L. Pithan, A. Richard, Y. H. Geerts, N. Tessler, O. Solomeshch, C. Ocal and E. Barrena, Effect of the Organic Semiconductor Side Groups on the Structural and Electronic Properties of Their Interface with Dopants, *ACS Appl. Mater. Interfaces*, 2020, 12, 57578–57586.
- C. Ruzié, J. Karpinska, A. Laurent, L. Sanguinet, S. Hunter, T. D. Anthopoulos, V. Lemaure, J. Cornil, A. R. Kennedy, O. Fenwick, P. Samori, G. Schweicher, B. Chattopadhyay



- and Y. H. Geerts, Design, synthesis, chemical stability, packing, cyclic voltammetry, ionisation potential, and charge transport of [1]benzothieno[3,2-*b*][1]benzothiophene derivatives, *J. Mater. Chem. C*, 2016, **4**, 4863–4879.
- 22 G. Gbabode, M. Dohr, C. Niebel, J. Y. Balandier, C. Ruzié, P. Négrier, D. Mondieig, Y. H. Geerts, R. Resel and M. Sferrazza, X-ray structural investigation of nonsymmetrically and symmetrically alkylated [1]benzothieno[3,2-*b*]benzothiophene derivatives in bulk and thin films, *ACS Appl. Mater. Interfaces*, 2014, **6**, 13413–13421.
 - 23 N. Bedoya-Martínez, B. Schrode, A. O. F. Jones, T. Salzillo, C. Ruzié, N. Demitri, Y. H. Geerts, E. Venuti, R. G. Della Valle, E. Zojer and R. Resel, DFT-Assisted Polymorph Identification from Lattice Raman Fingerprinting, *J. Phys. Chem. Lett.*, 2017, **8**, 3690–3695.
 - 24 A. O. F. Jones, Y. H. Geerts, J. Karpinska, A. R. Kennedy, R. Resel, C. Röthel, C. Ruzié, O. Werzer and M. Sferrazza, Substrate-induced phase of a [1]benzothieno[3,2-*b*]benzothiophene derivative and phase evolution by aging and solvent vapor annealing, *ACS Appl. Mater. Interfaces*, 2015, **7**, 1868–1873.
 - 25 B. Schrode, A. O. F. Jones, R. Resel, N. Bedoya, R. Schennach, Y. H. Geerts, C. Ruzié, M. Sferrazza, A. Brillante, T. Salzillo and E. Venuti, Substrate-Induced Phase of a Benzothiophene Derivative Detected by Mid-Infrared and Lattice Phonon Raman Spectroscopy, *ChemPhysChem*, 2018, **19**, 993–1000.
 - 26 H. Spreitzer, B. Kaufmann, C. Ruzié, C. Röthel, T. Arnold, Y. H. Geerts, C. Teichert, R. Resel and A. O. F. Jones, Alkyl chain assisted thin film growth of 2,7-dioctyloxy-benzothienobenzothiophene, *J. Mater. Chem. C*, 2019, **7**, 8477–8484.
 - 27 I. Horcas, R. Fernández, J. M. Gómez-Rodríguez, J. Colchero, J. Gómez-Herrero and A. M. Baro, WSXM: A software for scanning probe microscopy and a tool for nanotechnology, *Rev. Sci. Instrum.*, 2007, **78**, 013705.
 - 28 G. Ashiotis, A. Deschildre, Z. Nawaz, J. P. Wright, D. Karkoulis, F. E. Picca and J. Kieffer, The fast azimuthal integration Python library: pyFAI, *J. Appl. Crystallogr.*, 2015, **48**, 510–519.
 - 29 D. W. Breiby, O. Bunk, J. W. Andreasen, H. T. Lemke and M. M. Nielsen, Simulating X-ray diffraction of textured films, *J. Appl. Crystallogr.*, 2008, **41**, 262–271.
 - 30 G. Hlawacek, P. Puschnig, P. Frank, A. Winkler, C. Ambrosch-Drax and C. Teichert, Characterization of step-edge barriers in organic thin-film growth, *Science*, 2008, **321**, 108–111.
 - 31 T. Müller, M. Lohrmann, T. Kässer, O. Marti, J. Mlynek and G. Krausch, Frictional Force between a Sharp Asperity and a Surface Step, *Phys. Rev. Lett.*, 1997, **79**, 5066–5069.
 - 32 J. Chen, W. Shi, Y. Jiang, D. Wang, Z. Shuai and S. Z. Strain, Strain induced polymorphism and band structure modulation in low-temperature 2,7-dioctyl[1]benzothieno[3,2-*b*][1]benzothiophene single crystal, *Sci. China: Chem.*, 2017, **60**, 275–283.



Supplementary information

Temperature-induced Polymorphism of a Benzothiophene Derivative: Reversibility and Impact on the Thin Film Morphology

Shunya Yan,^a Alba Cazorla,^a Adara Babuji,^a Eduardo Solano,^b

Christian Ruzié,^c Yves H. Geert,^{c,d} Carmen Ocal,^{*a} Esther Barrena^{*a}

^a Institut de Ciència de Materials de Barcelona (ICMAB-CSIC), 08193 Bellaterra, Barcelona, Spain

^b ALBA synchrotron, C/ de la Llum 2-26. Cerdanyola del Vallès, Barcelona, 08290, Spain

^c Laboratoire de Chimie des Polymères, Faculté des Sciences, Université Libre de Bruxelles (ULB), Boulevard du Triomphe, CP 206/01, 1050 Bruxelles, Belgium

^d International Solvay Institutes of Physics and Chemistry, Université Libre de Bruxelles (ULB), Boulevard du Triomphe, CP 231, 1050 Bruxelles, Belgium

Email: e.barrena@csic.es

Cell parameters calculation

In a monoclinic system, such as the ones observed for C₈O-BTBT-OC₈ thin-film, *c* parameter can be directly determined from the out-of-plane spacing and the angle between *c* and *a*-axis (β), as described by equation S1:

$$c = d_{001} / \sin \beta \quad (S1)$$

In general, for crystal structures with the (001) plane parallel to the substrate surface, in-plane and out-of-plane components of the reciprocal vector *q* can be written as equations S2 and S3, respectively:

$$q_{xy}^2 = q_x^2 + q_y^2 = h^2 z_a^2 + k^2 z_b^2 - 2hk z_a z_b \cos \gamma \quad (S2)$$

$$q_z = h\alpha^* \cos \beta^* + kb^* \cos \alpha^* + lc^* \quad (S3)$$

where $z_a = 2\pi / (a \sin \gamma)$ and $z_b = 2\pi / (b \sin \gamma)$, and a^* , b^* , c^* , α^* , β^* refer to reciprocal lattice parameters. Thus, from in-plane *q*-values (q_{xy}) the unit cell parameters *a*, *b*, and γ can be determined, while out-of-plane *q*-values (q_z) lead to parameters *c*, α , and β .¹

According to equation S2, the lattice parameter *b* can be extracted from the in-plane position of the (020) peak. If γ is assumed to be 90°, *b* parameter is given by equation S4:

$$b = \frac{4\pi}{q_{xy(020)}} \quad (S4)$$

Once the *b* parameter is calculated, the lattice parameter *a* can be extracted from the in-plane position of the (-1-20) peak, following the equation S5:

$$a = \frac{2\pi}{\sqrt{q_{xy(-1-20)}^2 - 4 \left(\frac{2\pi}{b}\right)^2}} \quad (S5)$$

Additionally, since we observe a third diffraction rod, we can verify the calculated unit cell parameters by comparing the expected position for (-1-10) with the observed position. The expected position for (-1-10) is given by equation S6:

$$q_{xy(-1-10)} = \sqrt{4\pi^2 \left(\frac{1}{a^2 \sin^2 \beta} + \frac{1}{b^2} \right)} \quad (S6)$$

For each lattice parameter we have considered the uncertainty given by the error propagation in the equation, considering the uncertainty of the peak position, i.e., the standard deviation given by the Gaussian fit for each peak.

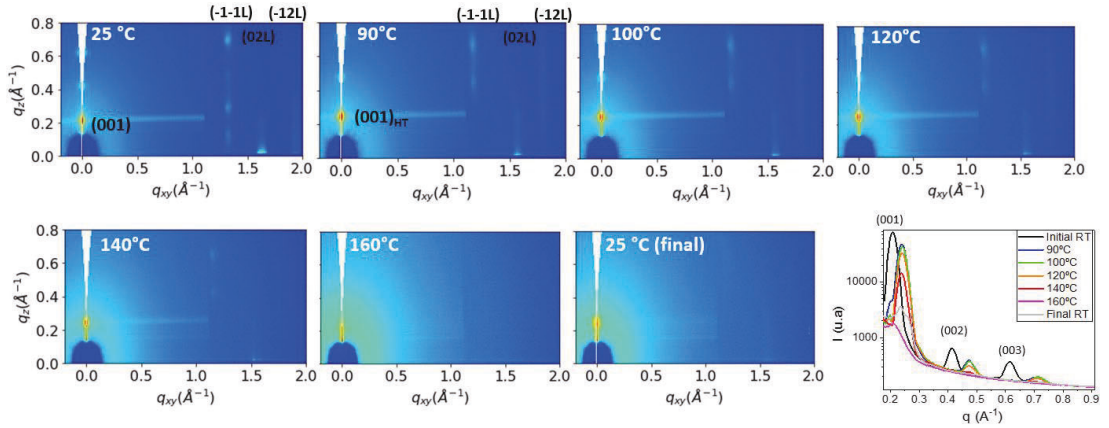
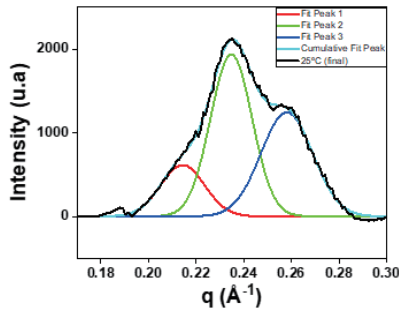


Figure S11. 2D GIWAXS patterns of a C₈O-BTBT-OC₈ thin film (incidence angle of 0.13°) acquired at each temperature. The horizontal line appearing $q_z \approx 0.24 \text{ \AA}^{-1}$ is a blooming effect from the CCD camera employed. Line cuts along the out-of-plane direction are plotted.



Model	Gauss		
Equation	$y=y_0 + (A/(w*\sqrt{\pi/2}))\exp(-2*((x-xc)/w)^2)$		
y0	3.60497 ± 5.09011	3.60497 ± 5.09011	3.60497 ± 5.09011
xc	0.21431 ± 0.00142	$0.23476 \pm 3.13516E-4$	$0.25808 \pm 6.0576E-4$
w	0.01849 ± 0.00159	$0.01749 \pm 8.51026E-4$	$0.02175 \pm 7.8747E-4$
A	14.19056 ± 2.22215	42.35017 ± 3.45375	33.84385 ± 1.80722
Reduced Chi-Sqr	1659.64057		
R-Square (COD)	0.99658		

Figure S12. Multiple peak Gaussian fit of the (001) peak from C₈O-BTBT-OC₈ films at 25 °C after post-annealing at 160 °C (grey spectrum in Figure 1b after background subtraction). The table corresponds to the results of the fits with Gaussian functions. The three peaks are centered at 0.214 \AA^{-1} , 0.235 \AA^{-1} and 0.258 \AA^{-1} .

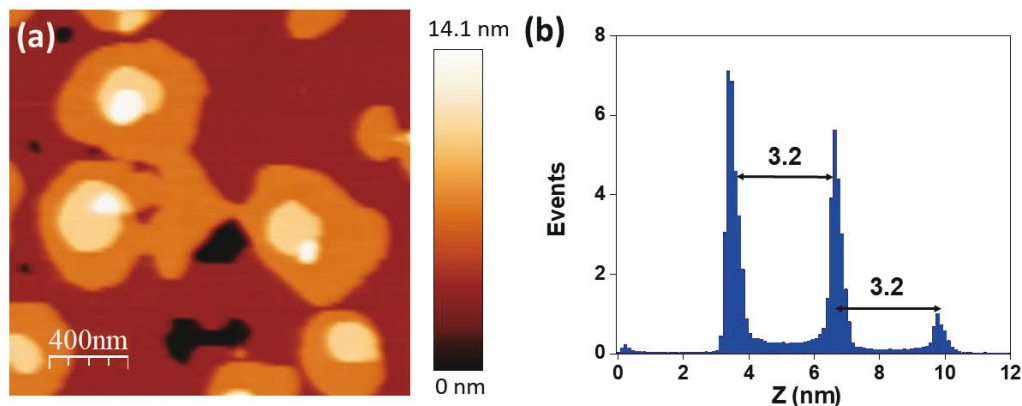


Figure S13. Topographic AFM image of the C_8O -BTBT- OC_8 film (nominal thickness of 14 nm) grown at RT (a). (b) Height distribution of the image in (a).

Figure S13a is the topography of a thin film of C_8O -BTBT- OC_8 with a nominal thickness of 14 nm, grown at 25 °C (room temperature). The film consists of 4 complete layers (each with single layer height) plus one nearly complete layer (large brown layer in the image) and islands with two or three layers. The height estimated from the histogram (Figure S13b) indicates that the molecules within the film are nearly perpendicular with respect to the silicon substrate, as corresponds to the SIP structure.

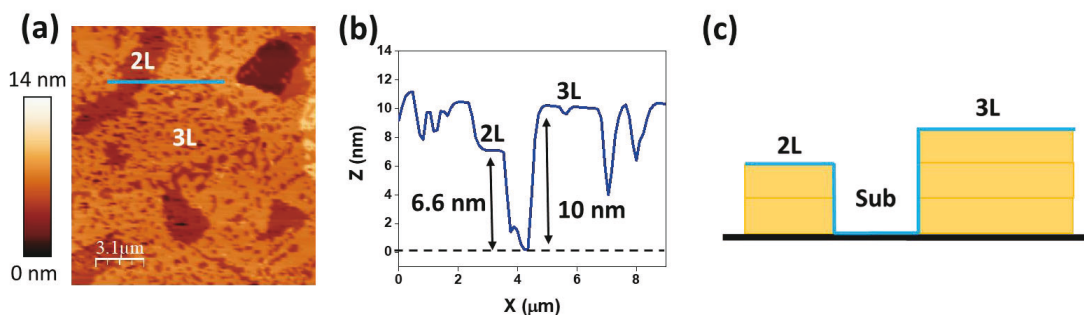


Figure S14. (a) Topographic AFM image of a C_8O -BTBT- OC_8 film (nominal thickness of 14 nm) grown at RT and cooled down to RT after post-annealing at 130 °C, (b) height profile corresponding to the blue segment in (a). The sketch in (c) illustrates schematically the height profile correspondence between height and number of layers indicated in (b).

As it can be seen from the topographic profile (blue line) in Figure S14b, reaching the substrate, the film consists of regions 2 and 3 layers thick.

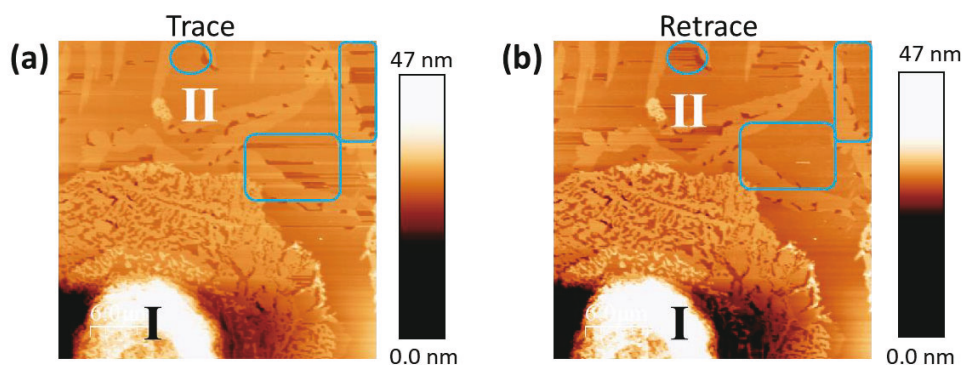


Figure S15. Trace (a) and retrace (b) topographic AFM images for a C_8O -BTBT- OC_8 film (nominal thickness of 14 nm) grown at RT and cooled down to RT after post-annealing at 150 °C. As it can be seen at the areas marked in blue, the lower layer is easily penetrated by the tip during scanning. The lateral size of the image is 30 μm x 30 μm .

In Figure S15 we show the trace and retrace images of the sample post-annealed at 150 °C. In region I (see detailed explanation in the main manuscript), the flat film of 2.5 nm thickness is easily damaged by tip scanning. In addition, some holes appear between the HTP and SIP structures arising from the different molecular density of these phases.

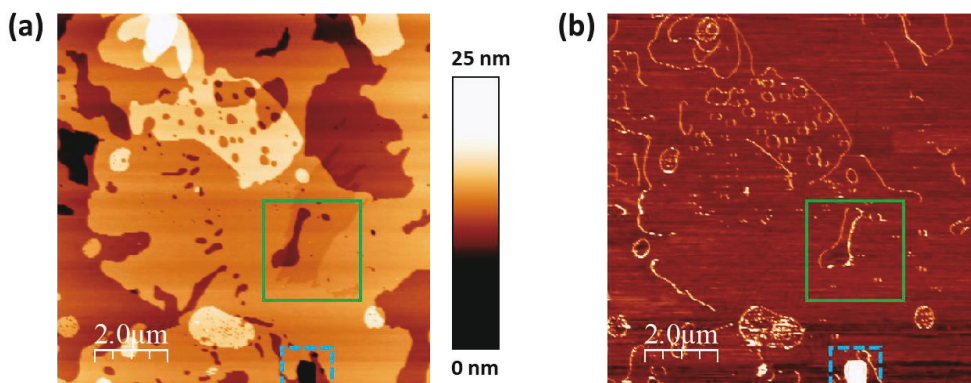


Figure S16. Topographic AFM image (a) and simultaneously obtained later force image (b) for a C_8O -BTBT- OC_8 film (nominal thickness of 14 nm) grown at 130 °C. The area marked by green and dashed blue squares correspond to Fig.6c and a hole reaching down the substrate, respectively.

Figure S16 is a larger image of the region imaged in Figure 6c of the main manuscript. It is clearly seen that the low 0.6 nm steps do not show any contrast in the lateral force (LF) image. Some other regions with similar steps can be identified, this fact demonstrates that, upon cooling at RT after the post-annealing treatment, some regions remain in the HTP structure while other regions convert to the most stable SIP at RT.

- [1] J. Simbrunner, C. Simbrunner, B. Schrode, C. Röthel, N. Bedoya-Martinez, I. Salzmann and R. Resel, Indexing of grazing-incidence X-ray diffraction patterns: The case of fibre-textured thin films, *Acta Crystallogr. Sect. A Found. Adv.*, 2018, **74**, 373–387.

PAPER II

*Polar polymorphism: a new intermediate structure towards
the thin-film phase in asymmetric benzothieno[3,2-b][1]-
benzothiophene derivatives*

Polar Polymorphism: A New Intermediate Structure toward the Thin-Film Phase in Asymmetric Benzothieno[3,2-*b*][1]-benzothiophene Derivatives

Shunya Yan, David Cornil, Jérôme Cornil, David Beljonne, Rogger Palacios-Rivera, Carmen Ocal,* and Esther Barrena*

Cite This: *Chem. Mater.* 2024, 36, 585–595

Read Online

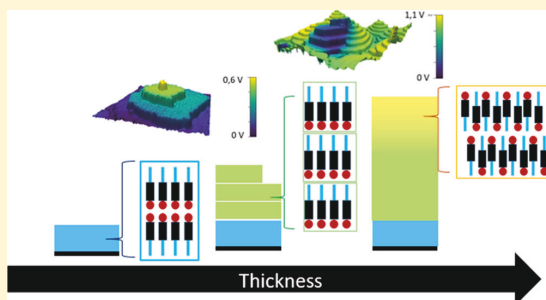
ACCESS |

Metrics & More

Article Recommendations

Supporting Information

ABSTRACT: Understanding structure and polymorphism is relevant for any organic device optimization, and it is of particular relevance in 7-decyl-2-phenyl[1]benzothieno[3,2-*b*][1]-benzothiophene (Ph-BTBT-10) since high carrier mobility in Ph-BTBT-10 thin films has been linked to the structural transformation from the metastable thin-film phase to the thermodynamically stable bilayer structure via thermal annealing. We combine here a systematic nanoscale morphological analysis with local Kelvin probe force microscopy (KPFM) that demonstrates the formation of a polar polymorph in thin films as an intermediate structure for thicknesses lower than 20 nm. The polar structure develops with thickness a variable amount of structural defects in the form of individual flipped molecules (point defects) or sizable polar domains, and evolves toward the reported nonpolar thin-film phase. The direct experimental evidence is supported by electronic structure density functional theory calculations. The structure of the film has dramatic effects on the electronic properties, leading to a decrease in the film work function (by up to 1 eV) and a considerable broadening of the occupied molecular orbitals, attributed to electrostatic disorder. From an advanced characterization point of view, KPFM stands out as a valuable tool for evaluating electrostatic disorder and the conceivable emergence of polar polymorphs in organic thin films. The emergence of polar assemblies introduces a critical consideration for other asymmetric BTBT derivatives, which may be pivotal to understanding the structure–property relationships in organic field-effect transistors (OFETs). A precise determination of any polar assemblies close to the dielectric interface is critical for the judicious design and upgrading of high-performance OFETs.



INTRODUCTION

In recent years, significant progress has been made in the development of novel π -conjugated organic materials used as active layer in high-performance organic electronic devices.^{1–4} Heteroarenes with fused aromatic rings, such as [1]-benzothieno[3,2-*b*]benzothiophene (BTBT) derivatives, qualify among the best-performing organic semiconductors for field-effect transistors (OFETs) with a charge carrier mobility over $10 \text{ cm}^2 \text{ s}^{-1} \text{ V}^{-1}$ and excellent air stability.^{5–7} Further applications extend to photodetectors/phototransistors or to their use as donors to form organic charge-transfer (CT) complexes.^{5,6} Furthermore, the high designability of BTBT derivatives has enabled the formation of a variety of symmetric and/or asymmetric alkylated BTBT molecular structures.^{8–13}

Besides their role in enhancing molecular solubility, long alkyl chain side groups serve to improve the intermolecular packing, leading to a lamella-like structure (where the interlayer distance correlates with the length of the molecule) and a herringbone (HB) arrangement of the π -cores that allows for efficient π – π overlap between adjacent molecules.

Indeed, the excellent charge transport properties of OFETs based on thin films of dialkyl BTBT derivatives can be attributed to the layered crystalline structure consisting of an alternating stack of alkyl chain and BTBT core layers.⁵ Furthermore, the synthesis of asymmetric BTBT derivatives with nonidentical side groups, has prompted a large number of studies because they offer greatly improved thermal stability and liquid crystalline (LC) phases that can be used to engineer the morphology of the films.^{10,14–17,19} While van der Waals forces are the dominant interactions between nonpolar molecules, dipolar electrostatic interactions also come into

Received: November 16, 2023

Revised: December 11, 2023

Accepted: December 11, 2023

Published: December 26, 2023



play for building blocks with an unbalanced distribution of the electronic density.

In particular, the monoalkylated 7-decyl-2-phenyl[1]-benzothieno [3,2-*b*][1]benzothiophene (Ph-BTBT-10) is a fascinating BTBT derivative that has gained significant attention due to its excellent high carrier mobility in p-type OFETs.^{10,14,18} LC phases emerging at higher temperatures ($T > 145$ °C)^{23–25} can be exploited for morphological and structural control. A key to the high performance of Ph-BTBT-10 in OFETs is the bilayer arrangement. As determined by single-crystal X-ray diffraction (XRD),²⁶ in the bilayer structure the Ph-BTBT-10 molecules stack on top of each other in a head-to-head (or tail-to-tail) fashion, resulting in a stacking periodicity of $d_{\text{BL}} = 5.30$ nm, i.e., twice the molecular length (Figure 1).^{23–26} The molecules are unidirectionally

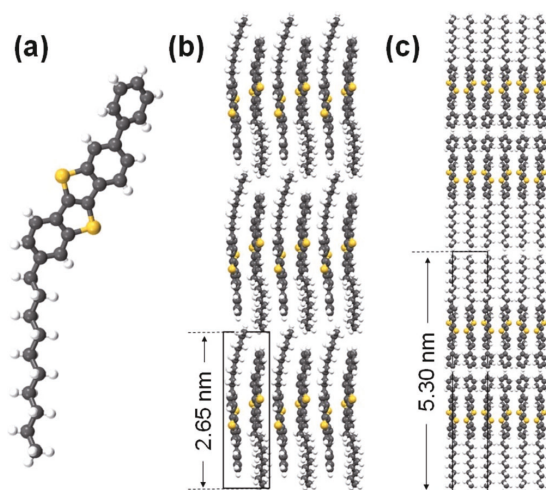


Figure 1. (a) Molecular structure of Ph-BTBT-10. (b) Thin-film polymorph consisting of a stack of single layers with antiparallel orientation of the molecules.²⁵ (c) Bilayer (BL) lamellar packing consisting of a stack of double layers, where the molecules have a unidirectional orientation within each layer but are arranged antiparallel to the molecules in the adjacent layer.²⁵ The corresponding stacking periodicities are indicated.

oriented within each half-bilayer, with the BTBT cores adopting an in-plane HB organization similar to that for symmetric derivatives. As a result of the asymmetric nature of the Ph-BTBT-10 and the associated electrical dipole, each half-bilayer is polar, whereas the entire BL is nonpolar. The HB packing of the molecular π -cores favors the two-dimensional transport and affords high carrier mobility.^{14,26,27}

During thin-film growth, the development of metastable crystalline structures that differ from the bulk structures is a widespread phenomenon in organic materials,²⁸ that also takes place in Ph-BTBT-10. Unlike single crystals, for films grown at room temperature (RT), the molecules have been found to adopt a layered structure with an interlayer spacing of $d_{\text{TF}} = 2.65$ nm, i.e., corresponding to a packing of single molecular layers (SL) and referred to as a thin-film phase. The high carrier mobility in OFETs based on Ph-BTBT-10 thin films has been linked to the structural transformation from the metastable thin-film phase to the thermodynamically stable BL stacking via thermal annealing at $T > 110$ °C, rendering

approximately ten times larger mobility.¹⁴ The formation of SL and BL structures as well as the structural transition between them by thermal annealing has also been found for other monoalkylated BTBT derivatives^{11,15,29–34} and other asymmetric materials,^{35,36} suggesting that they are common among asymmetric molecules.

The molecular packing in the thin-film structure was under debate until the structure was finally determined by wide-angle X-ray scattering in a study carried out on 60 nm-thick films.²¹ The reported structure is presented in Figure 1b. Molecules in the thin-film polymorph maintain a HB arrangement of the conjugated units and are packed with a slightly offset antiparallel orientation within each layer. The antiparallel orientation of the molecules in the plane yields a nonpolar layer as does the entire bilayer. As can be inferred from the structural models, the alignment of the BTBT cores in the BL (Figure 1c) favors a better overlap of the π -molecular orbitals than for the shifted antiparallel arrangement of the molecules in the thin-film phase (Figure 1b).

Given that the carrier mobility of the films is crucially dependent on the formed polymorph, many studies have focused on establishing strategies to control it via growth and thermal treatments, including recrystallization from the smectic phase, and in gaining a deep understanding of the molecular processes underlying the temperature-induced structural transformations.^{10,14,22,37–41} Still a complete perception of the effect of the substrate interface on the origin and variation of polymorphic phases has not yet been obtained. It remains unexplored how the electronic properties of thin films are affected by structural changes.

We combine here a systematic nanoscale morphological analysis with local Kelvin probe force microscopy (KPFM) that demonstrates the formation of single layers during the first stages of the growth (for thicknesses lower than 20 nm), which develop as an intermediate structure toward the thin-film phase as thickness increases. The experimental evidence is supported by electronic structure density functional theory (DFT) calculations, highlighting the effects of polar polymorphism on the electronic properties of the films. The thickness dependence of the reported polar structure and the potential coexistence of diverse polymorphs represent other key factors to be considered for controlling the efficiency and functionality of organic devices.

RESULTS

Low Coverage: Demonstration of Polar Assemblies.

Throughout this work, we establish the correlation between organic film topography and surface potential (SP) obtained by KPFM. The SP map provides a measure of spatial variation of the sample work function. For the setup employed here (see Experiments and Methods section), regions with a more positive value of SP correspond to a lower value of the work function; in other words, to a downshift of the vacuum level (E_{vac}). We report here common characteristics derived from a systematic investigation performed for Ph-BTBT-10 films (Figure 1a) deposited from the vapor phase onto the native oxide surface of Si(100) substrates, under high vacuum conditions (10^{-7} mbar) and at different substrate temperatures below the transition from thin film to BL structure, ranging from 25 to 90 °C. Although the conclusions are common to the entire series of samples studied, some of the selected images correspond to growths at 80 and 90 °C, since a higher substrate temperature favors the formation of larger terraces

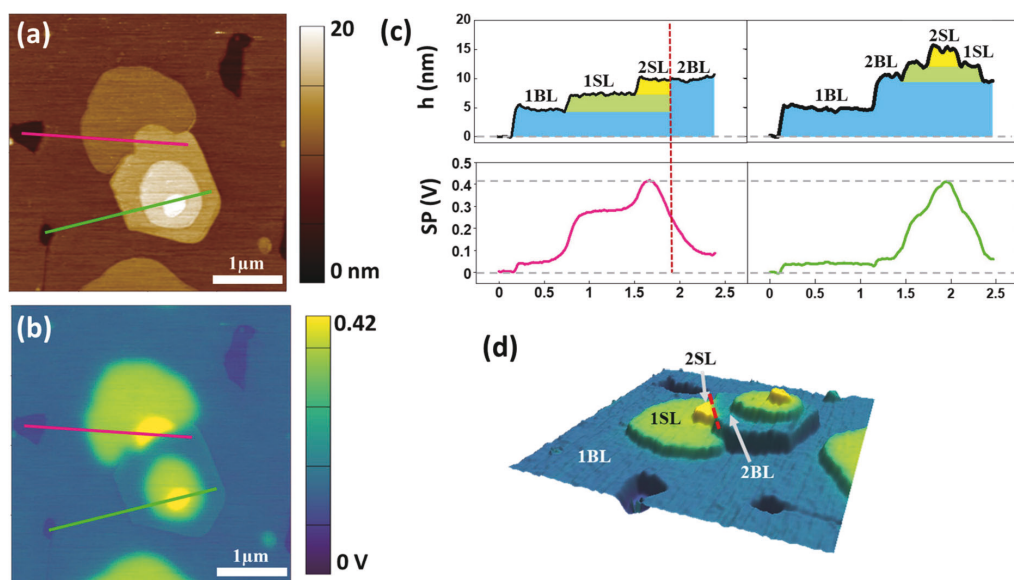


Figure 2. (a) Topographic image and (b) the corresponding surface potential map (raw data) for a nominal thickness of ≈ 5 nm of Ph-BTBT-10 deposited under UHV on the native oxide of a Si(100) substrate kept at 90 °C. (c) Line profiles obtained along the segments indicated in the corresponding topographic and SP images. For a clearer interpretation, the substrate level has been taken in the profiles as $h = 0$ and $SP_{\text{Sub}} = 0$. (d) Three-dimensional visualization of the merged topographic and SP data.

and, consequently, a better discrimination of the local SP (Figure S1).

The first stages of the Ph-BTBT-10 growth are analyzed first. The amount of molecules deposited is given as the nominal thickness in nanometers (see Experiments and Methods section). Typical topographic and KPFM data obtained for a nominal thickness of ≈ 5 nm are shown in Figure 2. The observed surface morphology (Figure 2a), where only a few regions of the substrate (black) remain uncovered, confirms the formation of a nearly continuous molecular film with a thickness of ≈ 5 nm (dark brown). This observation is in agreement with the formation of a Ph-BTBT-10 bilayer in direct contact with the substrate,²¹ where molecules within each single layer are unidirectionally oriented but arranged antiparallel in one single layer with respect to the other. On top of the first bilayer (1BL), extremely flat stacked terraces indicate a crystalline layered growth. The line profile shown in the top right of Figure 2c, corresponding to the magenta segment in (a), indicates that on top of 1BL, there are two terraces with a step height of $2.65 \text{ nm} \pm 0.05 \text{ nm}$. Given that, on average, the measured step height equals the molecular length of Ph-BTBT-10 (see Figure 1), each of such terraces is unambiguously ascribed to a single-molecule thick layer (1SL and 2SL). On the other hand, along the green profile in the top left of Figure 2c, one can see a terrace with bilayer thickness (marked as 2BL) followed by two more single layers. However, the most striking features are extracted from the SP maps. Outstandingly, BLs and SLs are clearly distinguished in the SP map (see Figure 2b and lower panels of Figure 2c). For simplicity, we assign the substrate as reference for SP ($SP_{\text{Sub}} = 0$ at the regions of the uncovered substrate). Note that BL regions exhibit the same value of SP, only differing by $\approx 0.05 \text{ V}$ from SP_{Sub} , i.e., stacked bilayers do not lead to potential buildup (see Figure 2b,c). Indeed, no surface dipole is

expected for a stack of bilayers due to the nonpolar character of each BL and the absence of charge transfer between the substrate and the film (i.e., condition of vacuum level alignment). The same argument would apply for the stacking of nonpolar layers in the thin-film structure (Figure 1b). It is conversely observed in Figure 2c that the formation of 1SL leads to an increase of SP by $\approx +0.25 \text{ V}$, indicating a net dipole in the SL configuration. As can be seen in the profiles at the bottom of Figure 2c, this quantitative effect is independent of the number of bilayers underneath, indicating that it is an intrinsic characteristic of the specific molecular arrangement within the SL. To facilitate visualization of the described effect, Figure 2d presents the 3D construction resulting from the superimposition of the SP data (color scale) to the topographic image. In summary, while SP remains constant regardless of the number of stacked BLs, SP becomes more positive and increases stepwise with the number of piled SLs. We note that this increase corresponds to a decrease in the local work function. Although from a morphological point of view, the stacking of an even number of SLs is indistinguishable from a stacking of BLs, the SP measurement provides a means of distinguishing the two types of crystalline structures. Very clarifying is the examination of the domain boundary between the two types of stacks signaled by a red dotted line in Figure 2c,d. While the domain boundary is clearly identified in the SP data, both domains are not distinguished in the topographic ones.

As mentioned above, the net electrical dipole observed for each SL is incongruent with the antiparallel orientation of molecules in the layer structure proposed for the thin-film phase determined for 60 nm-thick films.²⁵ Conversely, the results obtained here for considerably thinner films are consistent with an assembly of unidirectionally oriented (polar) molecules in each SL. The positive accumulation of

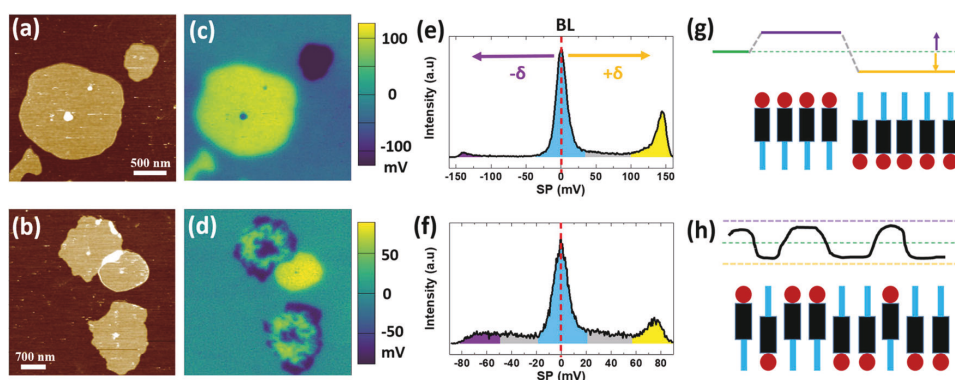


Figure 3. Topographic images (a,b) with the corresponding surface potential (SP) maps (c) and (d). Total z range in (a) is 8.5 nm (from the darkest to the brightest color). The histograms of each SP map are depicted in (e) and (f), respectively. In this case, in the absence of uncovered substrate, $SP = 0$ corresponds to the bilayer in contact with the substrate (1BL). The nominal thickness of Ph-BTBT-10 deposited is ≈ 6 nm. Illustrative diagrams of the vacuum level for single-molecule thick islands with unidirectional orientation (up or down) (g) and a mixed orientation (up and down) (h) of the molecules.

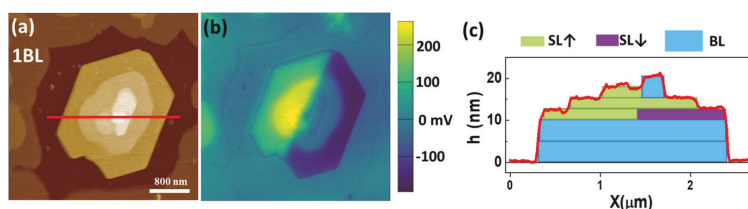


Figure 4. (a) Topographic image and (b) the corresponding surface potential (SP) for a nominal thickness of ≈ 5 nm of Ph-BTBT-10 deposited at 90°C . (c) Line profile along the segment indicated in (a). The molecular packing of the different layers under the profile is represented by the respective colors, where SL \uparrow and SL \downarrow indicate the direction of the alkyl chain.

SP points unequivocally to the fact that the molecules of each of all stacked SLs are oriented with the alkyl chains facing up (see calculations below). In other words, the observed stacking consists of single molecular layers with the same molecular dipole orientation, such that their dipoles add up.

Although most of the observed SLs exhibit a positive SP, indicating that the chain-up configuration is the most frequent assembly, single layers with opposite electrical dipole orientations (chain-down) as well as layers with coexisting small domains (chain-up and chain-down) were also found. Figure 3 illustrates this observation for a nominal thickness of ≈ 6 nm. Topographic images (Figure 3a,b) were taken on two surface regions of the same sample that show several molecular islands with a rather rounded shape and identical height (≈ 2.7 nm) nucleated on top of the bilayer in contact with the substrate. We first analyze the SP map in Figure 3c, which shows that each individual island in Figure 3a exhibits a homogeneous SP value, but opposite sign to one another (yellow or dark blue on the color scale). That is, the molecular arrangement within each island causes an increase/decrease in the local SP by the same amount ($\delta = \pm 0.15$ eV) with respect to the underlying nonpolar BL (see the histogram in Figure 3e). Note that in this case, where no substrate is seen in the imaged area, the reference for SP has been taken at 1BL (blue peak in the histogram) while chain-up and chain-down islands lead to positive (yellow peak) and negative (purple peak) values, respectively. Each of the described islands is a single domain, indicating complete lateral phase separation of polarities in this case. The lower value of the SP change in

this case (<0.2 V) may indicate some structural variability in the form of a certain amount of flipped molecules in the packing. Indeed, as illustrated in Figure 3b–d, lateral phase separation can occur in a much shorter range, giving rise to local electrostatic disorder. Next to the single domain circular island, two other islands do present an irregular shape and inhomogeneous SP. This observation reflects the coexistence of short-range assemblies down to the nanometer size with chain-down or chain-up molecules.

The formation of laterally separated chain-up and chain-down domains gives rise to SP maps with features that appear uncorrelated with the surface morphology. We will return to this fact, but an attractive example of this scenario is shown in Figure 4. The electrostatic potential map of the crystallite at the center of the image is explained by the presence of a single molecular layer intercalated within the film with a domain boundary separating domains with chain-up and chain-down orientations. Subsequent polar layers (all chain-up molecules) grown on top of the stacking fault lead to such an asymmetric SP distribution. The proposed stacking scheme is provided with the line profile in Figure 4c. The selected example also illustrates that the nucleation of a BL at the mound top does not result in any modification of SP, i.e., the BL is nonpolar and does not contribute to SP.

Evolution with Thickness: Molecular Flipping. The specular XRD spectra obtained for 15 and 40 nm-thick films (Figure 5a) show well-defined Bragg peaks at $q_z = 0.235 \text{ \AA}^{-1}$ corresponding to a spacing of 2.675 nm, confirming a layered packing with one single-layer periodicity. GIWAXS data

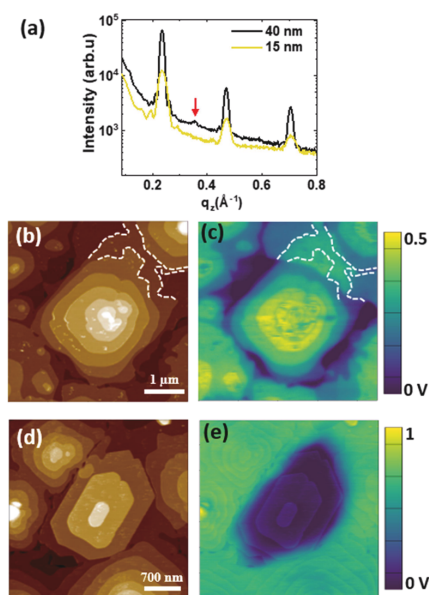


Figure 5. (a) Specular XRD spectra obtained for 15 and 40 nm-thick films. Topographic images of Ph-BTBT-10 films of the nominal thickness of 15 nm (b) and 40 nm (d). The SP maps simultaneously collected are displayed in (c) and (e), respectively. Some step profiles have been marked by dashed white lines in (b) and (c) to highlight a lack of correlation with the local SP in this region (see text).

confirm the characteristic pattern of the HB BTBT packing (Figure S2). The small-intensity peak at $q_z = 0.354 \text{ \AA}^{-1}$ (signaled by a red arrow) corresponds to the (003) Bragg peak of the bilayer lamellar structure ($d_{\text{BL}} = 5.32 \text{ nm}$), confirming the formation of a small fraction of the crystalline BL bulk structure. Representative topographic data of Ph-BTBT-10 films of the nominal thickness of 15 and 40 nm are displayed in Figure 5b,d, respectively, along with the corresponding SP maps (c and e). In both cases, terraced mounds are observed, most of them corresponding to SL stacks in agreement with the XRD data. Interestingly though, the mound at the center of Figure 5d exhibits terraces with straight edges all separated by steps with a height of $\approx 5 \text{ nm}$ (two molecular layers) and is therefore associated with the growth of a BL-crystallite. The presence of laterally segregated BL crystallites in the film is not rare (Figures S3 and S4), being responsible of the small fraction of crystalline BL observed by XRD (red arrow in Figure 5a). At this point, it is worth highlighting some interesting observations. As seen by the color scales in the KPFE maps, while SP increases with the number of SL in all visible mounds for the 15 nm-thick film (Figure 5c), for the 40 nm-thick film, SP is constant regardless of the number of SLs in the various mounds (lighter region in Figure 5e). We also note that the SP map in Figure 5c includes domains with different SP at the same terrace level (delimited by white dashed lines in Figure 5b,c). This fact arises from domain boundaries in buried layers that were formed during early growth stages, which might be due to SLs formed by domains of opposite polarity, as described before. Further examples of areas where the SP is uncorrelated with the morphology are given in the Figure S4.

Modeling and DFT Calculations. We use periodic DFT electronic structure calculations (see details in Experiments and Methods section) to model changes in the electrostatic potential of a perfect polar molecular layer, i.e., unidirectional orientation of the molecules, and in the presence of molecular disorder implemented by flipped molecules. The polar models were built from the smectic phase reported by Hofer et al. (Figure S5a),²¹ considering two possible dipole orientations. From now on, “up” and “down” configurations refer to the orientation outward and inward, respectively, of the alkyl chains of the Ph-BTBT-10 with respect to the substrate. The lattice vectors of the unit cell were increased by two along the in-plane directions to generate a supercell with an area of $(12.1 \text{ \AA} \times 16.6 \text{ \AA})$ containing 8 BTBT molecules (25.1 \AA^2 per molecule, i.e., a full density packing). On that basis, we have considered a single molecular layer with several ratios of down:up molecules to mimic molecular defects in the form of molecular flipping, between the two limiting cases (100% “up” and 100% “down”), see Figure 6a. The averaged electrostatic energy was computed perpendicular to the film, taking into account the potential difference between the top and bottom film planes. The change in electrostatic energy corresponds to the shift in the vacuum level (i.e., work function change), which corresponds to an opposite shift in the SP observed by KPFE.

The calculations in Figure 6a show a linear evolution of the vacuum level shift when continuously changing randomly the relative ratio of the up and down configurations. For single monolayers in a pure-down configuration (down:up 100%), the change in the electrostatic energy is $+0.264 \text{ eV}$, whereas switching the orientation of all molecular dipoles to a pure-up configuration (down:up 0%) results in a downshift of the vacuum level by -0.273 eV . Thus, the similar but opposite increase/decrease in the SP shift observed in some regions (Figure 3a–c) is explained by the formation of domains, each one made up of molecules adopting one of the two possible polar orientations. The dipole cancellation is almost perfect for a down:up ratio 1:1 (electrostatic energy $\approx -0.004 \text{ eV}$), corresponding to an antiparallel (mixed) configuration. As shown in Figure S5c, a polar single layer on top of a 1:1 mixed monolayer gives a similar shift as a polar free-standing single layer, thus implying a negligible role of depolarization. Similarly, no significant depolarization effect exists for a stacking of multiple layers, with the dipoles either adding up or canceling each other depending on their relative orientations (see Figure S5c). In particular, when all superimposed layers have the molecular dipoles aligned in the same direction, the total energy shift is virtually a multiple of the shift obtained for a single dipolar layer. Experimentally, this was not observed. The change in SP for a typical mound of packed SLs (Figure 6b) has been quantified and plotted in Figure 6c. The SP values measured at each terrace are depicted as a function of the number of SLs on top of the BL that is taken as a reference ($\text{SP}_{\text{BL}} = 0$). We first note that the SP value measured for the first SL on top of the BL is fully consistent with the expected downshift of the vacuum level from a pure-up configuration (down:up 0%). Remarkably, the experimental SP increases with the number of piled SLs until it saturates for ≈ 5 –6 layers. Taking into account the thickness of the underlying bilayer at the substrate interface, the nominal thickness of the film with saturated SP is approximately $\approx 20 \text{ nm}$.

The measured nonlinear increase and saturation of SP is explained by a progressive increase in the amount of flipped

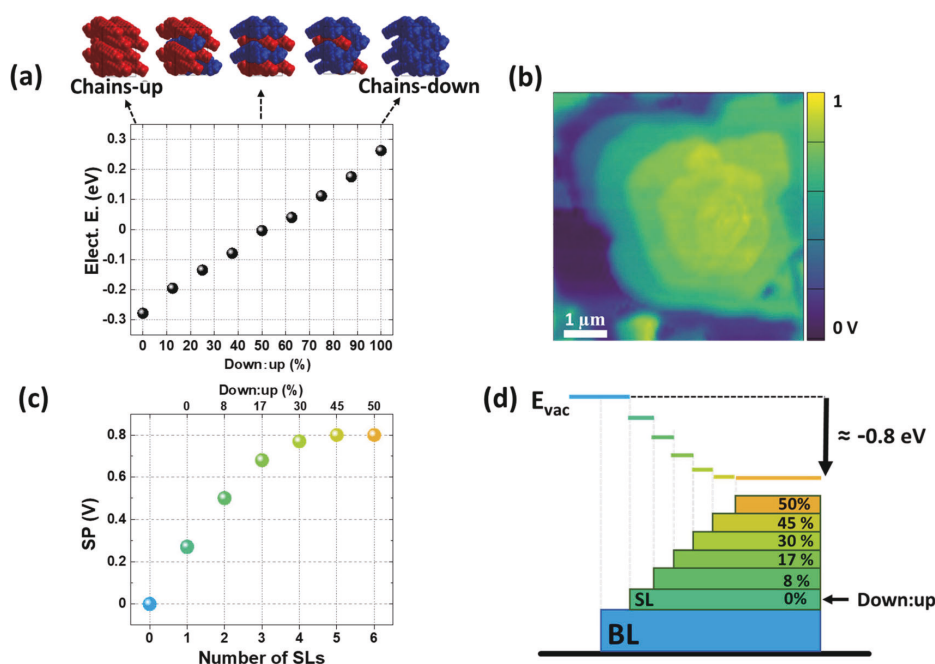


Figure 6. (a) DFT electron structure calculations: Electrostatic energy (vacuum level shift) calculated for a single monolayer as a function of the ratio between the two possible molecular orientations within the SL, i.e., chain-up (up) and chain-down (down). (b) KPFM map of a typical mound of stacked SLs. (c) Left axis: Experimental SP obtained from (b) as a function of the number of SL on top of the bottom bilayer, which is taken as the reference ($SP_{BL} = 0$). Top axis: percentage of down:up molecules for the diverse SLs estimated from (a) and the experimental difference in the SP by each added layer. (d) Illustrative cartoon indicating the percentage of down:up molecules in each layer and the effect on the vacuum level. The same color scale is used in all panels.

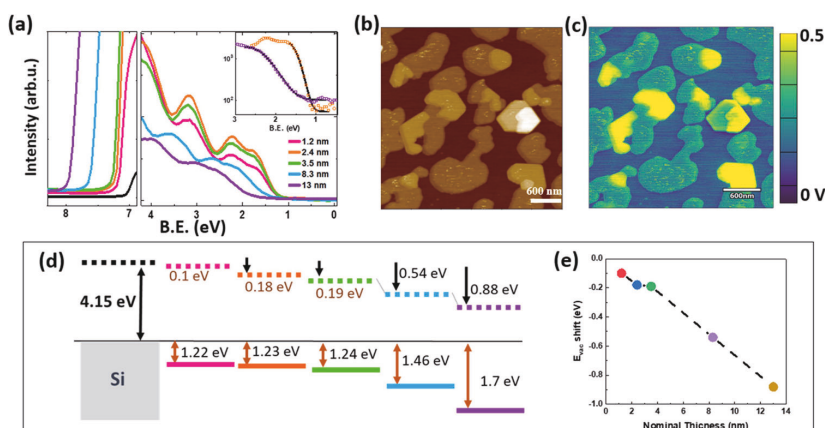


Figure 7. (a) In situ UPS measured for different amounts of Ph-BTBT-10 (nominal thickness indicated in nm) deposited at RT; SECO and valence band regions are depicted. (b) Topography and (c) surface potential map for a Ph-BTBT-10 nominal thickness of x nm deposited at RT. Under these conditions, islands of an incomplete BL leave uncovered substrate areas, while SL terraces form on top of the BL islands. Schematic illustration of the energy levels (d) and plot of the vacuum level shift (e) as a function of thickness, extracted from data in (a).

molecules as the layer number increases. From Figure 6a, we estimate the percentage of down:up molecules that corresponds to the measured SP shift for each added SL (see also Figure S6). These estimations are given in the top axis of Figure 6c and the percentage of flipped molecules is indicated in the illustrative cartoon of Figure 6d. In such a scenario, from the parallel orientation (down:up 0%) in the first layer, a rising

number of down-chain molecules is formed within each subsequent layer until, eventually, half of the molecules are arranged in an antiparallel fashion forming a mixed nonpolar SL (top center, Figure 6a). Hence, the thin-film phase reported for 60 nm-thick films (Figure 1b) is the nonpolar structure achieved, as the films thicken. Although the plot in Figure 6c has been measured in one particular mound, it represents the

general behavior. Nevertheless, the SP saturation value may differ for different regions (between 0.8 and 1.1 V) due to differences in local crystalline quality (as demonstrated in Figures 3–5).

It is worth noting that from an energetic point of view, the unidirectional alignment of dipoles is unfavorable by +0.35–0.40 eV compared to the nonpolar antiparallel configuration (more stable). As we discussed later, its formation during growth can be considered a kinetically trapped surface-induced structure.

Electronic Effects: Molecular Orbitals, Ionization Potential, and Vacuum Level. As we will see next, the local electrostatic potential data are key for a comprehensive understanding of the electronic density of states, as measured by UPS and the influence of thickness on the electronic properties of Ph-BTBT-10 films.

Figure 7 shows the UPS spectra obtained for different stages of the growth of Ph-BTBT-10 at RT. In particular, the corresponding secondary electron cutoff (SECO) and the highest occupied molecular orbital (HOMO) regions of the valence band (VB) are shown in Figure 7a. It is worth noting that during Ph-BTBT-10 growth at RT, nucleation of single molecular layers takes place on pre-existing BL islands before its completion (Figure 7b). Therefore, at the early stages of growth, the surface dipole of these nucleated SL terraces contributes to the surface-averaged SECO that results in a larger value than expected for a complete nonpolar BL. Up to a nominal thickness of 3.5 nm, there is no measurable alteration in the HOMO position and the SECO points to a condition of vacuum level alignment. Indeed, given that the Fermi level of the substrate is located within the gap of the OSC, charge transfer is not expected. As the thickness increases, a shift in the vacuum level (E_{vac}) is accompanied by a shift to the higher binding energy of the HOMO and a visible broadening. For a deposition of 13 nm, a considerable decrease of the E_{vac} by 0.9 eV is obtained. Note that the saturation of the E_{vac} , which is expected for a thickness of ≈ 20 nm, has not yet been reached; the 13 nm-thick film here can be considered a defective polar film. Figure 7d summarizes the evolution of both HOMO and E_{vac} with thickness. From the energy difference between HOMO and the SECO onset, a remarkable decrease in IP is estimated, from 5.27 to 4.97 eV for the total range of thickness studied. Although the HOMO onset region is well fitted with a Gaussian curve, indicating that there are no appreciable gap states, a clear broadening is observed. This is illustrated by the magnification of the frontier orbital region (inset Figure 7a) for nominal thickness of 2.4 and 13 nm, in which the corresponding fits (solid black lines) indicate a considerable broadening, with a change of the full width half-maximum (fwhm) of the Gaussian from 0.47 to 1.04 eV.

DISCUSSION

An outstanding observation previously reported²¹ and confirmed by this work is the formation of one bilayer (structural out-of-plane unit of the bulk phase) of Ph-BTBT-10 at the interface with the substrate. The almost negligible contribution to SP of the BL with respect to the substrate agrees with the zero net electrical dipole of this structure, where the opposite dipoles of each half-bilayer are canceled out. However, to the best of our knowledge, a demonstration that the lamellar stacking of individual molecular layers on top of this BL can be different from the established thin-film structure has not been reported so far. We have shown here the

appearance of polar single layers akin to one-half-bilayer. Outstandingly, the unidirectional packing of molecules maximizes the interchain van der Waals interactions and enhances herewith the packing of the BTBT cores²⁶ but, in terms of dipolar interactions, results in a considerable electrostatic energy cost. We hypothesize that the formation of the bottom BL templates the nucleation and growth of molecules with half-bilayer (unidirectional) packing. From this point of view, the reported polar polymorph is a surface-induced metastable structure that will be transformed into the bilayer crystalline structure (thermodynamically stable) upon thermal annealing. Although the alkyl-up configuration is favored, domains with the opposite orientation are also found. DFT calculations of the electrostatic potential yield a downshift of the E_{vac} by -0.273 eV (i.e., a positive shift of the SP) for a defect-free dipolar layer with chain-up orientation, which is in excellent agreement with the experimental value measured by KPFM for the first SL on top of the BL. The calculations also indicate that depolarization effects are negligible, so that a stacking of dipolar planes causes a net dipole moment perpendicular to the surface equal to the sum of each plane. Experimentally, the local SP shift measured as a function of the increasing number of stacked single layers does not escalate linearly but reaches a saturation value close to 1.0 V upon 5–6 layers. The observed changes in the SP can be adequately explained by the increasing proportion of flipped molecules within the stacked layers. As the film thickens, the assembly of alternating chain-up and chain-down molecules plus structural relaxation eventually leads to the nonpolar (1:1) thin-film structure.

The overall scenario is illustrated in Figure 8. The structural evolution with thickness can be rationalized by simple

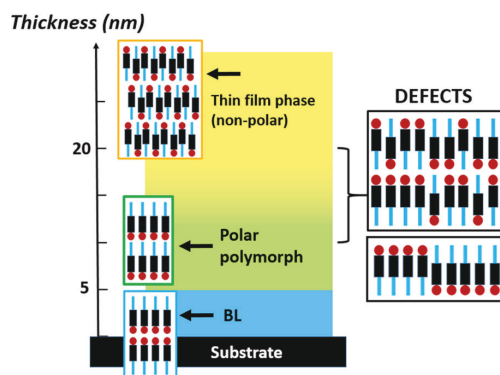


Figure 8. Cartoon illustrating the structural arrangement of Ph-BTBT-10 molecules during growth on a silicon substrate as a function of film thickness.

electrostatic arguments. It is known that whenever there is a dipole moment in the repeating structural unit perpendicular to the surface, the surface energy diverges, meaning that the polar surface becomes unstable with crystal thickness along the polar crystallographic direction. This is the so-called “polar catastrophe”.^{42,43} For ionic crystals, there are several “polarity compensation mechanisms” to overcome undesired instability. In our case, inclusion of flipped molecules in the packing during the growth can be seen as a mechanism for electrostatic compensation, avoiding the “polar catastrophe” as the number of layers stacked increases.

Comprehending the impact that such thickness-dependent polymorphism has on the HOMO density of states in thin films holds significant importance due to its profound influence on gap states and energy alignment and, herewith, with important implications for the performance of devices. Indeed, the UPS study as a function of thickness reveals a rigid shift of the energy levels and hence a decrease in the overall work function, confirming the KPFM results and the effect of the net electrical dipole. Localized defects in the form of flipped molecules or grain boundaries amid opposing polar domains introduce energy differences among molecular sites, i.e., static disorder. Although the impact that extrinsic static disorder has in the electronic properties of organic semiconductors (by producing gap states) has been demonstrated,^{44–46} here we provide direct evidence of the dramatic consequences of structural imperfections related to the polar character of the asymmetric BTBT molecule. Hence, for Ph-BTBT-10 thin films, the predominant source of energetic disorder is electrostatic in nature, stemming from the inherent electrical dipole of the molecule and causing a considerable broadening of the HOMO (here from 0.47 to 1.04 eV) as the film thickens. KPFM has been demonstrated to be an essential tool to identify the nature and spatial distribution of electrostatic defects in the film. In addition to structural defects in the form of individual flipped molecules (point defects), the formation of sizable domains, i.e., separated assemblies of one or the other possible polar orientations leads to heterogeneities in the electrostatic potential either in the form of islands (Figure 3c) or in small lateral scales (Figure 3d). Interestingly, in the case of buried (intercalated) domain boundaries, intriguing SP maps that appear uncorrelated to the morphology can be found (Figures 4 and 5). Furthermore, from combined KPFM and XRD data, we have shown that even when the film shows a predominant SL-layered structure, a small fraction of crystallites with the BL structure may also appear laterally segregated and remain embedded within the film (Figures 4, 5, and S4), causing a large spatial variation in the work function.

In this context, it is worth mentioning that Resel and co-workers have proposed a specific type of structural disorder in which the head-to-head stacking within the crystalline bilayer includes a fraction of flipped molecules. In view of our results, we believe that such defective BL packing will also lead to electrostatic disorder.²⁰

The observed changes in IP are not expected from a purely electrostatic picture, according to which the HOMO should closely follow the vacuum level resulting in a constant IP; however, any speculation is avoided here since a reliable interpretation of UPS can be particularly difficult for energetically inhomogeneous surfaces at the nanoscale.⁴⁸

Overall the findings of this work are projected to exert a significant influence on device performance, unraveling factors affecting the field-effect mobility, the threshold voltage, and contact resistance, which certainly warrant further investigation. Given that the formation of polar structures and different kinds of defects are expected to be very sensitive to the processing protocol, the characterization of polymorphism in thin films should go beyond a simple specular XRD and morphological analysis. X-ray characterization lacks the necessary spatial resolution and does not allow us to probe easily the coexistence of the different polymorphs at microscopic scale.

The stacking of single molecular layers on top of the bottom bilayer is the result of a subtle interplay of electrostatic and van

der Waals interactions, which are expected to be also in play for other asymmetric BTBT derivatives explored for their high potential in high mobility OFETs.^{15,30}

CONCLUSIONS

In this study, we unveil the great level of structural intricacy of Ph-BTBT-10 thin films that goes beyond the reported single-layer to bilayer transformation model. We demonstrate that between the double layer structure located directly at the substrate surface and the metastable thin-film phase, there is a structural phase that consists of the packing of polar single layers. DFT electronic structure calculations quantify a shift in the vacuum level by -0.273 eV per layer, assuming a defect-free polar layer of oriented chain-up molecules, which is in excellent agreement with the measured SP. Experimentally, the shift is reduced for subsequent layers and is explained by an increase in the percentage of flipped molecules. The net dipole cancellation (nonpolar) is almost exact for the alternate (1:1) ratio, reaching above a critical film thickness of ≈ 20 nm. We conclude that in polar organic semiconductor thin films, flipping of molecules is the polarity compensation mechanism.

Our study underscores that KPFM is a valuable tool to evaluate electrostatic disorder and the conceivable emergence of polar polymorphs in thin films. We identify a variable number of structural defects in the form of individual flipped molecules (point defects) or sizable polar domains (with chain-up and chain-down configurations). The actual film structure has dramatic consequences in the electronic properties, in particular, a decrease in the work function of the film with increasing thickness (up to ~ 1 eV) and a broadening of the HOMO attributed to electrostatic disorder.

The synthesis of asymmetric compounds by molecular engineering is a recently developed strategy for obtaining layered crystalline OSCs with high field-effect mobility. The findings of this study imply that the development of polar assemblies may represent a common issue for other asymmetric BTBT derivatives and deserve consideration for understanding the structure–property relationships in OFETs. A precise determination of the possible formation of polar assemblies close to the interface is pivotal for the strategic design and advancement of high-performance OFETs.

EXPERIMENTS AND METHODS

Molecular Film Growth. Ph-BTBT-10 (purchased from TCI Chemicals) films were grown from the vapor phase with a deposition rate of ≈ 2 Å/min onto the native oxide surface of Si(100) substrates (p-type) under high vacuum conditions (10^{-7} mbar) and at different substrate temperatures, ranging from 25 to 90 °C. The substrates were cleaned by sonication in acetone and ethanol for 10 min each, followed by 10 min of UV-ozone cleaning. The growth rates were monitored by a quartz crystal microbalance (QCM). The amount of deposited molecules is given as the nominal thickness in nm.

AFM and KPFM. Topographic and local SP measurements were performed at RT under a N_2 gas atmosphere to minimize moisture effects, using a Cypher ES Environmental AFM instrument, from Asylum Research (Oxford Instruments). KPFM measurements were conducted in amplitude modulation (AM-KPFM) with an AC voltage of 1 V at the frequency of the first eigenmode in a two-pass procedure (Nap mode). During the first pass, a topographic contour line is recorded in dynamic mode (constant amplitude). In a second pass, the KPFM is obtained while the mechanical excitation is switched off and the tip is driven to follow the topographic contour but approached toward the sample surface by a selected height difference. For the setup employed, where the voltage bias is applied to the tip, higher (lower) SP corresponds to lower (higher) surface work

function. The shift in E_{vac} in units of eV corresponds to the absolute value with the shift of SP in units of volts but has an opposite sign. Silicon tips with a Ti/Ir (5/20 nm) coating and a nominal spring constant of 2.8 (N/m) were employed.

UPS. VB and secondary electrons cutoff (SECO) spectra were measured by ultraviolet photoelectron spectroscopy (UPS) using an ultrahigh-vacuum (UHV) system equipped with a SPECS Phoibos 150 hemispherical energy analyzer and a Helium lamp ($h\nu = 21.22$ eV). To have access to the work function from the SECO, the corresponding spectra were taken with the samples biased at -10 V. A Au(111) single crystal was used as a reference for Fermi energy determination. The full width at half-maximum of the HOMO has been used as an indicator of disorder, which was extracted by using the Gaussian distribution to fit the first HOMO from each spectrum.

XRD. XRD in specular geometry was performed with a D8 DISCOVER multipurpose X-ray diffractometer (Bruker) using a wavelength of 1.542 \AA (Cu $K\alpha$). The 2D diffraction pattern was acquired by GIWAXS at the BL11-NCD-SWEET beamline of the ALBA Synchrotron (Spain) using a photon energy of 12.4 keV with an incident angle of 0.13° .

Theoretical Calculations. The theoretical investigation of the electronic properties (electrostatic potential and energy levels) was done at the DFT level using the SIESTA code.^{49,50} The calculations were carried on using the PBE functional with a real-space grid cutoff of 350 Ry , a DZP (double- ζ + polarization) orbital basis set, and a k-point grid of $(3 \times 2 \times 1)$. The organization of the BTBT films was modeled based on the crystalline unit cell obtained by Hofer et al. using MD simulations.¹⁹ From the bulk structure, we have generated several conformations to model SL structures with several “down:up” ratios. The electrostatic potential was computed from the converged electron density using the Macroave tools.⁴⁷ A large vacuum region was considered perpendicular to the layer surface, and a dipolar correction was applied to cancel the cell self-interaction.

■ ASSOCIATED CONTENT

Supporting Information

The Supporting Information is available free of charge at <https://pubs.acs.org/doi/10.1021/acs.chemmater.3c02926>.

Additional topographical and surface potential maps obtained by KPFM illustrating the coexistence of different polymorphs, GIWAXS data as well as further details of the calculations (PDF)

■ AUTHOR INFORMATION

Corresponding Authors

Carmen Ocal – Instituto de Ciencia de Materiales de Barcelona (ICMAB-CSIC), E-08193 Barcelona, Spain; orcid.org/0000-0001-8790-8844; Email: cocal@icmab.es

Esther Barrera – Instituto de Ciencia de Materiales de Barcelona (ICMAB-CSIC), E-08193 Barcelona, Spain; orcid.org/0000-0001-9163-2959; Email: e.barrera@csic.es

Authors

Shunya Yan – Instituto de Ciencia de Materiales de Barcelona (ICMAB-CSIC), E-08193 Barcelona, Spain

David Cornil – Laboratory for Chemistry of Novel Materials, University of Mons (UMONS), 7000 Mons, Belgium; orcid.org/0000-0002-9553-1626

Jérôme Cornil – Laboratory for Chemistry of Novel Materials, University of Mons (UMONS), 7000 Mons, Belgium; orcid.org/0000-0002-5479-4227

David Beljonne – Laboratory for Chemistry of Novel Materials, University of Mons (UMONS), 7000 Mons, Belgium; orcid.org/0000-0002-2989-3557

Rogger Palacios-Rivera – Instituto de Ciencia de Materiales de Barcelona (ICMAB-CSIC), E-08193 Barcelona, Spain; orcid.org/0000-0002-9574-3741

Complete contact information is available at:

<https://pubs.acs.org/doi/10.1021/acs.chemmater.3c02926>

Author Contributions

The manuscript was written through contributions of all authors. All authors have given approval to the final version of the manuscript.

Notes

The authors declare no competing financial interest.

■ ACKNOWLEDGMENTS

This work was funded by the Spanish Ministry under project PID2022-136802NB-I00 (AEI/FEDER, UE) and through the “Severo Ochoa” Programme for Centers of Excellence in R&D (FUNFUTURE CEX2019-000917-S). This study is part of the Advanced Materials programme (In-CAEM project) and is partially supported by MCIN with funding from European Union NextGenerationEU (PRTR-C17.I1) and by Generalitat de Catalunya. S.Y. is financially supported by the China Scholarship Council (CSC) under Grant No. 202006990034. This work has been carried out within the framework of the doctoral PhD program of Material Science, Department of Physics of the Universitat Autònoma de Barcelona (UAB). We are indebted to G. Sauthier from the ICN2 Photoemission Spectroscopy Facility and to the XRD service group of the ICMAB. GIWAXS experiments were performed at the beamline BL11—NCD-SWEET at ALBA Synchrotron with the collaboration of ALBA staff. This work was supported by the Energy Transition Fund of the Belgian Federal Government (FPS Economy) within the T-REX project. The computational resources were provided by the Consortium des “Equipements de Calcul Intensif” (CECI) funded by the Belgian National Fund for Scientific Research (F.R.S.-FNRS) under Grant 2.5020.11. D.B. and J.C. are FNRS Research Directors.

■ REFERENCES

- (1) Schweicher, G.; Garbay, G.; Jouclas, R.; Vibert, F.; Devaux, F.; Geerts, Y. H. Molecular Semiconductors for Logic Operations: Dead-End or Bright Future? *Adv. Mater.* **2020**, *32*, No. 1905909.
- (2) Liu, J.; Gao, M.; Kim, J.; Zhou, Z.; Chung, D. S.; Yin, H.; Ye, L. Challenges and recent advances in photodiodes-based organic photodetectors. *Mater. Today* **2021**, *51*, 475–503.
- (3) Lee, E. K.; Lee, M. Y.; Park, C. H.; Lee, H. R.; Oh, J. H. Toward Environmentally Robust Organic Electronics: Approaches and Applications. *Adv. Mater.* **2017**, *29*, No. 1703638.
- (4) Qian, F.; Bu, X.; Wang, J.; Lv, Z.; Han, S.-T.; Zhou, Y. Evolutionary 2D organic crystals for optoelectronic transistors and neuromorphic computing. *Neuromorphic Comput. Eng.* **2022**, *2*, No. 012001.
- (5) Xie, P.; Liu, T.; Sun, J.; Yang, J. Structures, Properties, and Device Applications for [1]Benzothieno[3,2-b]Benzothiophene Derivatives. *Adv. Funct. Mater.* **2022**, *32*, No. 2200843.
- (6) Tsutsumi, J.; Matsuoka, S.; Inoue, S.; Minemawari, H.; Yamada, T.; Hasegawa, T. N-type field-effect transistors based on layered crystalline donor-acceptor semiconductors with dialkylated benzo-thienobenzothiophenes as electron donors. *J. Mater. Chem. C* **2015**, *3*, 1976–1981.
- (7) He, D.; Qiao, J.; Zhang, L.; Wang, J.; Lan, T.; Qian, J.; Li, Y.; Shi, Y.; Chai, Y.; Lan, W.; Ono, L. K.; Qi, Y.; Bin Xu, J.; Ji, W.; Wang, X.

Ultrahigh mobility and efficient charge injection in monolayer organic thin-film transistors on boron nitride. *Sci. Adv.* **2017**, *3*, No. 1701186.

(8) Wang, L.; Li, T.; Shen, Y.; Song, Y. A theoretical study of the electronic structure and charge transport properties of thieno[2,3-*b*]benzothiophene based derivatives. *Phys. Chem. Chem. Phys.* **2016**, *18*, 8401–8411.

(9) Takimiya, K.; Nakano, M.; Sugino, H.; Osaka, I. Design and elaboration of organic molecules for high field-effect-mobility semiconductors. *Synth. Met.* **2016**, *217*, 68–78.

(10) Yoneya, M. Monolayer crystal structure of the organic semiconductor 7-decyl-2-phenyl[1]benzothieno[3,2-*b*][1]-benzothiophene, revisited. *Jpn. J. Appl. Phys.* **2020**, *59*, No. 090909.

(11) Diao, Y.; Lenn, K. M.; Lee, W. Y.; Blood-Forsythe, M. A.; Xu, J.; Mao, Y.; Kim, Y.; Reinspach, J. A.; Park, S.; Aspuru-Guzik, A.; Xue, G.; Clancy, P.; Bao, Z.; Mannsfeld, S. C. B. Understanding polymorphism in organic semiconductor thin films through nanoconfinement. *J. Am. Chem. Soc.* **2014**, *136*, 17046–17057.

(12) Tsutsui, Y.; Schweicher, G.; Chattopadhyay, B.; Sakurai, T.; Arlin, J. B.; Ruzié, C.; Aliev, A.; Ciesielski, A.; Colella, S.; Kennedy, A. R.; Lemaire, V.; Olivier, Y.; Hadji, R.; Sanguinet, L.; Castet, F.; Osella, S.; Dudenko, D.; Beljonne, D.; Cornil, J.; Samori, P.; Seki, S.; Geerts, Y. H. Unraveling Unprecedented Charge Carrier Mobility through Structure Property Relationship of Four Isomers of Didodecyl[1]-benzothieno[3,2-*b*][1]benzothiophene. *Adv. Mater.* **2016**, *28*, 7106–7114.

(13) Shi, W.; Chen, J.; Xi, J.; Wang, D.; Shuai, Z. Search for organic thermoelectric materials with high mobility: The case of 2,7-dialkyl[1]benzothieno[3,2-*b*][1]benzothiophene derivatives. *Chem. Mater.* **2014**, *26*, 2669–2677.

(14) Iino, H.; Usui, T.; Hanna, J. I. Liquid crystals for organic thin-film transistors. *Nat. Commun.* **2015**, *6*, 6828.

(15) He, K.; Li, W.; Tian, H.; Zhang, J.; Yan, D.; Geng, Y.; Wang, F. Asymmetric Conjugated Molecules Based on [1]Benzothieno[3,2-*b*][1]benzothiophene for High-Mobility Organic Thin-Film Transistors: Influence of Alkyl Chain Length. *ACS Appl. Mater. Interfaces* **2017**, *9*, 35427–35436.

(16) Inoue, S.; Minemawari, H.; Tsutsumi, J.; Chikamatsu, M.; Yamada, T.; Horiuchi, S.; Tanaka, M.; Kumai, R.; Yoneya, M.; Hasegawa, T. Effects of Substituted Alkyl Chain Length on Solution-Processable Layered Organic Semiconductor Crystals. *Chem. Mater.* **2015**, *27*, 3809–3812.

(17) Higashino, T.; Inoue, S.; Arai, S.; Matsui, H.; Toda, N.; Horiuchi, S.; Azumi, R.; Hasegawa, T. Architecting Layered Crystalline Organic Semiconductors Based on Unsymmetric π -Extended Thienocenes. *Chem. Mater.* **2021**, *33*, 7379–7385.

(18) Hamai, T.; Inoue, S.; Arai, S.; Hasegawa, T. Trap-state suppression and band-like transport in bilayer-type organic semiconductor ultrathin single crystals. *Phys. Rev. Mater.* **2020**, *4*, No. 074601.

(19) Hofer, S.; Bodlos, W.; Novák, J.; Sanzone, A.; Beverina, L.; Resel, R. Molecular packing analysis of the crystal smectic E phase of a benzothieno-benzothiophene derivative by a combined experimental/computational approach. *Liq. Cryst.* **2021**, *48*, 1888–1896.

(20) Hofer, S.; Unterkofler, J.; Kaltenegger, M.; Schweicher, G.; Ruzié, C.; Tamayo, A.; Salzillo, T.; Mas-Torrent, M.; Sanzone, A.; Beverina, L.; Geerts, Y. H.; Resel, R. Molecular Disorder in Crystalline Thin Films of an Asymmetric BTBT Derivative. *Chem. Mater.* **2021**, *33*, 1455–1461.

(21) Hofer, S.; Hofer, A.; Simbrunner, J.; Ramsey, M.; Sterrer, M.; Sanzone, A.; Beverina, L.; Geerts, Y.; Resel, R. Phase Transition toward a Thermodynamically Less Stable Phase: Cross-Nucleation due to Thin Film Growth of a Benzothieno-benzothiophene Derivative. *J. Phys. Chem. C* **2021**, *125*, 28039–28047.

(22) Ferrari, E.; Pandolfi, L.; Schweicher, G.; Geerts, Y.; Salzillo, T.; Masino, M.; Venuti, E. Interlayer Sliding Phonon Drives Phase Transition in the Ph-BTBT-10 Organic Semiconductor. *Chem. Mater.* **2023**, *35*, 5777–5783.

(23) Minemawari, H.; Tsutsumi, J.; Inoue, S.; Yamada, T.; Kumai, R.; Hasegawa, T. Crystal structure of asymmetric organic semi-

conductor 7-decyl-2-phenyl[1]benzothieno[3,2-*b*][1]-benzothiophene. *Appl. Phys. Express* **2014**, *7*, 23–26.

(24) Minemawari, H.; Tanaka, M.; Tsuzuki, S.; Inoue, S.; Yamada, T.; Kumai, R.; Shimoi, Y.; Hasegawa, T. Enhanced Layered-Herringbone Packing due to Long Alkyl Chain Substitution in Solution-Processable Organic Semiconductors. *Chem. Mater.* **2017**, *29*, 1245–1254.

(25) Yoneya, M. Monolayer Crystal Structure of the Organic Semiconductor 7-Decyl-2-phenyl[1]benzothieno[3,2-*b*][1]-benzothiophene. *J. Phys. Chem. C* **2018**, *122*, 22225–22231.

(26) Hamai, T.; Arai, S.; Minemawari, H.; Inoue, S.; Kumai, R.; Hasegawa, T. Tunneling and Origin of Large Access Resistance in Layered-Crystal Organic Transistors. *Phys. Rev. Applied* **2017**, *8*, 054011.

(27) Cho, J. M.; Mori, T. Low-Temperature Band Transport and Impact of Contact Resistance in Organic Field-Effect Transistors Based on Single-Crystal Films of Ph-BTBT-10. *Phys. Rev. Appl.* **2016**, *5*, No. 064017.

(28) Jones, A. O. F.; Chattopadhyay, B.; Geerts, Y. H.; Resel, R.; Jones, A. O. F.; Resel, R.; Chattopadhyay, B.; Geerts, H. Substrate-Induced and Thin-Film Phases: Polymorphism of Organic Materials on Surfaces. *Adv. Funct. Mater.* **2016**, *26*, 2233–2255.

(29) Bodlos, W. R.; Mattiello, S.; Perinet, A.; Fischer, R.; Beverina, L.; Caironi, M.; Resel, R. Controlled recrystallization from the melt of the organic n-type small molecule semiconductor 2-decyl-7-phenyl[1]benzothieno[3,2-*b*][1]benzothiophene S₃S₂S₃'-tetraoxide. *J. Cryst. Growth* **2021**, *572*, No. 126255.

(30) He, Y.; Xu, W.; Murtaza, I.; Zhang, D.; He, C.; Zhu, Y.; Meng, H. Molecular phase engineering of organic semiconductors based on a [1]benzothieno[3,2-*b*][1]benzothiophene core. *RSC Adv.* **2016**, *6*, 95149–95155.

(31) Inoue, S.; Nikaido, K.; Higashino, T.; Arai, S.; Tanaka, M.; Kumai, R.; Tsuzuki, S.; Horiuchi, S.; Sugiyama, H.; Segawa, Y.; Takaba, K.; Maki-Yonekura, S.; Yonekura, K.; Hasegawa, T. Emerging Disordered Layered-Herringbone Phase in Organic Semiconductors Unveiled by Electron Crystallography. *Chem. Mater.* **2022**, *34*, 72–83.

(32) Toshiki, H.; Satoru, I.; Yuichi, S.; Shunto, A.; Sachio, H.; Tatsuo, H. Bilayer-type Layered Herringbone Packing in 3-n-Octyl-9-phenyl-benzothieno[3,2-*b*]naphtho[2,3-*b*]thiophene. *Chem. Lett.* **2019**, *48*, 453–456.

(33) Inoue, S.; Higashino, T.; Arai, S.; Kumai, R.; Matsui, H.; Tsuzuki, S.; Horiuchi, S.; Hasegawa, T. Regioisomeric control of layered crystallinity in solution-processable organic semiconductors. *Chem. Sci.* **2020**, *11*, 12493–12505.

(34) Arai, S.; Inoue, S.; Tanaka, M.; Tsuzuki, S.; Kondo, R.; Kumai, R.; Hasegawa, T. Temperature-induced transformation between layered herringbone polymorphs in molecular bilayer organic semiconductors. *Phys. Rev. Mater.* **2023**, *7*, 25602.

(35) Tian, H.; Han, Y.; Bao, C.; Yan, D.; Geng, Y.; Wang, F. An asymmetric oligomer based on thienocene for solution processed crystal organic thin-film transistors. *Chem. Commun.* **2012**, *48*, 3557–3559.

(36) Wu, H.; Iino, H.; Hanna, J. I. Thermally induced bilayered crystals in a solution-processed polycrystalline thin film of phenyl-terthiophene-based monoalkyl smectic liquid crystals and their effect on FET mobility. *RSC Adv.* **2017**, *7*, 56586–56593.

(37) Higashino, T.; Arai, S.; Inoue, S.; Tsuzuki, S.; Shimoi, Y.; Horiuchi, S.; Hasegawa, T.; Azumi, R. Architecting layered molecular packing in substituted benzobisbenzothiophene (BBBT) semiconductor crystals. *CrystEngComm* **2020**, *22*, 3618–3626.

(38) He, Y.; Sezen, M.; Zhang, D.; Li, A.; Yan, L.; Yu, H.; He, C.; Goto, O.; Loo, Y. L.; Meng, H. High Performance OTFTs Fabricated Using a Calamitic Liquid Crystalline Material of 2-(4-Dodecyl phenyl)[1]benzothieno[3,2-*b*][1]benzothiophene. *Adv. Electron. Mater.* **2016**, *2*, No. 1600179.

(39) Arai, S.; Inoue, S.; Hamai, T.; Kumai, R.; Hasegawa, T. Semiconductive Single Molecular Bilayers Realized Using Geometrical Frustration. *Adv. Mater.* **2018**, *30*, No. 1707256.

(40) Tamayo, A.; Hofer, S.; Salzillo, T.; Ruzié, C.; Schweicher, G.; Resel, R.; Mas-Torrent, M. Mobility anisotropy in the herringbone structure of asymmetric Ph-BTBT-10 in solution sheared thin film transistors. *J. Mater. Chem. C* **2021**, *9*, 7186–7193.

(41) Baggioli, A.; Casalegno, M.; Raos, G.; Muccioli, L.; Orlandi, S.; Zannoni, C. Atomistic Simulation of Phase Transitions and Charge Mobility for the Organic Semiconductor Ph-BTBT-10. *Chem. Mater.* **2019**, *31*, 7092–7103.

(42) Cox, S. J. A theory for the stabilization of polar crystal surfaces by a liquid environment. *J. Chem. Phys.* **2022**, *157*, No. 094701.

(43) Tasker, P. W. The stability of ionic crystal surfaces. *J. Phys. C Solid State Phys.* **1979**, *12*, 4977–4984.

(44) Yang, J. P.; Bussolotti, F.; Kera, S.; Ueno, N. Origin and role of gap states in organic semiconductor studied by UPS: As the nature of organic molecular crystals. *J. Phys. D. Appl. Phys.* **2017**, *50*, 423002.

(45) Hagenlocher, J.; Broch, K.; Zwadlo, M.; Lepple, D.; Rawle, J.; Carla, F.; Kera, S.; Schreiber, F.; Hinderhofer, A. Thickness-Dependent Energy-Level Alignment at the Organic–Organic Interface Induced by Templated Gap States. *Adv. Mater. Interfaces* **2022**, *9*, No. 2101382.

(46) Bussolotti, F.; Yang, J.; Hinderhofer, A.; Huang, Y.; Chen, W.; Kera, S.; Wee, A. T. S.; Ueno, N. Origin of the energy level alignment at organic/organic interfaces: The role of structural defects. *Phys. Rev. B - Condens. Matter Mater. Phys.* **2014**, *89*, No. 115319.

(47) Schultz, T.; Lenz, T.; Kotadiya, N.; Heime, G.; Glasser, G.; Berger, R.; Blom, P. W. M.; Amsalem, P.; de Leeuw, D. M.; Koch, N. Reliable Work Function Determination of Multicomponent Surfaces and Interfaces: The Role of Electrostatic Potentials in Ultraviolet Photoelectron Spectroscopy. *Adv. Mater. Interfaces* **2017**, *4*, No. 1700324.

(48) Balderschi, A.; Baroni, S.; Resta, R. Band offsets in lattice-matched heterojunctions: A model and first-principles calculations for GaAs/AlAs. *Phys. Rev. Lett.* **1988**, *61*, 734–737.

(49) Sánchez-Portal, D.; Ordejón, P.; Artacho, E.; Soler, J. M. Density-functional method for very large systems with LCAO basis sets. *Int. J. Quantum Chem.* **1997**, *65*, 453–461.

(50) Sánchez-Portal, D.; Ordejón, P.; Canadell, E. *Computing the Properties of Materials from First Principles with SIESTA*; Springer, 2024; Vol. 113; pp 103–170.

Supporting Information

Polar polymorphism: a new intermediate structure towards the thin-film phase in asymmetric benzothieno[3,2-b][1]-benzothiophene derivatives

*Polar polymorphism: a new intermediate structure towards the thin-film phase in
asymmetric benzothieno[3,2-b][1]-benzothiophene (BTBT) derivatives*

Shunya Yan,¹ David Cornil,² Jérôme Cornil,² David Beljonne,² Rogger Palacios-Rivera,¹ Carmen Ocal¹ and Esther Barrena¹

¹ Instituto de Ciencia de Materiales de Barcelona (ICMAB-CSIC), Campus UAB, Bellaterra, E-08193 Barcelona, Spain.

² Laboratory for Chemistry of Novel Materials, University of Mons (UMONS), 20 Place du Parc, 7000 Mons, Belgium

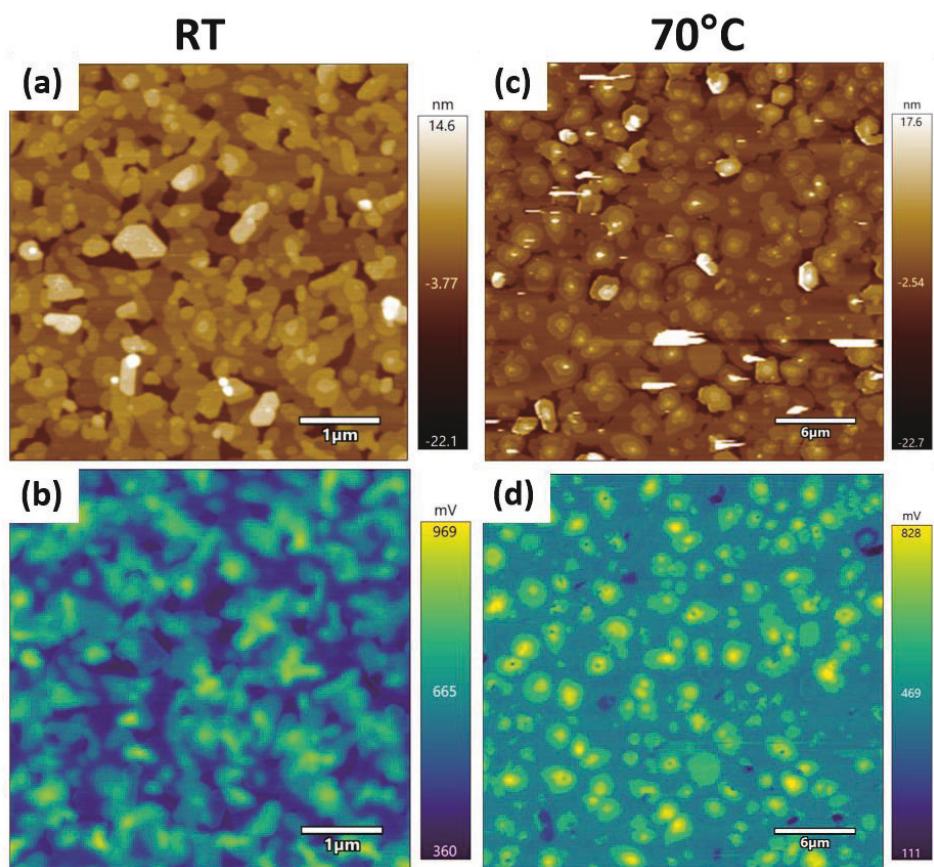


Figure S1. (a) Topographic image (5 μm x 5 μm) and (b) corresponding surface potential map for Ph-BTBT-10 deposited at room temperature. (c) Topographic image (30 μm x 30 μm) and (d) surface potential map for Ph-BTBT-10 deposited at a substrate temperature of 70 $^{\circ}\text{C}$. The substrate is the Si(100) with native oxide. A higher substrate temperature favors the formation of larger terraces during growth; morphologies with larger terraces allow a better quantification of local differences in the surface potential. Nominal thickness is \approx 6-7 nm in both cases.

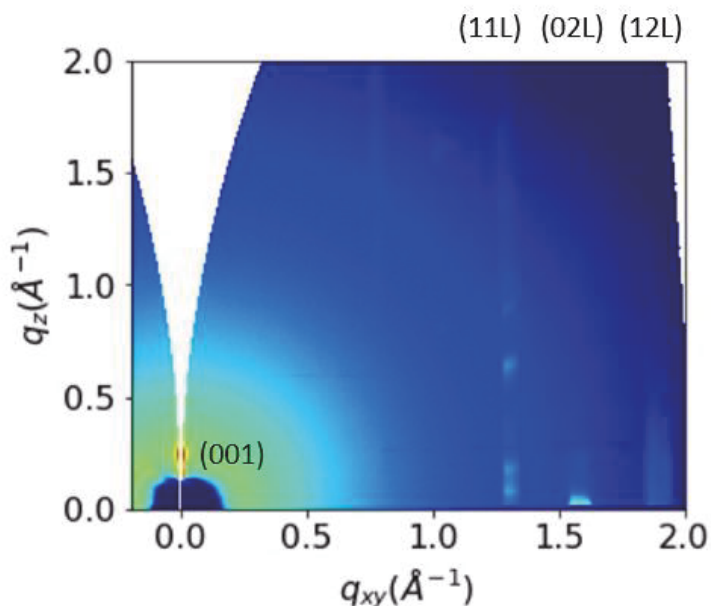


Figure S2. GIWAXS data measured for Ph-BTBT-10 (thickness ≈ 15 nm) on SiO₂ showing the characteristic diffraction pattern of the herringbone BTBT packing.

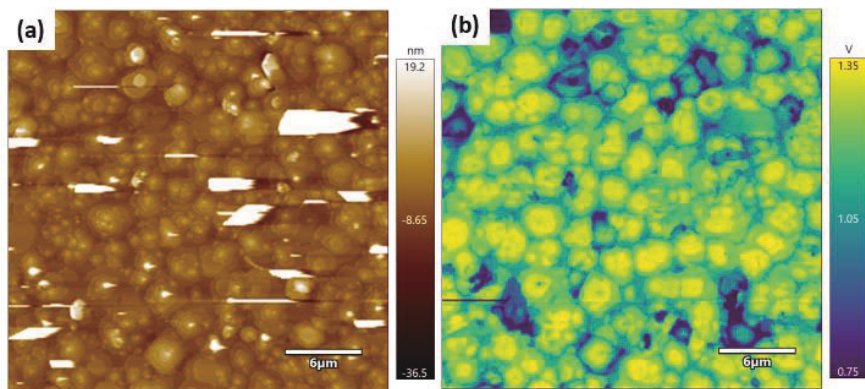


Figure S3. (a) Topographic image and (b) corresponding surface potential map of Ph-BTBT-10 (nominal thickness of ≈ 15 nm) grown on SiO₂ with the substrate kept at 70°C. As described in the text, most of the terraced mounds in the film correspond to stacks of SLs. There are, however, some mounds formed by BL-stacking, which can be distinguished by a lower SP.

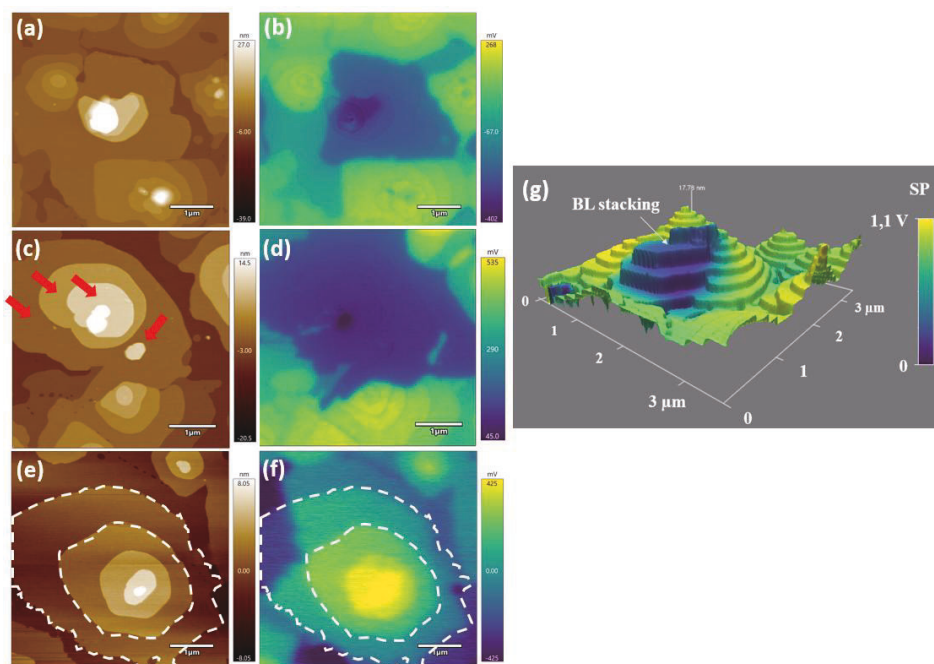


Figure S4. Topographic images (a, c, e) and the corresponding surface potential maps (b, d, f) of Ph-BTBT-10, with a nominal thickness of 12-16 nm, deposited with the substrate held at $\approx 70^\circ\text{C}$. It can be observed that the surface potential maps are not correlated with all morphological features. In some cases, as in e and f, the same terrace (delimited by dashed lines) exhibits more than one value of surface potential due to buried single layers with domain boundaries with opposite (up and down) dipolar orientations. In other regions, as in c and d, terraces with same surface potential are associated to a region of non-polar BL structure (i.e., terraces with a double step height are indicated by red arrows). (g) Three-dimensional visualization of the merged topographic and SP data for a 40 nm-thick film. The main mound is formed, in fact, by two coalescent parts with BL and single layer structures, which are clearly distinguished by double (left mound part) and single (right mound part) step heights, respectively, and by the large difference between the SP for each of the stacking sequences.

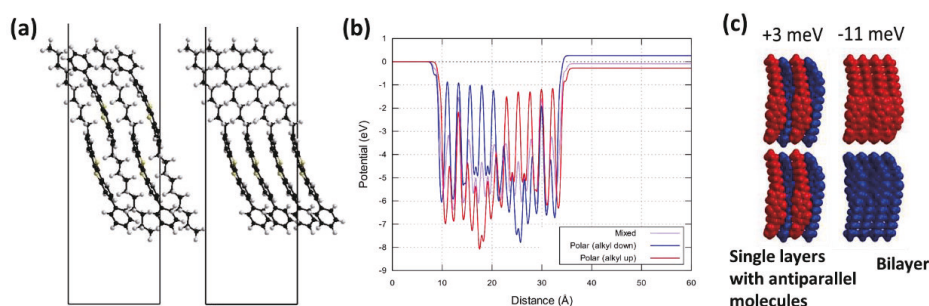


Figure S5. (a) Unit cell used for the calculations discussed in the manuscript. The molecular models are built from the smectic phase reported by Hofer et al. [ref. 17]. (b) Variation of the potential for full mixed vs polar (alkyl up and alkyl down) as a function of the distance to the substrate surface. Up and down configurations refer to the orientation outwards and inwards, respectively, of the alkyl chains of the Ph-BTBT-10 with respect to the substrate. (c) Left: Side view of a stack of two identical layers with a (1:1) ratio of up and down molecular conformations (50%). Right: Side view of a bilayer (BL) made of a pure chain-up layer on top of a pure down layer. The indicated values correspond to the potential shifts in these cases. Colors in (b) are consistent with the used in (c).

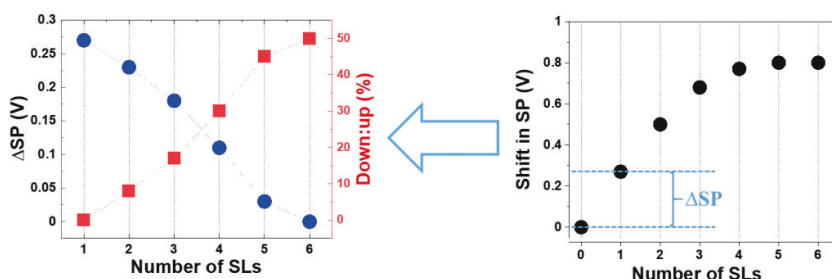


Figure S6. The surface potential increase (ΔSP) arising from the addition of each SL of Ph-BTBT-10 is estimated from the evolution of the SP vs. number of stacked SLs (right) shown in Figure 6c of the manuscript. The ΔSP values thus obtained (blue symbols) are compared with those expected from the calculations in Figure 6a for one molecular layer with a given percentage of down:up molecules. This procedure allows estimating the down:up percentage of each SL (red symbols). The percentage indicates the ratio of flipped molecules (defects), i.e., 0% corresponds to a perfect polar layer of up-chain molecules.

PAPER III

*Thickness dependent structural transition in Ph-BTBT-10
thin films and stabilization of the ubiquitous interface
bilayer*

Thickness dependent structural transition in Ph-BTBT-10 thin films and stabilization of the ubiquitous interface bilayer

Shunya Yan,^a Alba Cazorla,^a Eduardo Solano,^b Carmen Ocal^{a} and Esther Barrena^{a*}*

^a Institut de Ciència de Materials de Barcelona (ICMAB-CSIC), 08193 Bellaterra, Spain

^b ALBA synchrotron, C/de la Llum 2-26, Cerdanyola del Valles, Barcelona, 08290, Spain

KEYWORDS

Interfaces, structure, phase transition, KPFM, GIWAXS

ABSTRACT

The influence of the film/substrate interface and the role of film thickness on the structural transition temperature for thin films of the asymmetric BTBT derivative 7-decyl-2-phenyl[1]benzothieno[3,2-b][1]benzothiophene (Ph-BTBT-10) have been addressed by using Kelvin probe force microscopy (KPFM) and Grazing Incidence Wide Angle X-ray Scattering (GIWAXS). Our data strongly suggest that the structural transformation from a single-layer phase to the thermodynamically stable bilayer structure develops from the bottom of the film to its surface. Contrary to observations in other organic semiconductor films, notably, the thinner the Ph-BTBT-10 film the lower the transition temperature. This unusual behavior is interpreted in terms of a ubiquitous stabilization of the bilayer at the substrate interface which remains unaltered during the transition. The evolution over time of an incomplete organic/inorganic interface (below the interfacial bilayer completion), shows that molecular diffusion and rearrangement at room temperature lead to the bilayer stacking within hours. A result that further confirms the role of the interface stability, provided by the formation of this structure at the film bottom, on the structural transition suffered for thin films grown at room temperature.

INTRODUCTION

The chemical versatility of π -conjugated organic materials as organic semiconductors (OSCs), along with their ease of processing and compatibility make them ideal for a wide array of (opto-) electronic applications.[1],[2],[3],[4] Organic field-effect transistor (OFETs) are significant not only as electronic components in circuits but are also crucial devices in the development of low-cost (bio)chemical sensors.[5],[6],[7],[8] The charge carrier mobility of OSCs, which is one of the main performance metrics for (OFETs), has enormously improved from the very low initial values of $10^{-5} \text{ cm}^2 \cdot \text{V}^{-1} \cdot \text{s}^{-1}$ in the first OFETs demonstrated in the late 1980s to values up to $\approx 10 \text{ cm}^2 \cdot \text{V}^{-1} \cdot \text{s}^{-1}$ in 2000 for p-type OFETs.[1],[2],[3],[9] This impressive advance in performance has been possible by several breakthroughs in the synthesis of high-mobility OSCs, with heterocyclic semiconductors, such as benzothieno[3,2-b]benzothiophene (BTBT) derivatives,[10][11][12][13] and by a better understanding of the underpinning

structure–property relationships achieved thanks to advanced characterization tools. With the synthesis of high performing materials in the last years, the need of controlling the formation of polymorphs is an imperative, not only for securing the one maximizing the charge carrier mobility, but also for producing devices with reproducible performance and high stability.[14][15][16][17] [18][19] Despite the low interaction of molecules with the chemically inert substrates (SiO_2 , Al_2O_3 and polymers) used as dielectrics in thin-film OFETs, the formation of substrate-induced phases (SIP) is a common phenomenon subject of extensive research.[20],[21],[22],[23],[24],[25],[26] From a thermodynamic point of view, surface-induced polymorphism is a consequence of size reduction effects.[27],[28],[29] Because the surface and interface to volume ratio increases with decreasing film thickness, the contributions of the surface and interface energy may become dominant for very thin films. Unfortunately, there is a strong limitation in the experimental techniques available to identify and characterize polymorphism in very thin films and, in particular, fail to provide the spatial distribution of possible coexisting structures.[29]

Lately, the asymmetric BTBT derivative 7-decyl-2-phenyl[1]benzothieno[3,2-b][1]-benzothiophene (Ph-BTBT-10) has been extensively studied due to its excellent charge carrier mobility. Interestingly, it is one example of the critical role the surface has on the polymorphism observed in thin films. Due to the asymmetric shape of this molecule, single crystals exhibit a robust bilayer (BL) packing, where the molecules stack on top of each other in a head-to-head (or tail-to-tail) fashion, resulting in a lamellar stacking periodicity of $d_{\text{BL}} = 5.30$ nm, i.e., twice the molecular length (inset Figure 1b). In substrate-supported thin films, however, the molecules adopt a single-layer (SL) packing (inset Figure 1a). In addition to the important role of the surface, in a recent work [31] we demonstrated that electrostatic interactions in the film impel a rather complex scenario of polymorphism (Figure 1a). Indeed, while the surface favors and stabilizes the formation of a first bilayer, as those forming single crystals, subsequent layers follow a single-layer structure with a predominant alkyl-up (chain-up) orientation of the molecules, imparting a net electrostatic dipole as indicated by local Kelvin probe force

microscopy data.[31],[32] As illustrated in Figure 1a, for increasing number of layers, the density of defects in the form of flipped molecules rises up until the eventual formation of the thin-film SL phase, where each layer consists of an anti-parallel arrangement of the molecules (i.e., alternated “chain-up” and “chain-down” molecules). In other words, there is an intermediate defective film region for the passage from the bilayer structure formed at the substrate surface to the thin-film structure, which is not fully developed for thicknesses under a certain value.

Several works have pointed that the single-layer packing in thin films is a metastable structure, undergoing an irreversible transformation to the thermodynamically stable BL structure via thermal annealing at $T > 115\text{ }^{\circ}\text{C}$, rendering approximately ten times higher mobility.[33],[34],[35],[35]. The crystalline order and packing quality in thin films are at the origin of the performance and stability of devices.

As validated in our previous work, Kelvin probe force microscopy (KPFM) is a valuable tool for evaluating the conceivable emergence of polar polymorphs.[30] Here we combine KPFM and Grazing Incidence Wide Angle X-ray Scattering (GIWAXS) to monitor the structural changes in Ph-BTBT-10 thin films with thermal annealing for different thicknesses. We demonstrate the role of the interface on the structural transformation in Ph-BTBT-10 thin films, with strong implications on the effect of thickness on the stability of the structure with thermal annealing and aging.

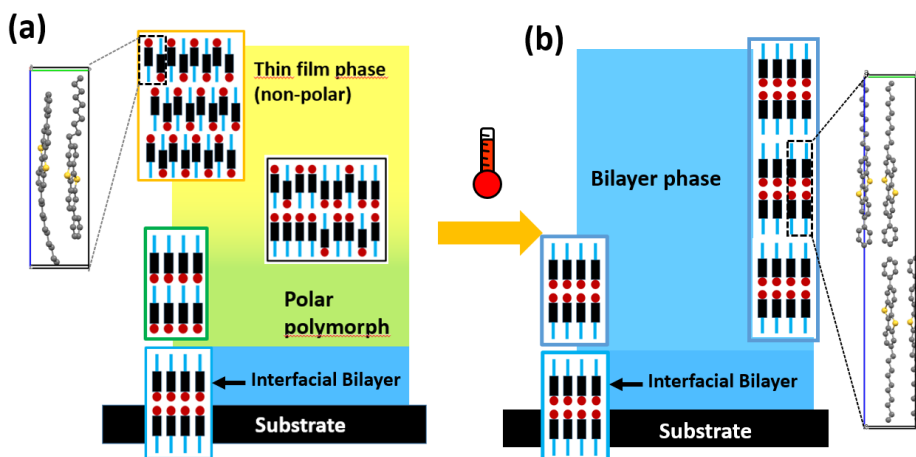


Figure 1. Cartoon illustrating the structural transition after annealing a film of Ph-BTBT-10 deposited at room temperature on the native oxide of silicon. (a) The as grown film exhibits the polar polymorphism and evolution to the thin film phase (non-polar) with thickness, adapted from[30]. (b) At a given (onset) temperature of post-growth annealing, the film undergoes a transition to the stable bilayer phase (non-polar).[31] The molecular bilayer at the interface is stabilized by the substrate and is not affected during the transition.

EXPERIMENTAL SECTION

Thin Film Growth

Ph-BTBT-10 (TCI Chemicals) thin films were grown on the native oxide of p-type Si(100) substrates via vapor-phase deposition at a controlled rate of 2 Å/min under high vacuum conditions (10^{-7} mbar) and a constant room temperature (RT) of 25 °C. Before deposition, the substrates were cleaned by sonication in acetone and ethanol (10 minutes each), followed by UV-ozone treatment for 10 minutes. Deposition rates were monitored by a quartz crystal microbalance (QCM). The nominal film thickness given throughout

this work corresponds to the measured by AFM. Transmission electron microscopy grids were used as shadow masks for selective deposition in order to keep uncovered regions of the silicon oxide to be used as a reference (see text). All thermal treatments here are post-growth annealing treatments.

KPFM

Topographic and local surface potential (SP) measurements were conducted under a nitrogen gas atmosphere to minimize any moisture effect. Kelvin probe force microscopy (KPFM) measurements were performed using the amplitude modulation (AM-KPFM) mode with an AC voltage of 1V at the first eigenmode frequency, in a two-pass procedure (Nap-mode) using a Cypher ES Environmental AFM (Oxford Instruments) equipped with *in situ* heating capabilities. Then, for the post-annealing studies, the as grown films were annealed at selected temperatures for 5 minutes and imaged *in situ* by KPFM. The acquisition time per image was 9 minutes (256x 256 pixels), or 17 minutes (512x512 pixels). Subsequent imaging was performed in the same sample stage after cooling down to 25 °C with a rate of 1 °C·s⁻¹. Pt-coated Silicon tips mounted on cantilevers with a nominal spring constant of 5.4 N·m⁻¹ were employed (HQ:NSC35 from MikroMash).

Topographic step heights and surface potential values were extracted by performing local or global histograms of the topographic and KPFM images. The error bars given in the plots correspond to analysis of the width half height of the gaussian fits of the histogram peaks.

GIWAXS

2D diffraction patterns were acquired by Grazing Incidence Wide Angle X-ray Scattering (GIWAXS) at the BL11-NCD-SWEET beamline of the ALBA Synchrotron (Spain) using a photon energy of 12.4 keV. A large-area 2D Rayonix LX 255-HS detector was used, which consists of a pixel array of 2880 * 960 (V * H) with a pixel size of 88.54 * 88.54 μm² for the binning employed. The scattering vector (q) was

calibrated using Cr_2O_3 as a calibration standard and pyFAI python library.[36] The conversion of the data to the reciprocal space was performed by using a developed python routine, obtaining the out-of-plane (OOP), q_z , and in-plane (IP), q_{xy} , components of the scattering vector corresponding to the directions perpendicular and parallel to the surface, respectively. The films were annealed in a Linkam heater stage for 5 minutes at each temperature and cooled down to RT at a cooling rate of $2.5^\circ \text{C} \cdot \text{s}^{-1}$ or measured in real time during annealing. For each series of measurements, the sample was moved stepwise to a fresh spot, minimizing radiation damage.

RESULTS

Intermediate film thickness (40 nm)

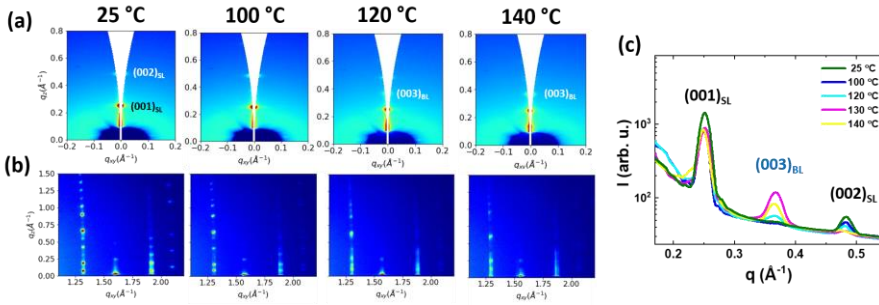


Figure 2. Out-of-plane (a) and in-plane (b) 2D-GIWAXS maps for a 40nm-thick thin film of Ph-BTBT-10, obtained at the indicated temperatures using an incident angle of 0.12° . Labels SL and BL stand for reflections corresponding to the single layer and bilayer structures, respectively. (c) Intensity distribution along the out-of-plane direction.

We first discuss the *in situ* GIWAXS, monitored for a 40 nm-thick Ph-BTBT-10 film during thermal annealing. The selected 2D diffraction patterns in Figure 2 illustrate the structural transition taking place in the film. Two regions of the reciprocal space are shown, OOP (a) and IP (b), measured at different temperatures from 25 to 140 °C. At room temperature, $(00l)$ Bragg diffraction reflections are observed in the OOP region.

The (001) peak position $q_z = 0.235 \text{ \AA}^{-1}$ has been obtained from a specular scan (Figure S1), where Bragg peaks up to the fifth diffraction order are visible corresponding to a interlayer spacing of 26.74 \AA , which is the periodicity of the SL structure typical of thin films. However, it is worth mentioning that no information on the molecular arrangement (i.e., parallel or anti-parallel) within each layer can be inferred from these data. The diffraction pattern in the IP region (Figure 2b) is dominated by the diffraction features observed at $q_{xy} = 1.32, 1.60, \text{ and } 1.91 \text{ \AA}^{-1}$, which correspond to the $(11l)$, $(20l)$ and $(12l)$ rods characteristic of the herringbone packing adopted by the BTBT cores. The diffraction pattern at RT is in agreement with the thin-film SL phase structure reported by Hofer et al.[31] As can be seen, annealing up $100 \text{ }^\circ\text{C}$ does not produce appreciable changes in the structure. However, the appearance of a new Bragg reflection along the q_z direction after annealing at $120 \text{ }^\circ\text{C}$ (Figure 2a) evidences the emergence of another unit cell with double periodicity along the c-axis. The Bragg peak observed at $q_z \approx 0.36 \text{ \AA}^{-1}$ corresponds to the third diffraction order of the BL structure and has been accordingly labelled as $(003)_{BL}$. As it can be seen in Figure 2c, further film annealing leads to an increase of the intensity of this BL Bragg peak, indicating the ongoing transformation from the single-layer to the bilayer stacking. A rough estimation of the crystal coherence length is obtained from the full width half maximum (FWHM) of the Bragg peaks (Figure S2). At RT, the crystal coherence length is consistent with the film thickness, indicating that the initial SL phase presents well-ordered domains extending across the film. The $(003)_{BL}$ peak is considerably broad at $120 \text{ }^\circ\text{C}$, but becomes narrower upon successive annealing, indicating an increase of the crystal coherence length in the OOP direction across the thickness, suggesting that the SL-BL transformation occurs in the vertical direction (we will be back to this point later).

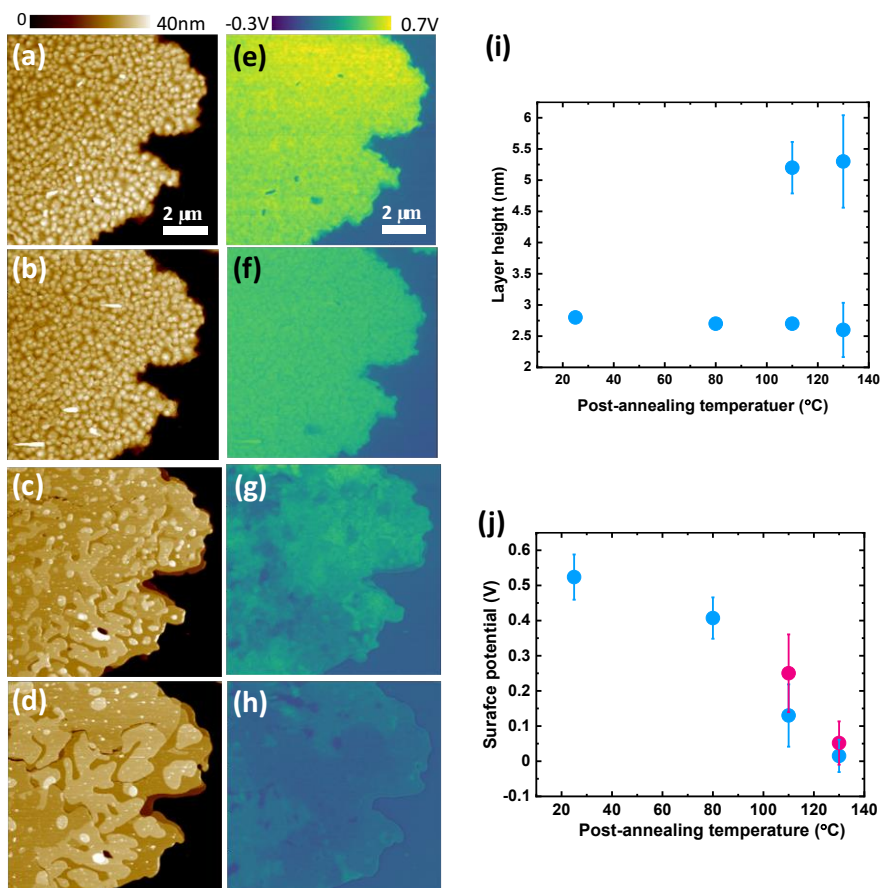


Figure 3. Topography and surface potential maps for a 40 nm-thick thin film of Ph-BTBT-10 as grown at 25 °C (a and e) and after post-growth annealing at 80 °C (b and f), 110 °C (c and g) and 130 °C (d and h). All images in this figure have been taken upon cooling down to RT. Note: A shadow mask was used during molecular deposition to leave uncovered substrate regions (darker in the right part of the images) that were used as in situ reference. The measured values of step height (individual layer thickness) and surface potential for each case are shown in (i) and (j), respectively.

To have a description of the observed phase transition in the real space, we measured the topography and surface potential of a Ph-BTBT-10 thin film (≈ 40 nm) after annealing at different temperatures (25 °C, 80 °C, 110 °C and 130 °C). The results are shown in

Figure 3, which also includes a summary of the measured step heights separating the terraces (individual layer thickness) and the surface potential in each case (right panels in Figure 3). Because the time acquisition per image in KPFM in this case is quite large (9 min), to avoid the joint effect of time plus temperature, the images were acquired after cooling down back to RT. In order to have areas with bare surface as an accurate *in situ* reference for surface potential values, molecular deposition was made through a shadow mask (see experimental section). The topography of the as-prepared film (Figure 3a) shows the characteristic morphology consisting of terraces separated by steps with a height corresponding to a single-layer ($\approx 2.8 \pm 0.1$ nm), in good agreement with the GIWAXS data at RT. For better visualization of the terraces, a magnified image is shown in Figure S3. This as-deposited film shows a more positive SP (Figure 3e) with respect to the substrate by more than 0.5 V. Note that, due to the asymmetric structure of Ph-BTBT-10, the global dipole moment compensates for both, a perfect bilayer packing and a perfect single-layer structure with antiparallel arrangement of the molecules (see both in Figure 1). Not being the case for the film in Figure 3a, the more positive electrostatic surface potential is attributed, as already commented, to a unbalanced chain-up to chain-down ratio with a predominant alkyl-up arrangement.[30] In summary, GIWAXS gives clear proof of a single-layer stacking and in-plane herringbone arrangement of the cores in the as-deposited film, but KPFM indicates a deviation, to a certain extent, from the perfect antiparallel molecular packing of the reported thin film SL structure. After annealing to 80 °C, despite no changes are discerned in the film morphology (Figure 3b) there is a decrease of the overall SP of the molecular film (Figure 3f). The most plausible explanation being that the thermal energy provided by annealing results in a reduction of the molecular disorder, at the origin of the net electrical dipole, towards a more balanced chain-up to chain-down ratio. Such a rearrangement may imply intra-layer diffusion of molecules and/or molecular flipping within a layer.[37]

Upon annealing to 110 °C, notable morphological changes occur (Figure 3c) as irrefutable proof of a structural conversion. On the one hand, a significant increase in the

lateral size of the terraces, that at this stage extend over few micrometers. On the other hand, the measured step height has doubled and is now 5.4 ± 0.1 nm (Figure 3i), correspond to the interlayer spacing of the bilayer structure. This transformation is accompanied by an additional, though no homogeneous, reduction of the SP (Figure 3g). This inhomogeneous SP can be interpreted as a lateral spatial variability in the extend and quality of the crystalline structure. Post-growth annealing at 130 °C leads to an enlargement of the bilayer terraces (Figure 3d). At this stage the surface potential of the film becomes quite homogeneous and drops to its minimum, nearly the substrate SP value (Figure 3j). The thin film behaves as transparent in terms of net dipole moment, indicating that the transition to the non-polar bilayer is nearly complete. But, although the bilayer is the predominant structure, single-layer height terraces do also exist (Figure 3i). The coexistence of both interplanar distances on the uppermost surface, upon annealing at 110 and 130 °C, supports our interpretation that reaching the BL structure by thermal annealing starts from the lower region of the film.

Remarkably, the structural transformation could be captured *in real time* during *in situ* imaging at 110 °C (Figure 4). The slow process of KPFM imaging permitted us to visualize an abrupt change in both, topography (Figure 4a) and surface potential (Figure 4b), happening in a much shorter time scale. Note that the signaled variations are observed along few scanning lines, i.e., in about some seconds.

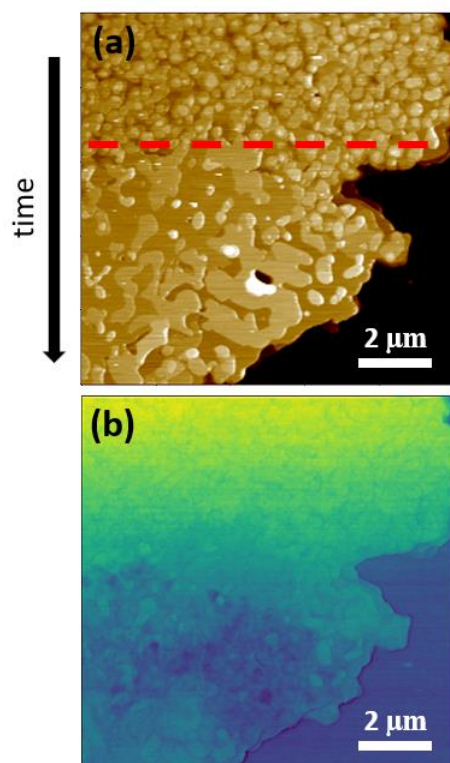


Figure 4. Topography (top) and surface potential (bottom) acquired during in situ annealing at 110 °C. The horizontal red dashed line highlights the time at which the sudden change in morphology related to the transition from single-layer to bilayer is observed. The scan direction is from top to the bottom (total acquisition time was 9 minutes). The total color scales are 40 nm (topography) and from -150 to 550 mV for dark to light SP contrast.

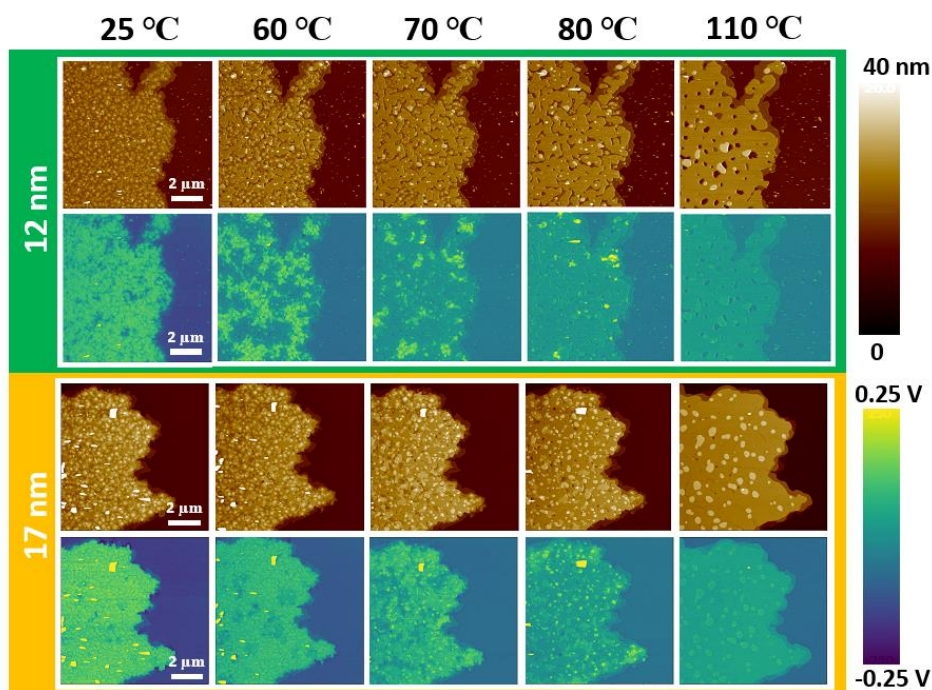


Figure 5. Topography and surface potential maps for Ph-BTBT-10 thin films with a thickness of 12 nm (top) and 17 nm (bottom) as grown at RT and after post-growth annealing at the indicated temperatures in each column.

Low thin film thickness (<20nm)

Because we know[30] that the thin-film structure (inset Figure 1a) is not fully developed for thicknesses below 20 nm, we address the structural transition for two thinner films (12 and 17 nm) grown at RT and restricting the post-growth annealing to temperatures between 60 and 110 °C (Figure 5). Data for intermediate temperatures (90 and 100 °C) are given in Figure S4. The as-deposited films (left column) show single-layered mounds like the single-layered morphology of the 40 nm-thick film at RT (Figure 3a). Both thin films exhibit a more positive SP than the substrate. We first note that while the morphology of the 17 nm-thick film remains basically unchanged upon annealing to 60 °C, the 12 nm-thick film (top panels) already manifests signs of the

transition to the BL structure at this temperature (for more detailed comparison see Figure S5). In particular, the thinnest film locally exhibits regions of enlarged terraces with bilayer step height and a correlated reduction of SP with a nearly bimodal contrast (one value similar to that of the substrate). For this film, the changes in morphology and SP, accompanying the transition towards the BL structure, are almost completed at 80 °C in this film, but annealing at 110 °C still produces lateral coalescence that leaves open voids reaching the underneath substrate, proof of vertical mass transport. The result is a film of bilayer stacking with a quite flat surface. For the 17 nm-thick film (bottom panels), a similar behavior is observed but the onset of the transition occurs at a larger temperature: large bilayer terraces emerge only upon annealing at 80 °C. Similarly, to the described above, this onset is accompanied by the reduction in SP and followed by the surface flattening with evidence of vertical mass transport. The structural transition seems to be complete upon further annealing at 100 °C (Figure in S4). Except for the voids visible in the 12nm-thick, the appearance of both thin films at 110 °C is quite homogenous (last column in Figure 5), though in terms of SP there are still few signs of molecular disorder (some unbalanced chain-up and chain-down ratio that provides small contrasts).

The described transition is quantitatively illustrated in terms of step height in Figure 6, for the 12 nm (a) and 17 nm (b) thin films, respectively. Additionally, the extracted onset temperatures for the bilayer formation are plotted in Figure 6c, including those of the 40 nm-thick film described in the previous section and the reported for a thicker film.[31] We remind that for the investigated 40nm- thick film, single- and double-layer step heights were found even at 130 °C. The cartoon in Figure 6d exemplifies the observed phenomenon.

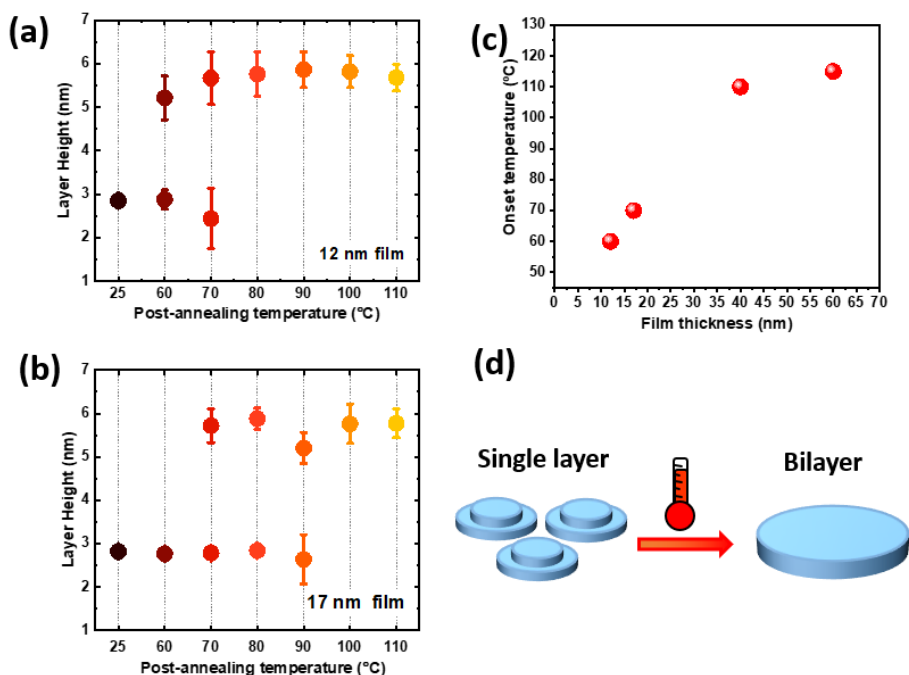


Figure 6. Layer thickness or step height and surface potential data for 12 nm-thick (a) and 17 nm-thick (b) thin films as prepared at RT and after post-growth annealing at different temperatures. (c) The bilayer onset temperature for film with different thickness, included the reported value for a 60 nm-thick film.[31] (d) Cartoon illustrating the transition between a single layer stack and a bilayer driven by post-growth annealing.

Visualization of the transition with time.

Although films of Ph-BTBT-10 grown at room temperature on surfaces are reported to develop the single layer thin film structure above a given thickness,[31],[30] it has been established that, for all thin film thicknesses, the silicon substrate favors and stabilizes the formation of what is considered a first bilayer at the interface, that is, in direct contact with the substrate (see Figure 1). However, the existence of such a ubiquitous interfacial bilayer cannot be accessed by GIWAXS, nor can a direct thickness measurement be made by AFM unless the molecular bilayer leaves regions of substrate.

In addition, from the results and discussion above, the lower the film thickness the lower the temperature needed to start the transition from a single layer packing to the bilayer structure. Therefore, there is a twofold interest to address very low Ph-BTBT-C10 depositions leaving bare regions of the substrate surface and analyzing the evolution over time at the growth temperature.

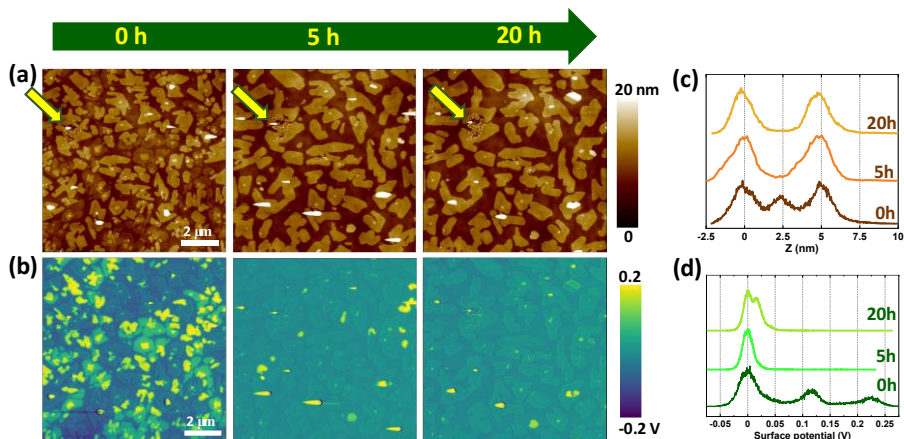


Figure 7. Topography (a) and surface potential (b) images for a film with nominal thickness of 3 nm, acquired immediately after growth ($t = 0$ h) at RT and after 5 and 20 h, respectively. A defect is marked in the images as a reference. Plots in (c) and (d) show the corresponding islands height and surface potential histograms. All measurements were taken at low HR (under N_2 atmosphere).

The evolution of morphology over time has been analyzed for a Ph-BTBT-10 nominal thickness of ≈ 3 nm deposited on the native silicon oxide substrate at RT. As can be seen in Figure 7a, the as-prepared sample grown at RT consists of islands with two different heights (around 2.5 nm and 5.0 nm), which are attributed to molecular assemblies with single-layer and double-layer thickness, respectively. Note that 0 h indicates that the sample was measured immediately after growth. The coexistence of the two types of islands can be attributed to the kinetics of the growth at the growth conditions. As already reported [30] in addition to the unequivocal differences in height, the inherent

asymmetry of this BTBT derivative prominently denotes distinction between bilayer and single-layer islands in the SP map of Figure 7b (0 h). Moreover, a two single layers stack and one bilayer stack have the same height but can be clearly differentiated. Whereas the non-polar bilayer packing denotes no appreciable net dipole moment (SP similar to that of the substrate), each single-layer island (i.e., polar) has a more positive SP, a value doubled when two of them are piled up (see Figure S6). The summary of island height and surface potential as a function of time are plotted in Figure 7c and Figure 7d, respectively. Notably, most morphological changes take place during the first 5 hours with negligible modifications afterwards. The evident surface diffusion leads to coalescence of the islands but interlayer mass transport also occurs as height and surface potential values indicate that all islands exhibit the bilayer stack.

SUMMARY AND DISCUSSION

The presented GIWAXS and KPFM investigation provides a consistent picture of the structural transformations for a 40 nm-thick film grown at RT. At this temperature, the film exhibits a single-layer packing with clear (*00l*) Bragg peaks along the out-of-plane direction and the characteristic in-plan herringbone arrangement of the BTBT cores, convenient for transport channel in OFETs. While the transition temperature between the single-layer and bilayer stacks are consistent with that reported, the surface potential data from KPFM demonstrate a complex scenario. The as-prepared film has a positive surface potential anticipated for polar layers. This result means that not all molecules in the film layers are in the perfect antiparallel arrangement expected for the so called thin-film structure (Figure 1a). Conversely, there is a certain degree of orientational disorder rendering a net electrical dipole. Post-growth annealing at 80 °C reduces the surface potential difference with respect to the substrate, suggesting a tendency towards a non-polar arrangement. For 120 °C, the 2D GIWAXS pattern confirms the appearance of the bilayer structure, which develops with further heating. The reduction of FWHM of the (*003*)_{BL} peak from 120 to 140 °C points to an increase in the coherence length or long-range crystallographic order. Although from the GIWAXS data the structural

transformation seems to be completed at 130 °C, the morphology shows steps with single-layer height at the surface. This finding allows inferring that the SL to BL structural transformation occurs from the bottom part of the film towards its surface. Moreover, the heterogeneous SP map upon annealing at 110 °C becomes quite homogeneous at 130 °C, indicating an improvement of the lateral crystallization degree within this temperature range.

For thinner films the structural transition is demonstrated to take place at a lower temperature. This is an opposite observation to reports for other organic films. For example, the metastable SIP of pentacene shows an enhanced stability for thinner films (i.e., the transition to the bulk phase occurs at a larger temperature than for thick films).[28] Similarly, Diao et al. reported enhanced kinetic stability of metastable polymorphs of TIPS-pentacene, although in this case the study was performed in confined thin films.[18] On both cases, the enhanced stability of the metastable polymorph can be attributed to the surface energy contribution to the Gibbs energy but limited contribution of the film/substrate interfacial energy.[28] In the case of Ph-BTBT-10, an ubiquitous bilayer is formed at the substrate interface, the stability of such a bilayer points to a greatly optimal interfacial energy in this system. At the top of the bilayer single-layers stack, with an intralayer packing that evolves with thickness from a metastable polar parallel arrangement of molecules (alkyl chain-up) towards the non-polar antiparallel arrangement of the thin-film structure (Figure 1a). With temperature, the metastable polar arrangement on top of the interfacial bilayer evolves to the non-polar bilayer structure of single crystals (Figure 1b). The onset temperature for this structural transition is inversely dependent on film thickness (Figure 6c).

Finally, we have shown that molecular surface diffusion and intralayer mass transport lead to the bilayer assembly in a time scale of hours for Ph-BTBT-10 partially covering the silicon oxide surface. Although out of the scope of this particular work, we remark that thickness effects are expected to be notable on the stability of thin films with

aging,[17] which would particularly concern the performance of organic thin film-based devices.

CONCLUSIONS

The influence of film thickness on the structural transition temperature of Ph-BTBT-10 films has been investigated by GIWAXS and KPFM. Key conclusions are drawn from the obtained results: i) the structural transformation, from single-layer lamella to a bilayer structure, extends from the bottom to the top film surface. Increasing the post-growth annealing temperature improves the vertical and lateral quality of the 40 nm-thick film as indicated by GIWAXS and KPFM, respectively; ii) a decrease of the film thickness (<20 nm) reduces the transition temperature to the thermodynamically stable bilayer phase. This non-evident behavior of Ph-BTBT-10, compared with other materials, is consistent with the stability of the interfacial bilayer as a substrate induced arrangement; iii) such a stability of the bilayer stacking at the interface with the substrate is observed in real space, for a laterally discontinuous deposition (3 nm), by the spontaneous evolution at room temperature over a time scale of few hours.

Some practical conclusions are also derived which are of interest for device design and performance optimization: i) achieving the convenient organic thin film structure implies careful control of the film thickness and thermal treatment processes; ii) to ensure uniform performance across the active layer, lateral electrostatic inhomogeneities (here detected by KPFM) need to be considered; iii) both aging and post-growth thermal annealing need to be optimized depending on the specific thickness of the Ph-BTBT-10 thin film. With the present work we demonstrate the importance of combining real space nanoscale tools and reciprocal space structural techniques to provide a deeper understanding of the relationship between film thickness, structural transitions, and thin film optimization, potentially guiding the development of more efficient and reliable organic semiconductor devices.

ASSOCIATED CONTENT

A PDF file is including with specular x-ray diffraction data as well as additional GIWAXS and KPFM data on the films. The file is available free of charge.

AUTHOR INFORMATION

Corresponding Author

* Esther Barrena, Institut de Ciència de Materials de Barcelona (ICMAB-CSIC), E-08193, Spain; orcid.org/0000-0001-9163-2959; Email: e.barrena@csic.es

*Carmen Ocal, Institut de Ciència de Materials de Barcelona (ICMAB-CSIC), E-08193, Spain; orcid.org/0000-0001-8790-8844; Email: cocal@icmab.es

Author Contributions

The manuscript was written through contributions of all authors. All authors have given approval to the final version of the manuscript.

Funding Sources

Spanish Ministry of Science and Innovation (MCIN), State Investigation Agency (AEI), European Union NextGenerationEU and the Generalitat de Catalunya (PRTR-C17.I1).

ACKNOWLEDGMENTS

This work was funded by the Spanish Ministry of Science and Innovation (MCIN) and State Investigation Agency (AEI) under project PID2022-136802NB-I00 (AEI/FEDER, UE) and through the Severo Ochoa Programme for Centres of Excellence in R&D (CEX2023-001263-S). This study is part of the Advanced Materials programme (In-CAEM project) and is partially supported by the MCIN with funding from European Union NextGenerationEU (PRTR-C17.I1) and by Generalitat de Catalunya. S.Y. is financially supported by the China Scholarship Council (CSC) under Grant No. 202006990034. This work has been carried out within the framework of the doctoral PhD program of Material Science, Department of Physics of the Universitat Autònoma de Barcelona (UAB). GIWAXS experiments were performed at the beamline BL11-NCD-SWEET at ALBA Synchrotron with the collaboration of ALBA staff.

REFERENCES

- [1] T. Nematiram, D. Padula, A. Landi, and A. Troisi, ‘On the Largest Possible Mobility of Molecular Semiconductors and How to Achieve It’, *Adv. Funct. Mater.*, vol. 30, no. 30, p. 2001906, 2020, doi: <https://doi.org/10.1002/adfm.202001906>.
- [2] G. Schweicher, G. Garbay, R. Jouclas, F. Vibert, F. Devaux, and Y. H. Geerts, ‘Molecular Semiconductors for Logic Operations: Dead-End or Bright Future?’, *Adv. Mater.*, vol. 32, no. 10, p. 1905909, Mar. 2020, doi: [10.1002/adma.201905909](https://doi.org/10.1002/adma.201905909).
- [3] C. Wang, X. Zhang, H. Dong, X. Chen, and W. Hu, ‘Challenges and emerging opportunities in high-mobility and low-energy-consumption organic field-effect transistors’, *Adv. Energy Mater.*, vol. 10, no. 29, p. 2000955, 2020.
- [4] J. Liu *et al.*, ‘Challenges and recent advances in photodiodes-based organic photodetectors’, *Mater. Today*, vol. 51, pp. 475–503, 2021.
- [5] S. Yuvaraja *et al.*, ‘Organic field-effect transistor-based flexible sensors’, *Chem. Soc. Rev.*, vol. 49, no. 11, pp. 3423–3460, 2020.
- [6] Y. Yan, Y. Zhao, and Y. Liu, ‘Recent progress in organic field-effect transistor-based integrated circuits’, *J. Polym. Sci.*, vol. 60, no. 3, pp. 311–327, 2022.
- [7] X. Zhang, Z. Pu, X. Su, C. Li, H. Zheng, and D. Li, ‘Flexible organic field-effect transistors-based biosensors: progress and perspectives’, *Anal. Bioanal. Chem.*, vol. 415, no. 9, pp. 1607–1625, 2023.
- [8] L. Luo and Z. Liu, ‘Recent progress in organic field-effect transistor-based chem/bio-sensors’, *VIEW*, vol. 3, no. 1, p. 20200115, 2022, doi: <https://doi.org/10.1002/VIW.20200115>.
- [9] A. F. Paterson *et al.*, ‘Recent Progress in High-Mobility Organic Transistors: A Reality Check’, *Adv. Mater.*, vol. 30, no. 36, p. 1801079, Sep. 2018, doi: [10.1002/adma.201801079](https://doi.org/10.1002/adma.201801079).
- [10] H. Usta *et al.*, ‘High Electron Mobility in [1]Benzothieno[3,2-b][1]benzothiophene-Based Field-Effect Transistors: Toward n-Type BTBTs’, *Chem. Mater.*, vol. 31, no. 14, pp. 5254–5263, Jul. 2019, doi: [10.1021/acs.chemmater.9b01614](https://doi.org/10.1021/acs.chemmater.9b01614).

- [11] H. Ebata *et al.*, ‘Highly Soluble [1]Benzothieno[3,2-b]benzothiophene (BTBT) Derivatives for High-Performance, Solution-Processed Organic Field-Effect Transistors’, *J. Am. Chem. Soc.*, vol. 129, no. 51, pp. 15732–15733, Dec. 2007, doi: 10.1021/ja074841i.
- [12] R. Wawrzinek *et al.*, ‘Mobility Evaluation of [1]Benzothieno[3,2-b][1]benzothiophene Derivatives: Limitation and Impact on Charge Transport’, *ACS Appl. Mater. Interfaces*, vol. 11, no. 3, pp. 3271–3279, Jan. 2019, doi: 10.1021/acsami.8b16158.
- [13] S. Ryu, C. Yun, S. Ryu, J. Ahn, C. Kim, and S. Seo, ‘Characterization of [1]Benzothieno[3,2-b]benzothiophene (BTBT) Derivatives with End-Capping Groups as Solution-Processable Organic Semiconductors for Organic Field-Effect Transistors’, *Coatings*, vol. 13, no. 1, 2023, doi: 10.3390/coatings13010181.
- [14] T. Salzillo *et al.*, ‘Enhancing Long-Term Device Stability Using Thin Film Blends of Small Molecule Semiconductors and Insulating Polymers to Trap Surface-Induced Polymorphs’, *Adv. Funct. Mater.*, vol. 30, no. 52, p. 2006115, 2020, doi: <https://doi.org/10.1002/adfm.202006115>.
- [15] D. W. Davies *et al.*, ‘Unraveling two distinct polymorph transition mechanisms in one n-type single crystal for dynamic electronics’, *Nat. Commun.*, vol. 14, no. 1, p. 1304, Mar. 2023, doi: 10.1038/s41467-023-36871-9.
- [16] S. K. Park and Y. Diao, ‘Martensitic transition in molecular crystals for dynamic functional materials’, *Chem Soc Rev*, vol. 49, no. 22, pp. 8287–8314, 2020, doi: 10.1039/D0CS00638F.
- [17] T. Oka, N. Shioya, T. Shimoaka, and T. Hasegawa, ‘Structural Rearrangement of Organic Semiconductor Molecules with an Asymmetric Shape in Thin Films’, *J. Phys. Chem. C*, vol. 127, no. 15, pp. 7560–7564, Apr. 2023, doi: 10.1021/acs.jpcc.3c01003.
- [18] Y. Diao *et al.*, ‘Understanding polymorphism in organic semiconductor thin films through nanoconfinement’, *J. Am. Chem. Soc.*, vol. 136, no. 49, pp. 17046–17057, 2014.

- [19]I. B. Rietveld, ‘Solid-solid phase transitions between crystalline polymorphs of organic materials’, *Curr. Pharm. Des.*, vol. 29, no. 6, pp. 445–461, 2023.
- [20]A. O. Jones, B. Chattopadhyay, Y. H. Geerts, and R. Resel, ‘Substrate-induced and thin-film phases: Polymorphism of organic materials on surfaces’, *Adv. Funct. Mater.*, vol. 26, no. 14, pp. 2233–2255, 2016.
- [21]D. G. de Oteyza, E. Barrena, J. O. Ossó, S. Sellner, and H. Dosch, ‘Thickness-dependent structural transitions in fluorinated copper-phthalocyanine (F16CuPc) films’, *J. Am. Chem. Soc.*, vol. 128, no. 47, pp. 15052–15053, 2006.
- [22]D. Gentili, M. Gazzano, M. Melucci, D. Jones, and M. Cavallini, ‘Polymorphism as an additional functionality of materials for technological applications at surfaces and interfaces’, *Chem Soc Rev*, vol. 48, no. 9, pp. 2502–2517, 2019, doi: 10.1039/C8CS00283E.
- [23]T. Salzillo and A. Brillante, ‘A New Approach to Polymorphism in Molecular Crystals: Substrate-Mediated Structures Revealed by Lattice Phonon Dynamics’, *Adv. Mater. Interfaces*, vol. 9, no. 28, p. 2200815, 2022, doi: <https://doi.org/10.1002/admi.202200815>.
- [24]T. R. Fielitz and R. J. Holmes, ‘Crystal Morphology and Growth in Annealed Rubrene Thin Films’, *Cryst. Growth Des.*, vol. 16, no. 8, pp. 4720–4726, Aug. 2016, doi: 10.1021/acs.cgd.6b00783.
- [25]S. C. B. Mannsfeld, A. Virkar, C. Reese, M. F. Toney, and Z. Bao, ‘Precise Structure of Pentacene Monolayers on Amorphous Silicon Oxide and Relation to Charge Transport’, *Adv. Mater.*, vol. 21, no. 22, pp. 2294–2298, Jun. 2009, doi: 10.1002/adma.200803328.
- [26]R. Ruiz *et al.*, ‘Structure of pentacene thin films’, *Appl. Phys. Lett.*, vol. 85, no. 21, pp. 4926–4928, 2004.
- [27]V. Shalabaeva *et al.*, ‘Unprecedented size effect on the phase stability of molecular thin films displaying a spin transition’, *J. Phys. Chem. C*, vol. 121, no. 45, pp. 25617–25621, 2017.

- [28] C. Yang, S. Li, and J. Armellin, ‘Size and temperature dependence of phase stability in nanocrystalline pentacene thin films’, *J. Phys. Chem. C*, vol. 111, no. 47, pp. 17512–17515, 2007.
- [29] A. Brillante, I. Bilotti, R. G. DELLA VALLE, E. Venuti, M. Masino, and A. Girlando, ‘Characterization of phase purity in organic semiconductors by lattice-phonon confocal Raman mapping: Application to pentacene’, *Adv. Mater.*, vol. 17, pp. 2549–2553, 2005.
- [30] S. Yan *et al.*, ‘Polar Polymorphism: A New Intermediate Structure toward the Thin-Film Phase in Asymmetric Benzothieno[3,2-b][1]-benzothiophene Derivatives’, *Chem. Mater.*, vol. 36, no. 1, pp. 585–595, Jan. 2024, doi: 10.1021/acs.chemmater.3c02926.
- [31] S. Hofer *et al.*, ‘Phase transition toward a thermodynamically less stable phase: cross-nucleation due to thin film growth of a benzothieno-benzothiophene derivative’, *J. Phys. Chem. C*, vol. 125, no. 51, pp. 28039–28047, 2021.
- [32] J. Cho and T. Mori, ‘Low-temperature band transport and impact of contact resistance in organic field-effect transistors based on single-crystal films of Ph-BTBT-C10’, *Phys. Rev. Appl.*, vol. 5, no. 6, p. 064017, 2016.
- [33] H. Iino, T. Usui, and J. Hanna, ‘Liquid crystals for organic thin-film transistors’, *Nat. Commun.*, vol. 6, no. 1, p. 6828, 2015.
- [34] T. Hamai, S. Arai, H. Minemawari, S. Inoue, R. Kumai, and T. Hasegawa, ‘Tunneling and origin of large access resistance in layered-crystal organic transistors’, *Phys. Rev. Appl.*, vol. 8, no. 5, p. 054011, 2017.
- [35] M. Yoneya, ‘Monolayer Crystal Structure of the Organic Semiconductor 7-Decyl-2-phenyl[1]benzothieno[3,2-b][1]benzothiophene’, *J. Phys. Chem. C*, vol. 122, no. 39, pp. 22225–22231, Oct. 2018, doi: 10.1021/acs.jpcc.8b04386.
- [36] G. Ashiotis *et al.*, ‘The fast azimuthal integration Python library: it pyFAI’, *J. Appl. Crystallogr.*, vol. 48, no. 2, pp. 510–519, Apr. 2015, doi: 10.1107/S1600576715004306.

- [37]S. Hofer *et al.*, ‘Molecular Disorder in Crystalline Thin Films of an Asymmetric BTBT Derivative’, *Chem. Mater.*, vol. 33, no. 4, pp. 1455–1461, Feb. 2021, doi: 10.1021/acs.chemmater.0c04725.

Supporting information

Thickness dependent structural transition in Ph-BTBT-10 thin films and stabilization of the ubiquitous interface bilayer

Shunya Yan^a, Alba Cazorla^a, Eduardo Solano^b, Carmen Ocal^{a}, Esther Barrena^{a*}*

^a Institut de Ciència de Materials de Barcelona (ICMAB-CSIC), 08193 Bellaterra, Barcelona, Spain

^b ALBA synchrotron, C/de la Llum 2-26, Cerdanyola del Valles, Barcelona, 08290, Spain

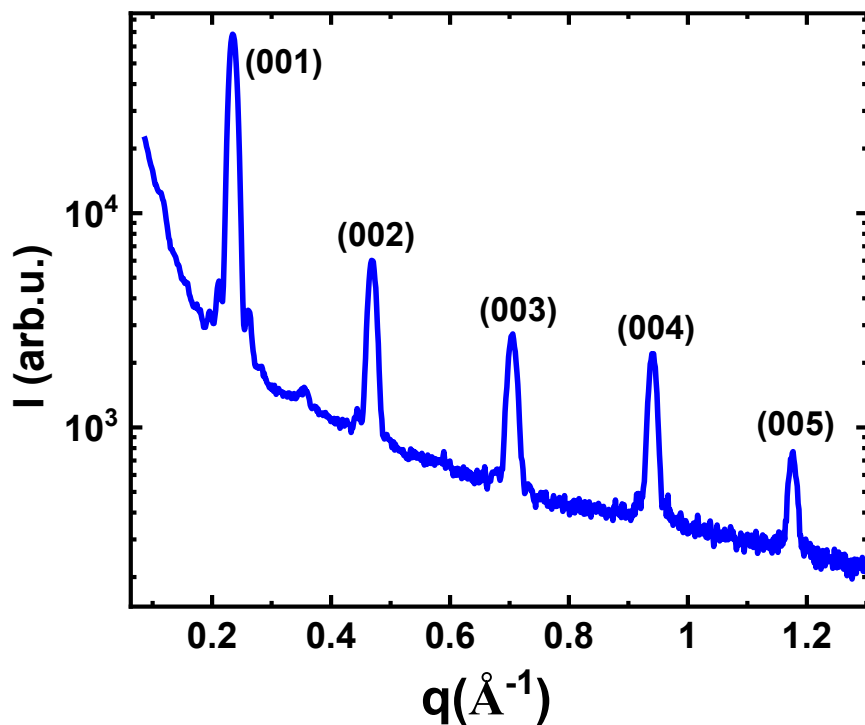


Figure S1. XRD specular data obtained from the as prepared 40 nm-thick film of Ph-BTBT-10.

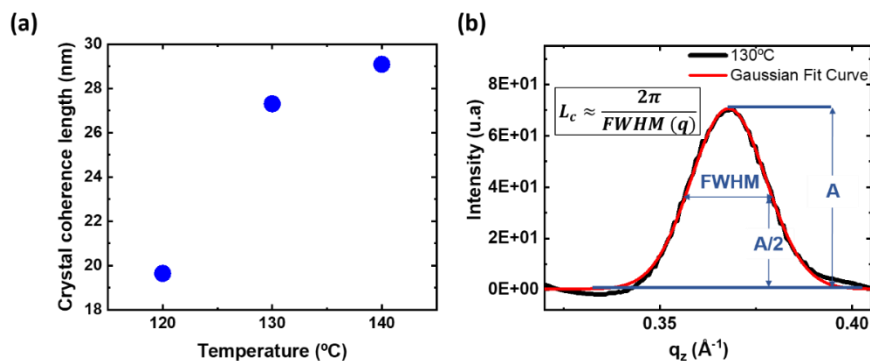


Figure S2: (a) Crystal coherence length calculated from the FWHM of the $(003)_{BL}$ peak at the indicated temperatures. (b) Estimation of the crystal coherence length (L_c) from the FWHM of a diffracted peak.

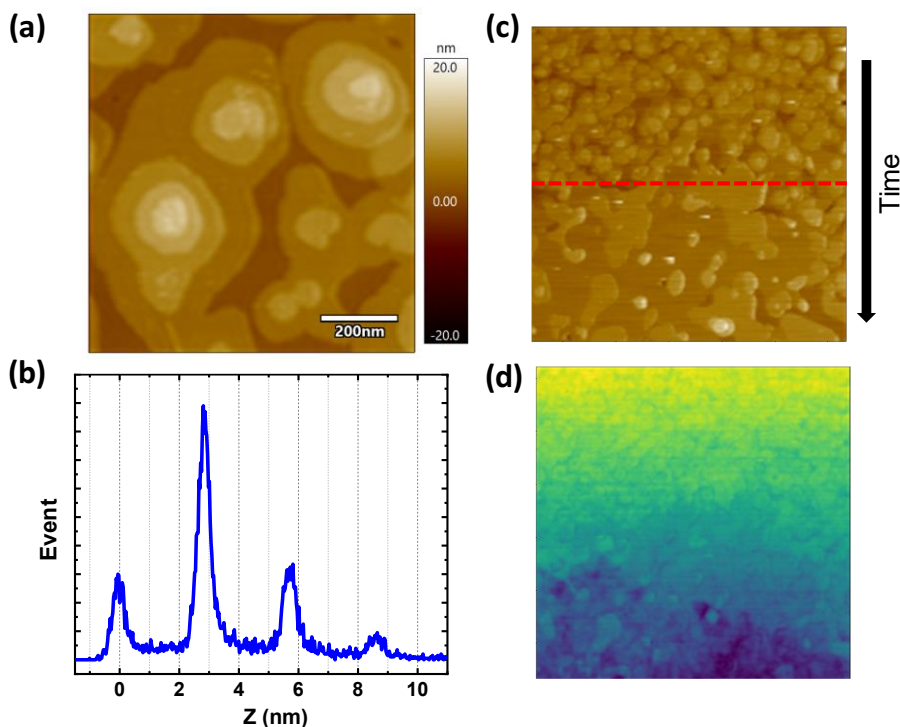


Figure S3. (a) Magnified image of the as prepared 40 nm-thick film grown at room temperature. (b) Histogram of surface heights in (a). The difference between the adjacent peaks corresponds well to the single layer thickness (step height). (c) and (d) Zoomed area of the Figure 4, measured during scanning at 110°C. The total color scales are 40 nm (topography) and from -150 to 550 mV for dark to light SP contrast.

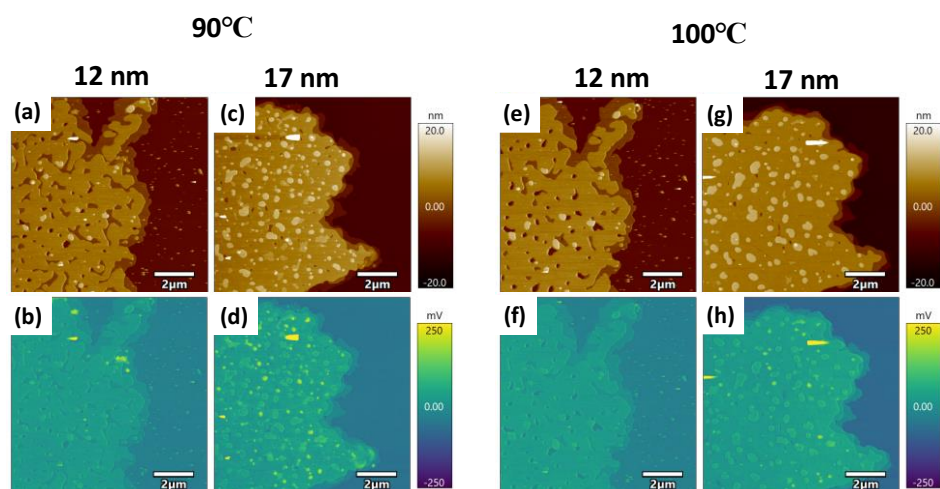
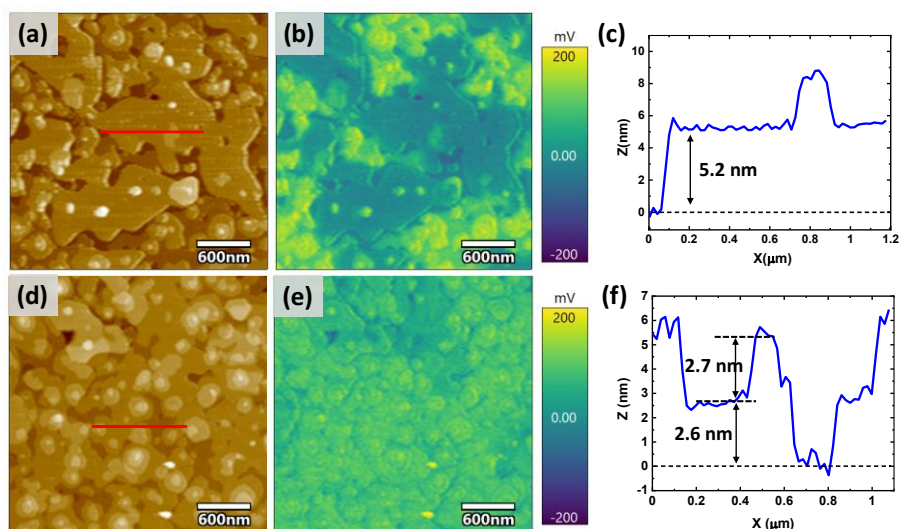


Figure S4. Topography (a and c) and surface potential maps (b and d) of 12 nm- and 17 nm-thick thin films, taken at RT after post-growth annealing at 90°C. Additionally, the topography (e and g) and surface potential maps (f and h) also taken at RT but after annealing at 100°C. Note that the 17 nm-thick film evolves from annealing to one and the other temperatures, whereas the 12 nm-thick film shows negligible differences between them.



Figure

S5. Topography (a and d) and surface potential maps (b and e) of 12 nm- and 17 nm-thick thin films, taken at RT after post-growth annealing during 5 minutes at 60°C. Line profiles in (c) and (f) correspond to the topography along the segments in (a) and (d), respectively.

From the surface potential map, it can be observed that for the 12 nm-thick film, some regions have transitioned from SL packing to BL packing after 5 minutes of post-growth annealing, resulting in a different surface potential. Comparison with the topography, indicates that the lower surface potential corresponds to a step height of 5.2 nm, which equals the thickness of the bilayer (BL structure). However, in the surface potential image of the 17 nm-thick film, there is no strong contrast, and the surface potential is predominantly arising from piled single layers. Indeed, the height profile shows that the steps are around 2.6 nm high, as expected from a SL structure. This supports that the thinner films require less temperature compared with thicker film for the onset of the structural transition.

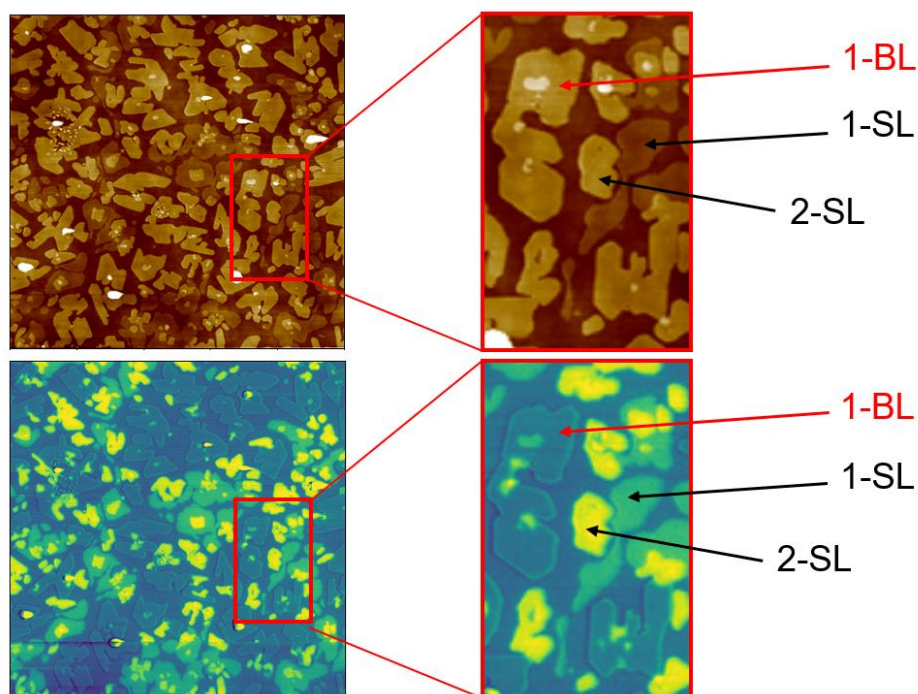


Figure S6. Left: Topography and surface potential maps (time = 0h in Figure 7 of the manuscript). Right: Magnified images of the regions indicated. 1-SL and 2-SL stand for islands consisting of one or two single molecular layers, respectively, while 1-BL stands for bilayer islands.

Figure S6 illustrates the use of SP data to differentiate islands of the asymmetric Ph-BTBT-10 with similar height (same color in topography), but made out of one bilayer (1-BL) or two single layers (2-SL). Islands as the labelled 1-BL exhibit a surface potential similar to that of the surrounding bare substrate, but 2-SL islands have a more positive SP. The SP of 2-SL is twice of that of just 1-SL, reflecting the additive character of polar layers with same orientation. 2-SL consists of molecules with the same orientation within one layer and in the

adjacent one. Conversely, 1-BL islands are made out of the typical non-polar bilayer assembly reported at the substrate interface, where molecules at each layer have the same orientation but opposite to the adjacent layer. In this context, one half of BL can be seen as 1-SL. Notably, when some molecules are nucleated on top of the BL, the aggregates can be 1-SL and 2-SL (see aggregates on the indicated 1-BL island).

Part III

CONCLUSION

7

SUMMARY AND PERSPECTIVES

In this study, we utilized nanoscale surface characterization techniques such as Kelvin Probe Force Microscopy (KPFM), X-ray Diffraction (XRD), and Ultraviolet Photoelectron Spectroscopy (UPS) to investigate the polymorphism of organic semiconductor materials. From our findings, we provide recommendations for optimizing and controlling thin film quality for improving the performance and reproducibility of OFET devices.

In the first part of this work, we used Grazing Incidence Wide-Angle X-ray Scattering (GIWAXS) and Atomic Force Microscopy (AFM) to study the impact of substrate temperature on the morphology and structure of C8O-BTBT-OC8 films grown via physical vapor deposition. After annealing at 90 °C or beyond we observed a structural transition from the substrate-induced phase (SIP) at room temperature to a new polymorph called high-temperature phase (HTP). In the HTP, molecules are tilted from the normal direction with an average angle of approximately 39°, leading to a reduced inter-planar spacing and slightly expanded in-plane unit cell. AFM results indicated that this structural transition is reversible for annealing temperatures below 150 °C. Upon cooling to room temperature, the HTP reverts to SIP. However, molecular layers at the SiO₂ interface may retain the HTP structure, overlaid by the SIP structure, potentially resulting in SIP and HTP coexistence at the interface, influenced by annealing temperature and cooling rate. This could negatively impact OFET field-effect mobility. Annealing temperatures above 150 °C leads to film dewetting and more complex morphology due to coexisting molecular angles during cooling.

In the second study, we investigated the polymorphism of another BTBT derivative, Ph-BTBT-10. Understanding its structure and polymorphism is crucial for optimizing

Chapter7 SUMMARY AND PERSPECTIVES

OFETs using Ph-BTBT-10 as the conducting channel, given that high carrier mobility in Ph-BTBT-10 films is linked to the bilayer structure. Systematic nanoscale morphology analysis and KPFM revealed that Ph-BTBT-10 films exhibit a complex structure beyond the reported single-layer to bilayer transition model. For films thinner than 20 nm, a polar thin film structure, intermediate between bilayer and thin film phases, was identified directly at the substrate surface. Density Functional Theory (DFT) calculations quantified a vacuum level shift by -0.273 eV for one layer with all molecular dipoles in an alkyl-up configuration, consistent with the measured surface potential shift in one molecular layer. With increasing thickness, the vacuum energy level decreases in a non-linear manner, attributed to an increased percentage of molecules with an alkyl-down orientation, leading to the non-polar antiparallel configuration of the thin film phase observed at higher thicknesses. This study underscores that KPFM is a valuable tool to evaluate electrostatic disorder and the emergence of polar polymorphs in thin films. The reported film structure has dramatic consequences in the electronic properties, in particular, we demonstrated a decrease in the work function with increasing thickness up to ~ 1 eV and a broadening of the HOMO attributed to electrostatic disorder.

Building on the second study, we further examined the role of interfaces in the structural transitions of Ph-BTBT-10 films and the impact of thickness on film stability. Using KPFM and GIWAXS, we monitored structural changes in Ph-BTBT-10 films of varying thicknesses during thermal annealing. We concluded that reduced thickness enhances bulk phase stability, as evidenced by a lower critical temperature for the transition to the bilayer structure. Studies on ultra-thin films revealed diffusion and reorganization processes over several hours, leading to an evolution from a stacking of polar single-layers towards the bilayer structure. Our results demonstrated that reducing film thickness lowers the temperature required for transition to the thermodynamically stable bilayer phase, contrary to reports on other organic semiconductor films.

Outlook:

Chapter7 SUMMARY AND PERSPECTIVES

In our investigation of C8O-BTBT-OC8, we found and proposed that growing films at appropriate substrate temperatures is more suitable for enhancing the electrical performance of thin films than post-annealing. After post-annealing and cooling, there is a possibility of SIP and HIP structures coexisting at the interface, which can negatively impact the carrier mobility of OFETs. Therefore, further research on the effects of different annealing and cooling process parameters on the organic film/SiO₂ interface structure is crucial.

In our study of Ph-BTBT-10, we first identified for thin-films a polar arrangement of the molecules that indicate the importance of dipolar electrostatic interactions. We suggest that polar assembly may be a common issue for other asymmetric BTBT derivatives, necessitating consideration for understanding structure-performance relationships in OFETs. Accurately determining polar assemblies near interfaces is crucial for the strategic design and development of high-performance OFETs.

AUTHOR'S CONTRIBUTIONS

1. **Yan, S.**; Cornil, D.; Cornil, J.; Beljonne, D.; Palacios-Rivera, R.; Ocal, C.; Barrena, E. Polar Polymorphism: A New Intermediate Structure toward the Thin-Film Phase in Asymmetric Benzothieno[3,2-b][1]-Benzothiophene Derivatives. *Chem. Mater.* **2024**, *36* (1), 585–595.
2. **Yan, S.**; Cazorla, A.; Babuji, A.; Solano, E.; Ruzié, C.; Geerts, Y. H.; Ocal, C.; Barrena, E. Temperature-Induced Polymorphism of a Benzothiophene Derivative: Reversibility and Impact on the Thin Film Morphology. *Phys Chem Chem Phys.* **2022**, *24* (39), 24562–24569.
3. Gutiérrez-Gálvez, L.; García-Mendiola, T.; Lorenzo, E.; Nuez-Martinez, M.; Ocal, C.; **Yan, S.**; Teixidor, F.; Pinheiro, T.; Marques, F.; Viñas, C. Compelling DNA Intercalation through ‘Anion–Anion’ Anti-Coulombic Interactions: Boron Cluster Self-Vehicles as Promising Anticancer Agents. *J Mater Chem B.* **2024**, Advance Article.
4. Jiménez-Guerra, M.; Calvo-Barrio, L.; Asensi, J. M.; Caño-Prades, I.; **Yan, S.**; Barrena, E.; Puigdollers, J.; Jehl, Z.; Sánchez, Y.; Saucedo, E. KCN Chemical Etching of van Der Waals Sb₂Se₃ Thin Films Synthesized at Low Temperature Leads to Inverted Surface Polarity and Improved Solar Cell Efficiency. *ACS Appl. Energy Mater.* **2024**, *7* (3), 874–884.
5. Caño, I.; Navarro-Güell, A.; Maggi, E.; Barrio, M.; Tamarit, J.-L.; Svatek, S.; Antolín, E.; **Yan, S.**; Barrena, E.; Galiana, B.; Placidi, M.; Puigdollers, J.; Saucedo, E. SbSeI and SbSeBr Micro-Columnar Solar Cells by a Novel High Pressure-Based Synthesis Process. *J Mater Chem A* **2023**, *11* (33), 17616–17627.
6. **Yan, S.**; Cazorla, A.; Solano, E.; Ocal, C.; Barrena, E. Thickness dependent structural transition in Ph-BTBT-10 thin films and stabilization of the ubiquitous interface bilayer. **2024**, (Submitted)

ACKNOWLEDGEMENT

At the end of the thesis, I would like to say thanks to all the people who support, help and inspired me in the last four years.

First and foremost, I want to express my heartfelt gratitude to my supervisor, **Esther Barrena**. I'm deeply thankful for the opportunity she gave me to join this research group. Esther is knowledgeable, kind, positive, generous, patient, and independent. Over the past four years, she has provided me with invaluable guidance in my academic pursuits and generous support in my personal life and career decisions. She has been not just an academic mentor, but a life mentor as well. I feel incredibly fortunate to have worked with her, and her rigorous work ethic and passion for life have truly inspired me.

I also want to thank **Carmen Orcal**. She is always elegant and meticulous. As our group leader, she has consistently supported me whenever I needed it and has offered valuable guidance by pointing out details I might have overlooked. Her dedication and seriousness in her work have profoundly influenced me.

I extend my gratitude to the other members of the research group. First, **Francesco Silvestri**, who was incredibly patient when I first joined, helping me get familiar with the environment and teaching me how to use various experimental instruments. I am deeply grateful for his help. Next, **Adara Babuji**—thank you for the life tips and assistance when I first arrived, which helped me integrate more smoothly into life in Barcelona. Then there's **Ana Pérez-Rodríguez**, who, although she had already graduated when I joined, became a close friend during later collaborations. I'm very thankful for the guidance she provided me as a senior in the lab.

Also to **Rogger**, who is enthusiastic, positive, and professional. Whether it was sharing his desk when I first joined or offering advice when I was job hunting later on, I'm truly grateful for all his support. Special thanks to **Alba Cazorla**, who has been both a

colleague and a friend. I appreciate her companionship and encouragement when I was feeling down. Lastly, I want to thank the new members, **Georgios Atsas, Rodrigo,** and **Daniel** Martín-Jiménez. I'm very happy to have met you all, and I wish you all the best.

I also want to thank the friends I met at ICMA B: **Tommaso Albrigi, Khanam Naureen, Masoudinia Fereshteh, Ali Faizan, Jo Sunghwan,** and others. The memories of us playing, chatting, and sharing our countries' traditions, customs, and cuisines are still vivid in my mind. I believe our friendship will last a lifetime.

Additionally, I want to thank my landlord, **Clara.** (Voy a escribir este párrafo en español, porque es para ella). Es una mujer admirable con mucho gusto. Estoy muy agradecida por el ambiente cálido y hogareño que me ha brindado, y por compartir de vez en cuando diversas delicias españolas, lo que me hizo sentir como en casa, incluso estando lejos. Un agradecimiento especial a nuestra pequeña querida, **Ethan,** quien siempre está tan feliz, llena de energía y esperanza. Ella me ha enseñado a enfrentar la vida con sencillez y positividad, y es un rayo de luz en mi vida.

Finally, I want to thank **my parents and friends** for their unwavering support. Thank you for always being there for me, encouraging me during tough times, and celebrating my successes. I will always cherish your companionship and support. I feel incredibly lucky to have you in my life, and I will do my best not to let you down. I look forward to continuing to support each other in the journey ahead.